ADVANCED METHODS IN MOLECULAR BREAST IMAGING

ADVANCED METHODS IN MOLECULAR BREAST IMAGING

By ASHLEY T. TAO, B.Sc., M.Sc.

A Thesis Submitted to the School of Graduate Studies in Partial Fulfillment of the Requirements for the Degree Doctor of Philosophy

DOCTOR OF PHILOSOPHY (2016) McMaster University
(Medical Physics) Hamilton, Ontario

TITLE: Advanced Methods in Molecular Breast Imaging

AUTHOR: Ashley T. Tao, B.Sc., M.Sc. (McMaster University)

SUPERVISOR: Dr. Troy H. Farncombe

NUMBER OF PAGES: ix, 175

Abstract

Molecular breast imaging (MBI) is a relatively new clinical breast imaging modality, which has the potential to have a significant impact in breast cancer screening and perioperative breast imaging for women with high risk factors for developing breast cancer. Two objectives were proposed in this thesis to increase the use of MBI. First, a magnetic resonance (MR)-compatible gamma camera was developed for combined molecular/MR breast imaging. MBI is a functional imaging technique with high specificity and sensitivity but could benefit from the addition of anatomical information from breast MRI for lesion localization, cancer staging, treatment planning and monitoring. A small area (8 cm×8 cm) cadmium zinc telluride (CZT) based gamma camera was developed and tested for MR compatibility in both sequential and simultaneous imaging conditions. Results indicated that the gamma camera was minimally affected during both sequential and simultaneous imaging with a gradient echo (GRE) and spoiled gradient echo (GRE) sequence. Signal to noise ratio (SNR) degradation was observed in the MR images but no geometric distortions were observed. Simultaneous imaging is feasible, but a reassessment of the RF shielding would be required to minimize the noise contribution degrading image quality. Second, backscatter photons were investigated as a potential dose reduction technique for MBI. While the effective dose from MBI is relatively low in comparison to other nuclear medicine procedures, the dose is considered high in relation to mammography and in order to increase acceptance as an alternative breast imaging method, dose reduction is an important objective. Backscatter photons have the same spatial information as primary photons but are typically discarded along with other scattered photons. A scatter compensation method called the triple energy window (TEW) was used to extract backscatter photons from the Compton scattering spectrum and added to the primary photons, increasing count sensitivity by 6 %. The noise level matched the increase in contrast leading to negligible change in lesion contrast to noise ratio (CNR). Dose reduction is not justified with this particular technique because of the elevated noise level, but the use of backcsatter photons show potential with improved contrast.

This thesis is dedicated to my late mother, Helen Tao.

Acknowledgements

There are many people that I must acknowledge, for without everyone's support, the culmination of my PhD would not have been possible. My first acknowledgement must goes to my supervisor Dr. Troy Farncombe. Words cannot begin to describe how thankful and grateful I am for his constant support and guidance throughout my years as a graduate student at McMaster. I truly appreciate the time he took to guide me on this journey. He was always available to meet with me whenever I needed to discuss something. He taught me how to think more critically and how to problem solve more efficiently (even though it may not always seem like it). I am indebted to him for everything that he has done for me over the years. I could not have asked for a better supervisor.

I must also thank Dr. Michael Noseworthy for his contribution to my work and for being a part of my committee. He was the driving force that made it possible to test my gamma camera inside the MRI scanner. His invaluable knowledge of MRI played a critical role in my research.

Thank you to Dr. Soo-Hyun Byun who has always supported me throughout all my years at McMaster and for stepping in to be a part of my committee on short notice.

I would like to acknowledge Norm Konyer for all the times that he has helped me with tests in the MRI scanner and for all the times he was available to discuss with me any MRI related issues I had.

I would like to extend my thanks and gratitude to those in the Imaging Research Centre and the department of Nuclear Medicine at both McMaster University Medical Centre (MUMC) and St. Joseph's Healthcare Hamilton who have contributed both directly and indirectly to my research. A special thank you to Mark Weir, Janet Crouch, Cathy McCaw and Kristina Taylor for facilitating the logistics of running my experiments with radioisotopes in the MRI scanner and Steve Madison for his assistance with acquiring CT images.

The construction of my gamma camera system would not have been possible without the help of George Boyes and Steve Fick in the machine shop at MUMC, Amy Tao and Michael Gooch at Multimatic Technical Centre and my supervisor, Dr. Farncombe.

I would like to thank my fellow graduate students in both medical physics and biomedical engineering (past and present) for encouraging me during challenging times. They were a wonderful group of people who were there to discuss my many obstacles or to just have a coffee break with. A special thank you to Alireza Akbari for the countless hours he put into helping me out with running tests in the MRI scanner and Hedi Mohseni for moral support and taking the time to proofread my thesis. Thank you to my lab colleagues, Muhammad Irfan Karamat and Alvin Ihsani for helping me set up SHARCNET on short notice and for moral support.

Lastly, thank you to my family and friends who have always been supportive in my pursuit for a PhD. A special thank you to my aunt, Ann Linton who has had a significant impact on the person that I am today. Thank you to my parents for sacrificing everything in their lives and to all the families that sponsored my parents to come to Canada, so that I would have the opportunity to pursue my dreams and live the life that I have.

To everyone who has helped me and supported me in this journey, thank you.

Contents

List of Figures

List of Tables

List of Abbreviations

ADC	Analog to digital converter
ASIC	Application specific integrated circuit
B_0 field	Main magnetic field
B_1 field	Rotating RF magnetic field
BSGI	Breast specific gamma imaging
CC	Craniocaudal
CNR	Contrast to noise ratio
CS	Chip select
CT	Computed tomography
CZT	Cadmium zinc telluride
DCE	Dynamic contrast enhanced
DRB	Digital readout board
DU/IU	Differential/Integral uniformity
EDR	Event data readout
FFC	Flat flexible cable
FIFO	First in first out
FOV/CFOV/UFOV	Field of view(Central/Useful)

FPGA	Field programmable gate array
FWHM	Full-width at half maximum
FWTM	Full-width at tenth maximum
GATE	Geant4 Application for Tomographic Emission
GPIO	General purpose input/output
GRE/SPGR	Gradient echo (Spoiled)
GUI	Graphical user interface
LAR	Lifetime attributable risk
LSB	Least significant bit
LVDS	Low voltage differential signaling
MBI	Molecular breast imaging
MFH	Magnetic field homogeneity
MIBI	sestamibi/6 methoxyisobuylnitrile ligands
MISO	Master in slave out
MLO	Mediolateral oblique
MOSI	Master out slave in
MRA	Module register access
MRI	Magnetic resonance imaging
MSB	Most significant bit
mux/demux	Multiplexer/demultiplexer
PET/PEM	Positron emission tomography/mammography
PMT	Photomultiplier tube

RF	Radio frequency
ROI	Region of interest
SCLK	SPI clock
SE	spin echo
SNR	Signal to noise ratio
SPECT	Single photon emission computed tomography
SPI	Serial peripheral interface
TE	Echo time
TEW	Triple energy window
TR	Repetition time
USB	Universal Serial Bus

Declaration of Academic Achievement

The work presented in this thesis is the result of research performed by myself during the years 2012-2016 and has not previously in its entirety or part submitted to any academic institution for any degree. Contributions from other authors are appropriately acknowledged.

Chapter 1

Introduction

1.1 Motivation

Advancements in breast imaging for early detection and improved treatments of breast cancer have led to a 6 % increase in the 5-year relative survival rate for Canadian women diagnosed with breast cancer in 2006-2008 versus 1992 [1]. Despite these improvements, breast cancer remains the most common cancer diagnosis in Canadian women and is second to lung cancer death rates. As of 2015, it is estimated that 1 in 9 Canadian women will develop breast cancer during her lifetime and 1 in 30 will die from it [1].

Mammography is currently the gold standard for breast cancer screening, because it is the only imaging modality proven to reduce mortality from breast cancer [2] and the diagnostic value of mammography far exceeds the risk of radiation induced cancer. The sensitivity of mammography is relatively high (71-96 %) for the screening population [2, 3], but studies have shown that it significantly decreases (30-69 %) for women with dense breast tissue [4, 5]. Sensitivity decreases in this subpopulation because the underlying principle relies on imaging the differences in tissue density. Tumours and microcalcifications (a potential breast cancer marker) are visible on mammograms because they are more dense than normal breast tissue which is generally comprised of fat. However, dense breast tissue combined with potentially cancerous lesions inherently creates poor physical contrast leading to lower sensitivity. Confounding this limitation in mammography, breast density is also a known risk factor for developing breast cancer [6–9]. Studies have shown that sensitivity also decreases due to variability in breast density and other risk factors associated with breast cancer such as BRCA gene mutations in women with both dense and fatty breast tissue [10–14]. BRCA gene mutations can occur in the BRCA1 or BRCA2 gene, which are tumor suppressor genes responsible for repairing damaged DNA. Mutations in these genes do not necessarily imply the development of breast cancer, but studies have indicated elevated incidences of breast cancer [15–17].

There are a number of alternative breast imaging methods such as magnetic resonance imaging (MRI), ultrasound and thermography, but breast MRI is the preferred modality second to mammography for screening patients with high risk factors for developing breast cancer, as well as perioperative breast imaging. MRI has been touted for its very high sensitivity due to its superior soft tissue contrast and ability to resolve fine tissue structure, but it tends to also highlight inconsequential morphological abnormalities resulting in specificity ranging from 37-97 % [18, 19].

A relatively new imaging modality that is starting to gain more acceptance is molecular breast imaging (MBI). MBI is a functional imaging technique which images the preferential uptake of a radioactive tracer (Tc-99m sestamibi) in breast cancer rather than the anatomical structure of the breast tissue. MBI uses a specialized gamma camera made with solid state detectors called cadmium zinc telluride (CZT) for dedicated breast imaging. Recent studies have reported sensitivity as high as 90 % and specificity between 82 % and 90 % [20, 21]. While MBI boasts higher specificity and sensitivity in comparison to mammography, it only provides information based on the functional aspect of the Tc-99m uptake. Despite the advancements in MBI, it is not yet widely accepted as an option for breast imaging. According to the most recent breast imaging and intervention guideline from the Canadian Association of Radiologists, MBI is not listed as one of the modalities recommended for breast imaging [22]. One of the major contributing factors preventing MBI from having a stronger presence in breast imaging is the higher effective dose to patients. In addition, MBI is still a relatively new modality and so accessibility to this dedicated breast imaging system is limited. MBI has the potential to make a significant impact on the diagnosis and treatment of breast cancer in women with risk factors for developing breast cancer.

1.2 Objective

This thesis focuses on two proposed methods to increase the use of MBI to help improve breast cancer diagnoses and aid in breast cancer treatment planning. The first objective was to develop a gamma camera insert for simultaneous MBI and breast MR imaging to combine the advantages of both imaging modalities, and the second objective was to investigate a software based scatter correction method called the triple energy window (TEW) to reduce dose to the patient and/or improve image quality by making use of backscattered photons.

1.2.1 Combined MBI/MRI Imaging

MBI lacks anatomical detail, but provides functional information based on the uptake of Tc-99m sestamibi, while breast MRI provides anatomical detail with excellent soft tissue contrast. Combining the two imaging modalities would complement one another and provide additional information to support the drawbacks of each. This concept

of combining two imaging systems dates back to the early 1990's when Hasegawa et al. proposed combining single photon emission computed tomography (SPECT) with computed tomography (CT) [23] and shortly thereafter, Townsend et al. developed the first prototype positron emission tomography (PET)/CT system [24]. Dual modality imaging has become a popular area of research because it is acknowledged by the medical imaging community that there is no one modality that has the sensitivity and specificity for optimal imaging. PET/CT for example, has had such a significant impact that stand-alone PET is now practically obsolete. Recently, the first commercial PET/MR system was released. However, whole body dual-modality imaging with MRI is financially cumbersome to health care systems. The motivation for combined MBI/MRI is two-fold. The first reason is to provide a low cost gamma camera for dual-modality imaging with MRI for dedicated breast imaging with minimal modifications to the existing MR hardware. The second reason is the combination of high sensitivity from MRI and specificity from MBI may improve the ability to localize lesion boundaries and extent of pathology. In addition to high risk screening, this could also be used to monitor disease progression/regression and aid in surgical planning. This dual-modality system would allow physicians to view breast tissue from both an anatomical and functional perspective, allowing better interpretation of breast images following surgery. The scan time for a simultaneous MBI/breast MRI system would be significantly reduced compared to sequential imaging, and potential patient movement/image registration errors would be minimized by maintaining patient positioning.

Developing an MBI system to function simultaneously with MRI presents several major challenges. First, the gamma camera components must be non-ferromagnetic and must be insensitive to the large static and changing magnetic fields. On the other hand, MRI is sensitive to minute changes in the magnetic field and extraneous radio frequency (RF) could degrade MRI performance. The main focus was to develop a gamma camera system to function inside the MRI as a prototype to test with breast MR imaging without altering the existing MRI system. Traditional gamma cameras are incompatible in large magnetic fields, but recent developments in semiconductor detectors have made it feasible to perform gamma imaging in the presence of large magnetic fields. Current MBI systems use CZT (a semiconductor detector) for it's detection efficiency, and spatial and energy resolution, but the gamma camera itself was not designed for MRI compatibility. The proposed gamma camera system was designed

around CZT detectors and would image the uptake of Tc-99m, while simultaneously performing breast MR imaging. The two sets of images would then be co-registered for image interpretation.

1.2.2 TEW Method for Dose Reduction

MBI has not received acceptance similar to that of mammography or breast MRI mostly due to the exposure from ionizing radiation. Currently, MBI results in a much higher effective dose (6.5 mSv) compared to screening mammography (0.4-0.6 mSv) [25, 26]. While the effective dose is much lower than other nuclear imaging techniques, it is considered too high for screening. A study from 2010 determined the lifetime attributable risk (LAR) of fatal cancer from an administered dose of 740 MBq (20 mCi) of Tc-99m was 20 times higher than mammography, in women aged 40 years at exposure. Using the 'as low as reasonably achievable (ALARA)' principle as a guiding motivation, lowering the administered dose would minimize the LAR of fatal cancer and provide an alternative option in breast cancer screening programs.

The proposed method to investigate dose reduction is through the addition of backscatter photons to photopeak photons. Backscatter photons are photons which undergo a 180° scatter and deposit their energy with the same spatial information as primary photons but with lower energy. These photons are typically discarded along with the remaining scatter spectrum. The goal is to make use of these photons using a software based scatter correction method called the triple energy window (TEW) to increase count sensitivity by separating the backscatter photons from the rest of the scattered spectrum. The TEW method was originally developed for dual-isotope imaging to remove down-scattered photons in the lower energy isotope from radioisotopes with higher gamma emissions. Since the probability of backscatter is higher at lower energies relative to higher energies, it is postulated that the low energy emitting radioisotope used in MBI would yield an appreciable number of backscatter photons. If the TEW scatter correction can extract the backscatter photons from the scatter spectrum, the increase in count sensitivity could potentially lead to decreased dose in MBI studies or improved image quality.

1.3 Thesis Outline

This thesis contains five main chapters aside from the introduction; Chapter 2 outlines the various breast imaging modalities and the current research in molecular breast imaging along with a literature review for each proposed objective. Chapter 3 describes the design and development of the CZT based gamma camera. Chapter 4 evaluates both imaging modalities using the gamma camera developed in the previous chapter. The experiments used to characterize the effects of MRI on MBI and vice versa during sequential and simultaneous imaging conditions, are presented along with the results. A discussion of the results and challenges from combined planar gamma imaging and breast MRI are reviewed. Chapter 5 presents the methods and results from investigating backscatter photons for use in MBI followed by a discussion and recommendations for dose reduction. Finally, this thesis will culminate with a summary of the results and suggestions for future work.

Chapter 2

Overview of Breast Imaging Modalities and Literature Review

The Canadian Association of Radiologists published a guideline on the recommended imaging modalities and protocols for both screening and perioperative breast imaging [22]. Mammography is considered the gold standard, but secondary and tertiary imaging options such as breast MRI and ultrasound are used for women with high risk factors for developing breast cancer and to address inconclusive mammograms. Currently, MBI is not included in this guideline, but it offers significant advantages which will be discussed below. The following is a brief review of MBI, each of the modalities currently recommended for breast imaging, alternative imaging modalities, and a summary of the current status of molecular breast imaging.

For the combined MBI/MRI background, there will be a review consisting of the foundations of gamma camera design, the challenges associated with dual-modality imaging with MRI and a literature review summarizing recent research in simultaneous nuclear/MRI imaging.

Additionally, the background will include the physics of backscattering and the fundamental concept in the TEW scatter correction method used to investigate the potential count sensitivity increase/dose reduction. A literature review will follow highlighting the use of the TEW method and use of backscatter photons in imaging.

2.1 Breast Imaging Modalities

2.1.1 Mammography

In mammography, the breast is compressed between two compression plates and images are acquired by measuring the penetration of low energy X-rays through breast tissue. Compression is necessary to minimize the dose to the patient, to spread out the breast tissue so that abnormalities are not obscured by overlying breast tissue, to minimize x-ray scatter, and to minimize patient movement. Two standard views, craniocaudal (CC) and mediolateral oblique (MLO) are obtained to visualize as much of the breast as possible. The average effective dose from digital and screen-film mammograms are between 0.4-0.6 mSv [25, 26].

For the general population, this method for breast cancer screening has been very successful at detecting tumours while imposing minimal radiation exposure and reducing breast cancer mortality rates [1, 27, 28]. Unfortunately, mammography is not effective in detecting breast cancer in women with dense breast tissue because X-ray attenuation in

dense breast tissue is similar to cancerous lesions thus resulting in a higher proportion of false negatives. Breast tissue composition varies among women and Fig. 2.1 summarizes the varying levels of tissue density. The American College of Radiology Breast Imaging Reporting and Data System (BI-RADS) guideline characterizes breast density as mostly fat, scattered fibroglandular tissue, heterogeneously dense tissue or mostly fibroglandular tissue. Based on data from 1996 to 2008, 40 % of women had scattered fibroglandular tissue, 40 % had heterogeneously dense breast tissue and a smaller proportion (10 %) with extremely dense tissue [29]. At least 50 % of women have a considerable amount of dense breast tissue and the likelihood of visualizing early stage breast cancer in these patients with mammography is low. Recent studies have reported sensitivities ranging from 30-80 % due to dense breast tissue [30]. Compounding the low sensitivity in mammography from dense breast tissue, the Canadian National Breast Screening Study also showed that women with dense breast tissue were at an increased risk for developing breast cancer [31].

Contrast enhanced (CE) mammography with iodine has been investigated as a means to address the low sensitivity from dense breast tissue. However, a special imaging technique is required to visualize the contrast from the small amount of iodine present. Two sets of images are acquired, one at low energy, the standard low energy X-ray ($\sim$ 28-33kV) used to image the breast and a higher energy X-ray ($\sim$ 45-49kV) to take advantage of the property of iodine for improved contrast. The low energy image is subtracted from the high energy image to visualize the uptake of iodine [32]. Some of the disadvantages of this method is a 1.5$\times$ increase in the radiation dose compared to traditional mammography and some patients experience adverse reactions to the iodine contrast [32]. While some studies have shown that sensitivity improves over traditional mammography, these studies were limited in population size [33–37]. In addition, contrast enhanced breast MRI (discussed in the next section) consistently outperformed contrast enhanced mammography in terms of sensitivity. Therefore, further studies are required to justify the increased use of CE-mammography.

An emerging method of breast imaging based on the same principles of mammography is digital breast tomosynthesis, except that several X-ray projections are acquired over a limited range of angles to reconstruct the breast in three dimensions. Depending on the manufacturer, 9-25 projection images are acquired over an arc ranging between 11°-60°. Despite the use of multiple projections as compared to two projection images from mammography, the dose to the patient is comparable for both modalities[39,

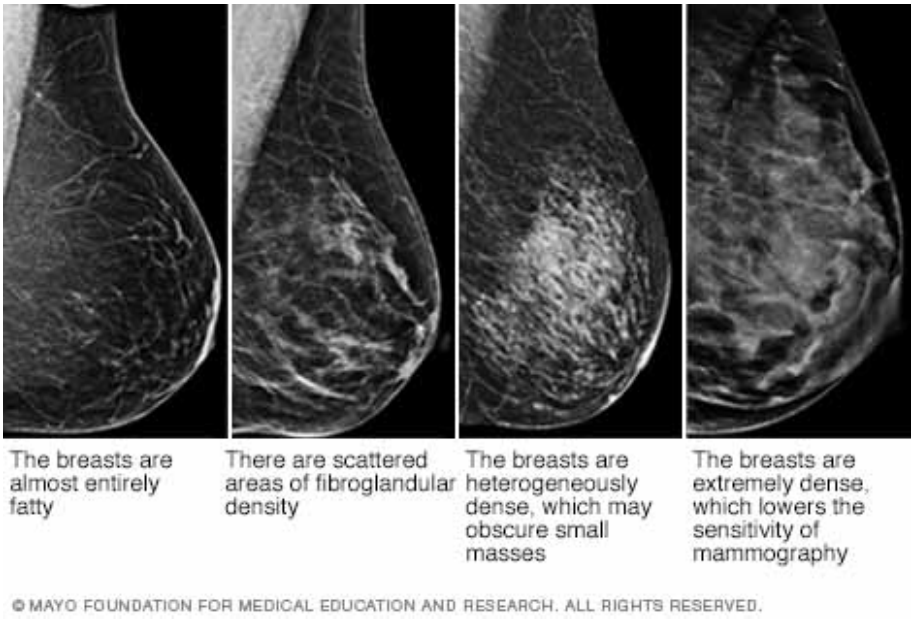

Figure 2.1: Differences in breast tissue density. Reprinted with permission of Mayo Foundation for Medical Education and Research [38].

40]. This method provides better visualization of potentially hidden lesions within the breast tissue with marginal improvement in sensitivity, but dense breast tissue remains a fundamental problem in X-ray imaging [41].

2.1.2 Breast MRI

A secondary imaging modality to mammography is breast MRI due to the ability to image high soft tissue contrast. However, it is only reserved for patients with high risk factors for developing breast cancer and/or ambiguous mammograms because the cost of MRI is much higher than mammgraphy. Besides the high soft tissue contrast, another advantage of breast MRI is that patients are not exposed to any ionizing radiation. Unlike mammography, breast MRI is highly favourable for women with dense breast tissue because imaging is based on the the tissue relaxation properties and proton density of the breast tissue.

MR Imaging is based on detecting hydrogen nuclei in the body (imaging of other nuclei with a magnetic moment such as carbon, phosphorus and sodium etc. is possible in MRI, but is not relevant to this thesis). The nucleus of the hydrogen atom consists of a single proton. Protons have an inherent spin property called the gyromagnetic

ratio (γ_H which is equal to 42.58 MHz/T)[1]. In the presence of a large static magnetic field (B_0), the protons will align parallel (with a small proportion of protons aligning anti-parallel) to the direction of the magnetic field (with net longitudinal magnetization and zero transverse magnetization) and precess with a frequency given by the Larmor frequency ω, in Eq. 2.1. In a 3 T magnetic field, protons have a Larmor frequency approximately equal to 128 MHz.

$$\omega = \gamma_H B_0 \tag{2.1}$$

In addition to precession in the magnetic field, protons are also sensitive to radio frequencies (RF) equal to the Larmor frequency and will absorb the corresponding energy from an externally applied RF pulse. An incident rotating RF magnetic field (B_1) induces a net transverse magnetization of the hydrogen nuclei. The amount of magnetization is given by the flip angle (α) prescribed in the MRI sequence and is dependent on the duration of the RF pulse. When protons absorb the RF pulse, they are in an unstable excited state and will relax to it's stable state by emission of an RF signal called the free induction decay. The time to recover the longitudinal magnetization is given by T1 and the time to return to zero transverse magnetization is given by T2. The sequence parameters and tissue characteristics determine the signal properties of the echo affecting the contrast in images. In general, there are three types of signal weighting in MRI, T1, T2- weighted and proton density images. Fat appears bright and water appears dark in T1-weighted images, and fat appears gray and water appears bright in T2-weighted images.

The signal detected in MR imaging is generated from an echo signal of the free induction decay. The echo can be derived from an RF pulse ($\alpha = 90°$) followed by an RF refocusing pulse ($\alpha = 180°$) a time TE (echo time) after the initial RF pulse. This type of sequence is called a spin echo (SE) sequence. Spatial localization of the echo signal is determined by three gradient coils, one for each axis. The echo is detected by RF receive coils that are tuned for maximum RF absorption. The gradient coils induce a linear magnetic field gradient in the MRI bore to localize the echo signal. The detected RF signals are stored in a k-space matrix based on the frequency and phase properties of the echo signal. The sequence is repeated until the k-space matrix is

[1]The gyromagnetic ratio is typically represented as 'γ'. However, due to the overlapping use of γ for gamma-ray imaging, the gyromagnetic ratio is represented with subscript H for the specific gyromagnetic ratio of hydrogen.

Figure 2.2: 16-Channel dedicated breast coil Sentinelle by Invivo [42].

filled and the time between each initial RF pulse is given by the repetition time (TR). Images in the spatial domain are reconstructed by applying a 2-D inverse Fourier transform to the k-space matrix. The echo can also be generated from the gradient coils instead of the 180° RF pulse.

In dedicated breast MR imaging, a specialized breast coil is used to optimize signal to noise ratio (SNR) and spatial resolution. The signal decreases with distance from the surface coils due to Faraday's law of induction, therefore SNR is maximized near the surface of the coil. Moreover, spatial resolution is improved for breast MR imaging as compared to whole body imaging due to a smaller field of view (FOV) .

The most common coil geometry used in breast MR imaging are surface coils (as shown in Fig. 2.2) in which the patient lies in a prone position with the breast pendant between the coils. The breasts are mildly compressed in the mediolateral direction. Images can be generated in any plane, however, the most common breast views are sagittal and axial.

Breast MRI typically uses dynamic contrast enhancement (DCE) with gadolinium to enhance cancerous lesions [22]. Gadolinium is a contrast agent with paramagnetic properties which highlights areas of blood flow. Development of cancerous breast tissue is associated with increased neovascularity and angiogenesis, therefore gadolinium tends to accumulate in tumours. MRI images are acquired pre- and post-contrast to observe the time intensity profile of the gadolinium uptake.

Breast MR imaging protocols differ depending on site-specific procedures, scanner and coil, however, the general template consists of a scout scan to localize the breast

within the coils, and pre- and post-contrast images, lasting approximately 45 minutes. The pre-contrast images consists of three initial scans. First, a T1-weighted gradient echo (GRE) sequence to highlight any morphological changes in the breast tissue. A T2-weighted spin echo (SE) with fat suppression is then prescribed to highlight potential fluid filled cysts. Third, a 3D T1-weighted fat suppressed GRE sequence is used to serve as a pre-contrast baseline. Fat suppression is used in the breast protocol because the breast is made up mostly of fatty tissue and fat resonates at a similar frequency to hydrogen (a 3.4 ppm chemical shift between fat and water corresponds to ~ 440 Hz difference at 3 T) resulting in a high signal which may affect the contrast observed in the non-fatty tissue. The post-contrast image is then acquired dynamically over a period of 8-10 minutes using the same image parameters as the 3D T1-weighted fat suppressed gradient echo sequence in the pre-contrast image. Subtraction of the pre-contrast image from the post-contrast image improves visualization of the gadolinium uptake. The resultant MR images are analyzed with the contrast enhanced image, the time intensity curve from the uptake and washout of gadolinium and the fat suppressed T2-weighted image [43–45].

The signal intensity over a defined region corresponding to a lesion will exhibit one of three characteristic curves as summarized in Fig. 2.3 where SI is the signal intensity pre-contrast and the SI_c is the signal intensity post-contrast. These time-intensity curves were established by Kuhl et al. for lesion-contrast characterization [46]. Lesions where the contrast enhancement gradually increases corresponds to a type I curve. This uptake profile is generally exhibited in benign lesions but has been reported in up to 9 % of malignant lesions [46]. The type II curve begins with a typical uptake but plateaus as time progresses. This suggests that lesions with this profile should be further investigated as 34 % of lesions were malignant with this profile in the study performed by Kuhl et al. [46]. Lastly, the type III curve exhibits a washout pattern in which the contrast enhancement significantly drops off. This is likely indicative of a malignant lesion and biopsies are recommended as outlined by Kuhl et al [46].

Studies have reported breast MRI sensitivity between 90 and 100 %, which is significantly higher than mammography [11–14, 20, 47, 48]. However, the inherent high spatial resolution and ability to display soft tissue contrast tends to highlight more detail in the breast which may appear cancerous, but is benign and/or inconsequential, resulting in an over-diagnosis of breast cancers. An increased uptake and a fast washout of gadolinium is typically indicative of an invasive cancer. However, it has been shown

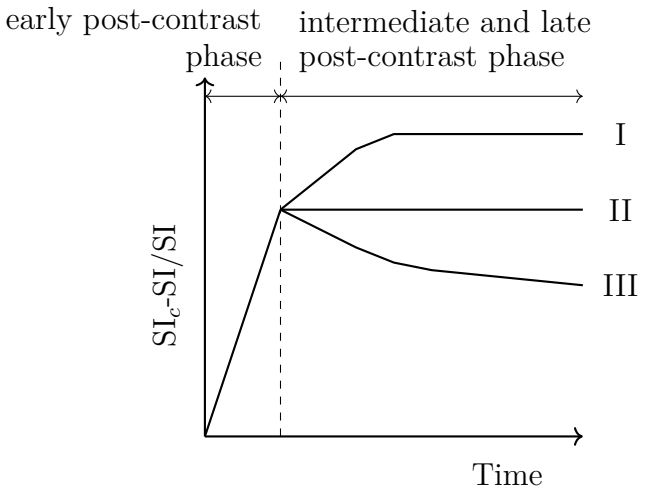

Figure 2.3: Time-signal intensity curves for breast MRI lesion enhancement (Reproduced from [46]).

that angiogenesis is not necessarily an indicator of a malignant lesion and that benign tissues can present with variable uptake profiles including ones similar to malignant lesions, resulting in lower specificity [18, 49]. While these studies suggest that false positives are an issue in MRI, there have been a number of studies addressing the screening efficacy of breast MRI with conflicting results indicated by the varying specificity results, ranging between 37-97 % [18, 19, 47, 50, 51]. In addition, a study by Baltzer et al. showed that breast MRI tended to present with high specificity when related to mass lesions (image enhancements with defined boundaries) versus low specificity with non-mass lesions (image enhancements with no defined boundaries) [52]. This indicates that despite the consistent high sensitivity of MRI, specificity tends to vary between studies.

MR spectroscopy is sometimes used to improve the specificity from a standard DCE-MRI. MR spectroscopy measures the relative signal of compounds which resonate during RF excitation without the readout gradient. Similar to hydrogen, metabolites also resonate during the RF excitation but with different frequencies. Since the water and fat signal dominates the spectrum, it must be suppressed to view the presence of metabolites. Studies have suggested that elevated levels of choline were associated with tumour malignancy [51, 53–55]. While an increase in choline is observed in malignant tumours, it was also observed in benign tumours [22, 52] resulting in mixed results for specificity improvement. This method is not included in standard breast MR protocols

due to this variability, but is implemented on a case by case or study basis for pre- and post-surgical comparison of the observed choline concentration.

2.1.3 Molecular breast imaging

While molecular breast imaging is a relatively new imaging modality, it's history dates back to the early 1990's when it was indirectly discovered that there was preferential uptake of Tc-99m sestamibi (also known as Tc-99m MIBI) in malignant breast tissue during cardiac imaging [56, 57]. Dedicated breast imaging (scintimammography) followed soon after [58, 59]. Tc-99m MIBI is a radioactive tracer with a half-life of 6 hours, emitting a 140 keV gamma-ray (89 % abundance) that is commonly used for cardiac perfusion imaging. It is named as such because the radioisotope component (Tc-99m) is bound by six methoxyisobutylisonitrile (MIBI) ligands. Tc-99m MIBI is a cation which accumulates in the mitochondria via passive diffusion across the mitochondrial membrane potential. The uptake of Tc-99m is thus greater in cancerous tissues which exhibit greater mitochondrial concentration [60, 61].

The Tc-99m MIBI uptake also correlates with blood flow to determine areas of infarct and/or ischemia in cardiac imaging. Angiogenesis is a potential indicator for malignant cancers because tumours require an abundance of vasculature for cell proliferation [62]. Given that Tc-99m MIBI is used to image cardiac blood flow, it is not surprising then that Tc-99m is taken up in areas of high angiogenesis in the breast tissue. Both processes involving uptake in the mitochondria and measuring blood flow increases the specificity of MBI.

In MBI, the breast is placed between two opposing, small field of view, gamma cameras and is mildy compressed to minimize the amount of scattering tissue. The latest MBI systems utilize the solid-state detector CZT as the main detection element in the gamma camera, which offers superior energy and spatial resolution as compared to traditional gamma cameras. An example of a CZT based gamma camera is shown in Fig. 2.4. Projection images of the radiotracer uptake are generated by detection of gamma rays in the CZT detector (further explanation of gamma ray detection in CZT will be discussed in the following section). A collimator is typically made of lead and absorbs scattered photons that are not parallel to the holes. The spatial localization of each detected gamma ray and the corresponding detected energy is processed in the readout electronics. A pixel map of the detected photons make up the projection image.

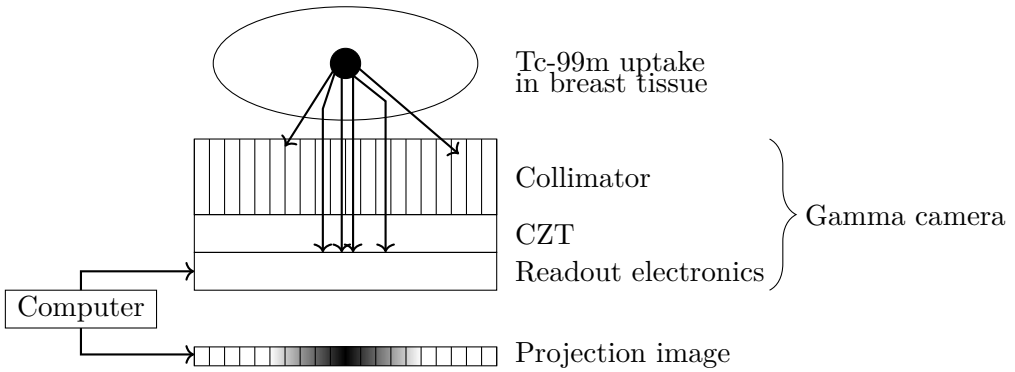

Figure 2.4: Gamma camera components in MBI (Only one gamma camera pictured).

In a typical MBI procedure, the patient is injected with a standard dose of 740 MBq (20 mCi) of Tc-99m MIBI and the 140 keV emissions from the radiotracer uptake is detected by the gamma camera resulting in projection images. The two views that are acquired in a typical MBI protocol, namely CC and MLO, are the same as the mammography views, and a typical MBI exam takes approximately 40-50 minutes (10 mins/view/breast). MBI is not used as a screening option for the general population because the administered dose exposes the patient to an effective dose of approximately 6.5 mSv, which is significantly greater than mammography [20, 25, 63]. While this dose is low in comparison to other nuclear imaging techniques, it is considered high for screening purposes.

Early variations of molecular breast imaging were referred to as scintimammography and breast-specific gamma imaging. The different terms used to differentiate and describe different scintigraphic breast imaging[2] techniques are shown in Fig. 2.5. In scintimammography, the gamma camera is composed of traditional detector components (scintillator coupled to a photodetector) to image the uptake of Tc-99m. Specific details of gamma camera design and operation will be discussed in the following section. The patient would be positioned prone on a table with the breasts pendant with the gamma camera adjacent to the table. Patients were injected with 925 MBq (25 mCi) of Tc-99m and images were obtained without any breast compression. Breast specific gamma imaging (BSGI) was the next iteration of scintigraphic breast imaging systems and is sometimes referred to as MBI. It bears more similarities to the current MBI system in

[2]The term 'scintigraphic' imaging has long been used in nuclear medicine to describe planar gamma imaging but is ambiguous with the development of direct detection gamma cameras. For the purposes of this thesis, planar imaging with CZT gamma cameras may be referred to as 'scintigraphic' imaging.

that the patient is seated upright with the breast compressed with small field of view gamma cameras. On one side is the detector and the other side is a plastic paddle to minimize the amount of scatter from the breast. The administered dose is similar to scintimammography, ranging from 925-1110 MBq (25-30 mCi) and resulting in an effective dose of 7.8-9.4 mSv [26, 64].

Figure 2.5: Variations of scintigraphic breast imaging systems (L-R: Scintimammography [65], breast specific gamma imaging -Dilon 6800 [66], and molecular breast imaging - GE Discovery NM750b [67])

In contrast to the previous iterations of dedicated molecular breast imaging detectors, the new MBI systems are made from the latest CZT detector technology which boasts exceptional energy resolution and improved detector sensitivity compared to standard gamma cameras, thereby allowing decreased administered dose. In addition, MBI features a dual-head design so that the maximum distance from the breast tissue to the detector is half the thickness of the breast, thereby improving detection sensitivity. The frequency of scintimammography and BSGI use are decreasing due to the advent of newer technologies with CZT based imaging systems, lowered dose requirements, and superior image quality.

2.1.4 Other Breast Imaging Modalities

Besides mammography, breast MRI and MBI, some of the other breast imaging options are positron emission mammography (PEM), PET, CT, ultrasonography, and thermography.

PEM is similar to MBI in that two planar gamma cameras are used to image the gamma rays emitted by the uptake of a radioactive tracer, except that a positron emitter (typically F-18 tagged to glucose, commonly known as fluorodeoxyglucose (FDG)) is injected into the patient instead of a gamma emitter. Glucose preferentially accumulates in cancerous tissue because higher glucose metabolism is required for cancerous tissue growth.

The gamma cameras detect the coincident 511 keV gamma rays emitted 180° apart after the positron annihilates with an electron. Since event detection in PET is based on the timing of two coincident gamma rays, a physical collimator is not necessary as it is with SPECT or planar scintigraphic imaging. The primary concern is the high effective dose associated with PEM. A typical PEM scan requires an administered dose of 370 MBq of FDG resulting in a 6.7 mSv effective dose, similar to MBI [64, 68]. The whole body equivalent of positron imaging (PET) uses a full ring of detectors but is only used for cancer staging post-diagnosis and for treatment monitoring because the spatial resolution of whole body PET limits the ability to detect small lesions. The administered dose is similar to PEM but since most PET scans are performed with CT for attenuation correction, the effective dose is 2-5 times higher than for PEM alone [69]. A drawback to both PEM and PET is the limitation of imaging only one radioisotope, whereas planar gamma imaging or SPECT is capable of imaging multiple isotopes simultaneously.

Breast CT creates a fully 3-dimensional reconstruction of the breast using X-ray projections spanning 360° around the chest region of the patient instead of a limited range as in digital breast tomosynthesis. One of the main drawbacks of breast CT is the high effective dose (5-18 mSv [25]). Breast CT is currently being used for breast cancer staging, radiotherapy treatment planning and perioperative imaging. Development of dedicated breast CT imaging with cone-beam geometry offers a lower dose option (similar to mammography) for high resolution diagnostic imaging. Results from CT were comparable to mammography but visualization of masses were better using CT than with mammography and conversely, mammography was better than for imaging microcalcifications than with CT [70–73]. Dedicated breast CT may become an alternative imaging method to mammography but clinical implementation is still in it's infancy [26].

Breast ultrasonography is one of the most common modalities used second to mammography due to it's relatively low cost. It is typically prescribed if breast MRI is

unavailable, radiation exposure must be limited, or some other patient contraindication is present. Breast ultrasonography uses sound waves in the 5-10 MHz range to produce images of the breast. The preferred frequency depends on the desired depth of penetration and image resolution. As frequency increases, resolution increases but depth of penetration decreases. Ultrasound transducers convert electrical signals to sound waves and vice versa. Sound waves produced from the transducer travel through breast tissue and can either be absorbed, scattered, reflected or transmitted. The reflected wave is what is detected in the ultrasound transducer. Using the speed of sound in tissue ($\sim$1540 m/s) and the time it takes the echo to return, the distance between the ultrasound probe and depth at which the wave was reflected can be determined. This information is displayed in a B-mode (also known as brightness mode) image and is the most common imaging view in ultrasound. The image is a 2-dimensional representation of the cross sectional plane covered by the transducer. The brightness of each pixel correlates with the strength of the echo signal and the pixel location correlates with the depth from the transducer. Ultrasound can be used to measure blood flow which may provide more insight into the vascularization of a breast lesion using a property called the Doppler shift. The Doppler shift occurs when the echo is reflecting off of a moving object such as blood. The frequency increases when the blood is travelling towards the transducer and decreases away from the transducer. Doppler ultrasonography highlights blood flow by measuring the change in the frequency when the waves are reflected. Studies have shown that Doppler ultrasonography can be useful in characterizing potentially malignant breast lesions but this method can not explicitly differentiate malignant versus benign lesions [74–77]. Ultrasound is best used to investigate blood flow, lumps and fibroadenomas as a low cost breast imaging modality compared to breast MRI. However, due to the manual nature of this imaging technique and the absence of a universal scanning protocol, results are highly dependent on operator performance leading to variable sensitivity and specificity [11, 14, 78–80].

Breast thermography (also known as digital infrared thermal imaging) uses infrared detectors to detect heat on the surface of the breast. This method is based on the idea that an increase in blood supply generates heat, and therefore heat is detected in regions of significant tumour angiogenesis. A 2001 study on thermography reported 54 % sensitivity and 67 % specificity suggesting thermography is more accurate for women without breast cancer [81]. There have not yet been any studies indicating

any concrete evidence of breast cancer detection [82, 83]. Therefore, it is not accepted as a means for breast cancer detection but is noted as a modality recognized by the Canadian Association of Radiologists.

2.1.5 The current status of breast MBI

While each modality has it's own set of advantages and disadvantages, MBI is emerging as a new imaging technique which has potential to contribute significantly in the diagnosis, treatment planning, and monitoring of breast cancer with the majority of MBI development emerged from the early 2000's [84, 85]. Current research in MBI is focused on dose reduction through both hardware and software methods, and utilizing MBI images along with other imaging modalities to help improve breast cancer diagnosis. Based on radiation dose estimates, the main concern is the dose to other organs due to high absorbance of Tc-99m in the gallbladder, small and large intestines, kidneys and urinary bladder wall from Tc-99m MIBI [86].

Early developers of the modern MBI system have investigated low dose MBI (300 MBq vs 740 MBq) by optimizing collimator parameters and increasing the photon energy acceptance window. The modified collimator was matched to the pixel size for optimal gamma ray detection [64, 87]. The standard acquisition window width is ±10 % around the photopeak. Inherent properties of CZT such as charge sharing, cross-talk, and trapping result in incomplete charge collection, which is primarily observed in the low-energy tail of the energy spectrum. Hruska et al. compensated for this effect by extending the low energy threshold to -20 % from the photopeak and demonstrated improvements in count sensitivity and lesion contrast [64, 87]. A recent study investigated by Rhodes et al. revealed that the diagnostic accuracy of MBI at low dose (300 MBq) using the optimized collimator and the extended energy acceptance window was equivalent to the standard dose (740 MBq) but decreased the effective dose from 6.5 mSv to 2.4 mSv [21]. Using MBI with these optimized parameters and in conjunction with mammography, sensitivity increased by 24 % to 91 %, but specificity decreased from 89% for mammography alone to 83% combined. Individually, the modalities resulted in higher specificity with 89 % to 91% for mammography and MBI respectively [21]. Researchers are striving to achieve less than or equal to a 150 MBq administered dose which would correspond to an effective dose of less than 1.3 mSv [20] making the dose comparable to mammography.

MBI has also been used to supplement images from breast MRI and mammography

to improve grading and diagnosis of breast cancers. A study performed by Golan et al. showed that the initial number of true positives from MRI were increased with the complementary MBI images [88]. In addition, Duarte et al. also noted the benefits of combining MBI with MRI, and demonstrated that the estimated tumour size from using both modalities was more accurate than mammography, clinical breast exams, and MRI alone [89]. In both studies, the authors showed the feasibility and benefits of fusing MBI and MRI images which were acquired sequentially. Simultaneous imaging offers the benefits of improved image registration and shorter patient scan time. In addition to high risk screening, dual-modality imaging may be beneficial for pre-surgical breast cancer planning.

2.2 Combined MBI/MRI Imaging

The general concept of dual-modality imaging systems aims to address the drawbacks of each modality by complementing one with the other. Given the current status of breast imaging technology, developing a dual-modality imaging system could be a beneficial and cost-effective alternative for women in screening, treatment planning, and post-surgical imaging.

Recent advances in semiconductor technology have led to significant progress in the development of dual-modality imaging systems combining nuclear medicine with MRI [90–98]. While most of these developments have been directed at PET/MR using avalanche photodiodes or silicon photomultipliers, there has been some interest in developing SPECT imaging systems. SPECT/MR development has often made use of CZT detectors because of the high detection efficiency of lower energy SPECT tracers. For example, Hamamura et al. developed a custom birdcage coil for simultaneous SPECT/MR imaging using a CZT based gamma camera with a 4 T MRI with minimal impact on the gamma camera performance, but observed a 50 % decrease in SNR in the MRI images [99]. In a separate study, Tsui et al. developed both an RF birdcage coil and a ring of CZT detectors coupled to multi-pinhole collimators for simultaneous small animal SPECT/MR. The custom SPECT system was inserted into a 3 T MRI and their results indicated simultaneous imaging was feasible [90]. These examples show that with the advent of improved semiconductor technology, studying both biological processes and anatomical structures through simultaneous imaging is a possibility. However, these configurations required the use of custom RF coils and/or have been

aimed towards small animal imaging. MR-compatible planar scintigraphic systems such as MBI offer the ability to perform dual-modality breast imaging at a much lower cost than a whole body SPECT/MR system as well as the improved performance typically observed with dedicated imaging.

There are some important factors to consider in the design of an MR-compatible gamma camera. First is the compatibility of the detector and associated electronics within the main magnetic field, the switching gradients and/or RF when inside the MRI bore. Second, one must be mindful of the space available for both the patient and any additional equipment. The goal is to minimize the impact on the current MRI system, as some dual-modality designs require permanent modifications to the MR coil and/or bore. Third, the gamma camera must not negatively affect MRI performance.

Traditional gamma cameras are unable to function inside the MRI scanner because of the method of photon detection. They consist of a scintillator such as thallium doped sodium iodide (NaI(Tl)) coupled to a photomultiplier tube (PMT) as shown in Fig. 2.6. PMTs are not compatible in magnetic fields due to the fundamental principles of how the signal is obtained. High-energy gamma-rays are converted to visible light photons via a scintillator. The visible light photons then eject photoelectrons off the photocathode of the PMT. These photoelectrons are then accelerated across large voltage potentials called dynodes. According to the Lorentz force, a charged particle (such as an electron) with velocity v, experiences a force F, when in the presence of an electric field E, and a magnetic field B as shown in Eq. 2.2.

$$F = qvBsin\theta + qE \tag{2.2}$$

In the absence of a magnetic field, only the electric field contributes to the force on the electron resulting in a net force, targeting the electrons to the next dynode. However, in the presence of magnetic fields, the electron trajectory will tend to the direction perpendicular to the magnetic field thus affecting the electron collection at each dynode and ultimately, the PMT output.

An alternative photodetector which is relatively new for medical imaging applications are semiconductor detectors and are compatible in magnetic fields. In the past decade, there has been extensive research and development in semiconductor technology which has paved the way for combining nuclear medicine imaging with MRI. There are a number of semiconductor detectors on the market; however, those in the germanium family require extensive cooling with liquid nitrogen to operate

reliably and accurately. Silicon based detectors such as silicon photomultipliers have been and are continuing to be investigated for PET/SPECT detector development due to their high detection efficiency when coupled with a scintillator such as lutetium-yttrium oxyorthosilicate (LYSO) or thallium doped cesium iodide (CsI(Tl)). Silicon photomultipliers use Geiger-mode avalanche photodiodes as the basis of their structure. Another type of semiconductor is CZT and one of its many advantages is that it is relatively stable at room temperature [100–102], which means that it does not require active cooling, unlike many other semiconductor detectors.

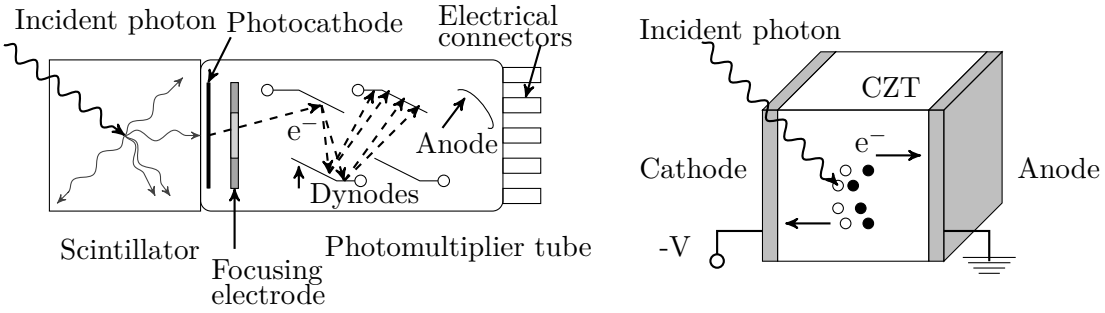

(a) Cross section of a scintillator coupled to a photomultiplier tube

(b) Cross section of CZT

Figure 2.6: Gamma ray detection in a scintillator/PMT versus CZT

The advantage of using CZT in gamma cameras as opposed to a scintillator coupled to a photodetector is the direct detection of high energy gamma-rays. Gamma rays interacting within the CZT generates 1 electron-hole pair per 4.5 eV of energy deposited, this is equivalent to 31 000 electron-hole pairs for a 140 keV gamma-ray. On the other hand, PMTs require a scintillator to convert the high-energy gamma-rays to visible light photons and these photons go on to eject electrons off a photocathode in the PMT with 15-20 % efficiency. The yield is approximately 1000 photoelectrons for a 140 keV gamma-ray, which is significantly less than CZT. Based on photon counting statistics, this corresponds to an ideal energy resolution of 5 % for PMTs and 0.1 % for CZT. The theoretical resolutions are not realizable due to noise and scintillator defects leading to non-uniform light collection for PMTs and charge trapping, charge sharing, leakage current and pixel cross talk in CZT. Realistically, CZT has an energy resolution of 3-6 % at room temperature compared to 7-10 % with PMTs at 140 keV [103, 104].

The magnetic field has minimal effect on the electron trajectory in CZT because the distance traversed is much shorter than in PMTs (<5 mm in CZT versus several

centimetres in PMTs). If the CZT is positioned in any orientation except parallel to the main magnetic field, electrons will experience a Lorentz shift. CZT detectors have been tested in high magnetic fields (4-7 T) without any effects in CZT performance except the Lorentz shift was observed when the CZT was positioned perpendicular to the main magnetic field [97, 105, 106]. Therefore, semiconductor technology offers the ability to pursue dual-modality imaging with MRI due to the ability to operate within a magnetic field.

The entire system including the accompanying electronics must be shielded to prevent any interference between the gamma camera and the MRI system and vice versa. MR gradients may induce noise in the CZT/electronics and likewise, the time varying RF and gradient switching may induce unwanted effects in the CZT detector. Shielding of RF is typically accomplished by use of a Faraday cage. A Faraday cage is made of a conductive material enclosing the object to be shielded. The charged particles in the conductor are re-distributed along the perimeter of the cage to cancel out the effects imposed by the extraneous RF from both inside and outside the cage. Copper is the most common shielding material used and is even used to shield the MRI room. However, conductive materials are susceptible to induced eddy currents inside the MRI which in turn affect the magnetic field homogeneity. An alternative material shown to possess good RF shielding while being transparent enough for gamma-ray penetration is carbon fiber. While carbon is conductive, studies have shown that the geometry of carbon fiber results in sufficient RF shielding preserving semiconductor detector performance inside a 3 T and 7 T MRI system [107–109].

In addition to RF shielding, the magnetic field homogeneity (MFH) is crucial to MRI performance as it is the basis to reliably reconstruct anatomical structures. The uniformity of the magnetic field dictates where the signal is detected from, to reliably reproduce the imaged object. Every material has some degree of magnetic susceptibility, which describes the degree of magnetization in the presence of a magnetic field. Ferromagnetic materials such as iron or nickel have a very large magnetic susceptibility, with a strong attraction to magnetic fields and may retain magnetization after removal of the magnetic field. These materials must be avoided inside the MRI room, as they will distort the magnetic field resulting in poor image quality, as well as presenting a physical hazard. The effect on the MFH in the isocentre/imaging volume is dependent on the material property, geometry and the distance from the isocentre. The B_0 field is shimmed prior to imaging in order to optimize the MFH, although

it is impossible to achieve a perfectly homogeneous field. The MFH is generally expressed in terms of parts per million (ppm) or in frequency (Hz) over a specified region of interest. Generally, the recommended criteria for MFH is 1.5 ppm peak to peak (approximately 0.5 ppm root-mean-square) over a 35 cm diameter spherical volume (DSV) [110], however most clinical systems are able to achieve less than 1 ppm. At 3 T, this corresponds to a maximum shift ($\Delta\omega$) of $\sim$128 Hz (or $\pm$63.87 Hz). Significant shifts beyond 1.5 ppm in the magnetic field homogeneity can manifest itself as loss of signal and/or geometric distortions. Loss of signal may influence the ability to accurately diagnose and/or delineate potential lesion boundaries. In addition, geometric accuracy is critical in standard anatomical MRI imaging because its ability to accurately reconstruct anatomical features is crucial to the diagnosis of various diseases.

2.3 Backscatter Imaging in MBI

Dose reduction methods in MBI remain a key objective if it is to be considered for more frequent use in screening and supplementary imaging with mammography. Hardware and software improvements to MBI systems over the past few years have led to a 60 % decrease in administered dose [87] and researchers anticipate that dose could decrease an additional 30 % from the original recommended dose [20]. This work has contributed significantly to the increased use of MBI, but the effective dose remains high relative to mammography. In an effort to pursue further dose reduction in MBI, a software based scatter compensation method was investigated in order to increase count sensitivity by extracting backscatter photons from data that is typically discarded in a nuclear medicine imaging study.

Backscatter photons was first used with X-rays as a low-dose imaging method based on projecting X-rays to the object of interest and detecting the photons which undergo a 180° scatter rather than measuring the penetration through the object [111]. These backscatter photons preserve the same spatial information as primary photons except that the photon is not attenuated through the object of interest, instead the photons are reflected off the object surface back into the detector. More recently, backscatter imaging has become popularized for its use in security screening [112, 113]. The principle of backscatter imaging is proposed to supplement images generated from primary photons with the addition of backscatter photons to increase the count

sensitivity and improve image quality so that dose may be reduced.

Unlike conventional planar X-ray imaging or CT, the origin of the radiation source is unknown in nuclear medicine. In order to reliably determine the location of radiotracer uptake, imaging is based on detecting photons which travel parallel to the collimator. The primary photons detected can be discriminated through energy windowing. Backscatter photons relay the same spatial information as primary photons, but they are obscured by the remaining Compton scatter photons that degrade spatial resolution and contrast. In a separate investigation, Kadrmas et al. used scattered photons to reduce noise levels in SPECT images and it was suggested that there may be merit in investigating backscatter photons due to a similar response function to primary photons [114].

Nuclear medicine images are derived from photons within an energy window centered around the photopeak/gamma-ray emission energy. All other scattered photons are discarded since scattered photons degrade spatial resolution and contrast. For a photon with a specific energy interacting within a given medium, photons can be either transmitted, scattered or absorbed. The fraction of photons that are removed from an initial photon beam per unit distance is given by the attenuation coefficient. The attenuation coefficient (μ) is governed by the sum of the individual interaction probabilities from Rayleigh scattering, photoelectric effect, Compton scattering and pair production, denoted by R, τ, σ_C and κ respectively (Eq.2.3). [3]

$$\mu = R + \tau + \sigma_c + \kappa \tag{2.3}$$

In Rayleigh/coherent scattering, the photon interacts with the whole atom and is deflected at an angle with essentially the same energy. The amount of energy absorbed by the atom is negligible compared to the energy of the incident photon. The probability of this interaction is low and is only relevant for energies less than 50 keV. Since there is no transfer of energy, this interaction is not applicable to nuclear medicine imaging.

Pair production is the generation of an electron and positron pair which requires a minimum photon energy of 1.022 MeV, equivalent to the rest mass of an electron and positron (511 keV each). This process is not relevant because it exceeds the energy

[3]The Compton interaction probability is typically denoted as σ but this symbol is also used to describe the scattering cross section and the standard deviation in a Gaussian distribution. Therefore, a subscript c is used to indicate the intended Compton interaction probability.

range used in MBI ($\sim 140\,\text{keV}$).

The photoelectric effect is one of two main interactions in nuclear medicine. The photoelectric effect (shown in Fig. 2.7) occurs when the incident photon with energy E_γ, is completely absorbed in a material with atomic number (Z) and ejects an electron. The energy of the ejected electron E_e is equal to the the difference between the incident photon energy and the binding energy E_b (energy required to remove the electron from the atom). When a photoelectric interaction occurs, an electron is ejected and the fast moving moving particle is absorbed a short distance later due to the linear energy transfer properties of electrons. If the electron is ejected from an inner shell, an electron from the outer shell will fill the inner shell vacancy so that the atom can return to it's stable state. The excess energy from changing electron shells is converted to electromagnetic radiation in the form of a characteristic X-ray or an Auger electron. The probability of a photoelectric interaction is proportional to Z^3/E_γ^3, therefore photoelectric effect dominates with high Z materials and lower energy gamma rays. Photoelectric interactions are dominant in the main detection element of the gamma camera because CZT has a large atomic number ($Z_{eff} \approx 50$). Gamma emissions that travel parallel through the collimator and undergo photoelectric interaction with the gamma camera generates image contrast thus providing useful image information for interpretation. However, photoelectric absorption can also occur in tissue, but with a higher probability at lower energy. The deposition of energy from fast moving charged particles in tissue therefore contribute to the patient absorbed dose.

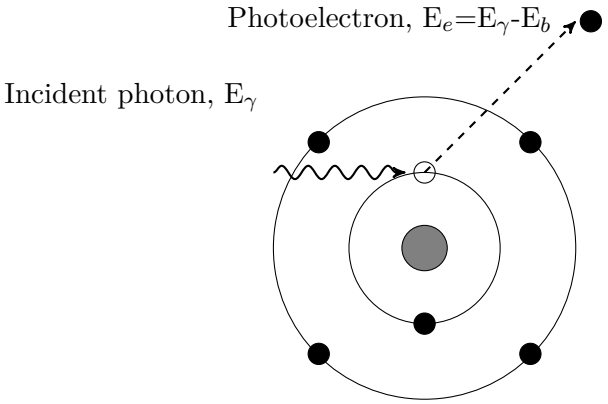

Figure 2.7: Photoelectric effect

The second main interaction in nuclear medicine is Compton scattering. Compton scattering is an inelastic scattering process in which the incident photon interacts with

a loosely bound valence electron. The binding energy must be negligible in comparison to the photon energy for Compton scattering process to occur. Some or most of the energy is transferred to the recoil electron as shown in Fig. 2.8. The energy of the scattered photon is governed by the Compton scattering equation (Eq. 2.4) where θ is the scattering angle, E_γ is the energy of the incident photon and E_γ' is the energy of the scattered photon.

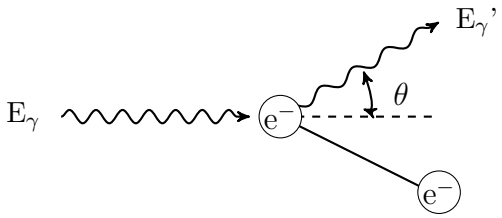

Figure 2.8: Compton scattering

$$E'_\gamma = \frac{E_\gamma}{1 + \frac{E_\gamma}{0.511}(1 - cos\theta)} \tag{2.4}$$

Compton scattering is a dominant interaction in the body because of the presence of scattering material for photons to interact with. These scattered photons lead to decreased contrast because the origin of the gamma emissions do not correlate with the detected location. However, photons scattered 180° from the incident photon are said to be backscattered and have the same spatial information as primary gamma rays but with lower energy as illustrated in Fig. 2.9.

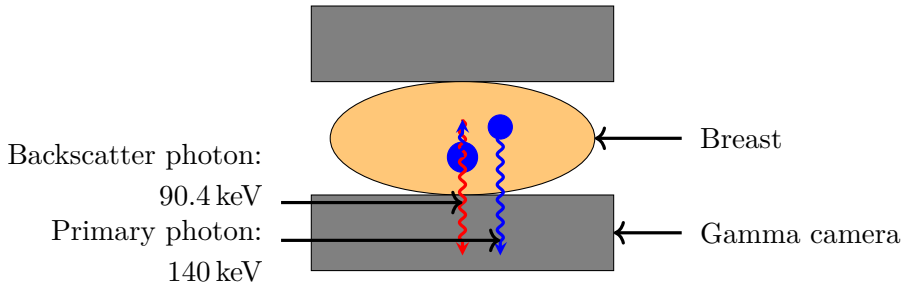

Figure 2.9: Backscatter versus primary photon using Tc-99m in molecular breast imaging.

Recall that the radiotracer used in MBI is Tc-99m and the primary emission is 140 keV gamma rays. The backscatter photon energy according to the Compton scattering equation is 90.4 keV and the remaining 49.6 keV is transferred to the ejected

electron. If the interaction occurs in the tissue, the backscatter photon corresponds to the 90.4 keV deposited in the detector. However, a backscatter event in the detector would result in a 90.4 keV photon scattered out of the detector and 49.6 keV transferred to the Compton electron and deposited into the detector. All instances of backscatter herein refer only to the detection of the backscattered photon and not the Compton electron. The angular distribution from Compton scattering is given by the Klein-Nishina differential scattering cross section in Eqn. 2.5, where the differential cross section $d\sigma_{KN}/d\Omega$ gives the effective area available for scattering over an infinitesimal solid angle with angle θ, and electron radius r_o is 2.818×10^{-15} m.

$$\frac{d\sigma_{KN}}{d\Omega} = \frac{r_o^2}{2}(\frac{hE'}{E})^2(\frac{E'}{E} + \frac{E}{E'} - sin^2\theta_\gamma) \tag{2.5}$$

The probability of Compton scattering is proportional to the total cross section and the electron density given in Eq. 2.6. The probability of Compton scattering is proportional to the total cross section and the electron density where A is the atomic mass, ρ is the density, and N_A is Avogadro's number.

$$\mu = \frac{\sigma A \rho}{N_A} \tag{2.6}$$

At low energies, the differential cross section approaches the Thomson scattering limit of 79 mb (area of an electron). Higher energy photons tend to be more forward directed due to a smaller cross section and therefore have a lower probability of backscattering, whereas low energy photons will approach the Thomson limit of equal probability of both forward and backward scattering.

The relative probability of a 140 keV gamma ray interacting as a function of the scattering angle according to the KN scattering equation is shown in Fig. 2.10. The limit of the scatter probability for the incident photon is 79.4 mb/sr, defined by the Thompson scattering probability and the corresponding probability for a backscatter photon with incident energy of 140 keV is 35 mb/sr. This corresponds to a 44 % likelihood of a backscatter event as compared to forward scattering.

It is postulated that the inclusion of backscatter photons would improve image quality or provide the same image quality with decreased dose to the patient since backscatter photons have the same spatial information as primary photons. However, there are a few limitations that currently prevent the use of backscatter photons in nuclear medicine imaging studies. First, the backscatter photons are located within

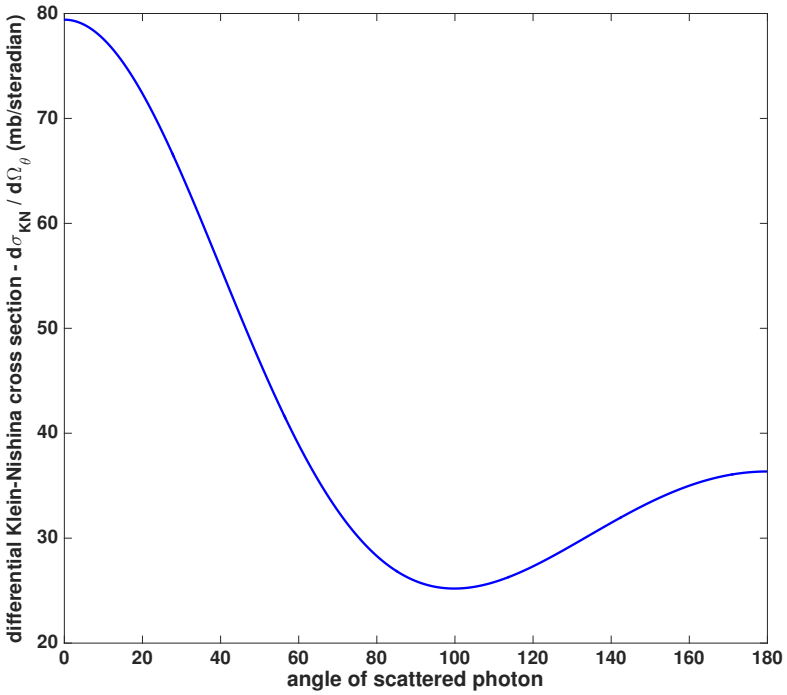

Figure 2.10: Klein-Nishina differential scattering cross section as a function of scattering angle.

the scattered portion of the energy spectrum with both single and multiple Compton scatters, and lead characteristic X-rays from the collimator and shielding materials. In addition, there is an overlap of backscatter photons with other wide angle Compton scatter photons due to the energy resolution of the gamma camera system. The backscatter photons must be separated from the rest of the scatter spectrum in order to make them useful and contribute to the photopeak data.

A scatter compensation method must be investigated to extract the backscatter photons. There are two main types of scatter compensation methods, spatial-based scatter models derived experimentally or from Monte-Carlo simulations, and energy distribution-based methods [115, 116]. Spatial-based scatter models involve the deconvolution of the scatter response function with the projection image. Since the scatter response function is different from that in the photopeak window, development and validation of a scatter model either experimentally or through Monte-Carlo simulations would be required for investigation of backscatter photons. In terms of the window-based correction methods, The most common subtraction-based scatter

methods are the dual-energy and triple energy window methods [116]. The dual-energy window scatter correction method estimates the scatter fraction based on an energy window set below the the photopeak window. This method does not account for higher energy scatter into the lower window and is therefore inappropriate for investigating backscatter photons. The triple energy window uses three energy windows, one for the main photopeak and two subwindows, one above and one below to estimate the scatter portion. The scattered photons are subtracted on a pixel by pixel basis. A TEW-based approach was proposed to isolate backscatter photons from the spectrum of scattered photons due to its relative ease of implementation and it's relative accuracy in comparison to the computationally intensive Monte-Carlo scatter models.

2.3.1 Triple Energy Window Method

The TEW compensation method was introduced by Ogawa et al. in 1991 [117] and was originally developed for dual isotope imaging to remove down-scattered photons into the lower energy peak. TEW is based on estimating the scatter contribution using a trapezoidal approximation using two small scatter windows abutted to the main photopeak window as illustrated in Fig. 2.11. The number of counts in these subwindows are scaled and subtracted from the total counts in the main window. This method can be applied to the higher energy emitting isotope in dual isotope imaging, but since there are no scattered photons with energy larger than the primary gamma-ray, the TEW method can be simplified to the dual energy window scatter correction, as the number of counts in the upper scatter window tends to zero [118].

The estimated number of photopeak photons C_{P1} is given by Eqn. 2.7 where C_{M1} is the total counts in the main peak window with window width, W_{M1}, C_{L1} is the total number of counts in the left subwindow of window width W_{L1}. Similarily, the estimated number of backscatter photons C_{P2} is determined using the same method except the counts (C_{R2}) in the upper scatter window W_{R2} is included in the scatter estimation given by Eqn. 2.8.

$$C_{P1} = C_{M1} - \left(\frac{C_{L1}}{W_{L1}}\right).\frac{W_{M1}}{2} \tag{2.7}$$

$$C_{P2} = C_{M2} - \left(\frac{C_{L2}}{W_{L2}} + \frac{C_{R2}}{W_{R2}}\right).\frac{W_{M2}}{2} \tag{2.8}$$

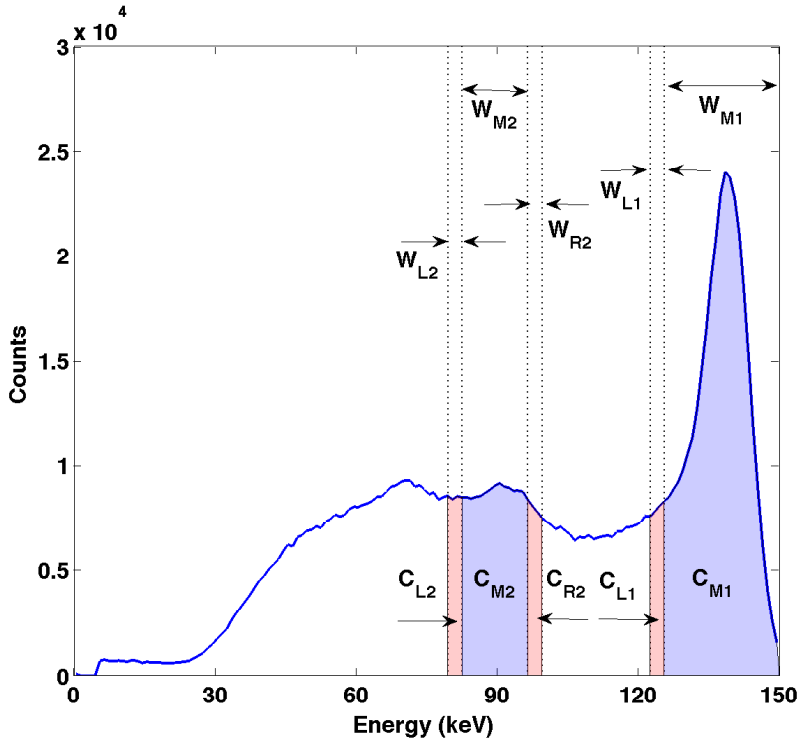

Figure 2.11: Tc-99m spectrum of a simulated line source in a phantom with 5 cm forward and 5 cm back scatter material (phantom density = 1.02g/cm^3).

The spectrum above represents simulated data from a Tc-99m filled line source within a phantom consisting of 5 cm of forward and 5 cm of backscatter breast tissue showing a defined backscatter peak. In a separate study, de Jong et al. investigated the contribution of backscatter in dual isotope imaging from the Tc-99m 140 keV peak into the Tl-201 72 keV peak. They determined that an additional 10 % of counts contaminated the lower energy photopeak but their analysis of backscatter photons included all photons scattered $\geq 90°$. Moreover, they showed that the effect of backscatter photons plateaued beyond 5 cm of backscatter material [119]. In this thesis, the term backscatter is used exclusively for 180° scattered photons and photons within the defined backscatter energy window, unless otherwise stated. For a defined scattering medium, it is expected that the backscatter photon yield will increase as the amount of backscatter material increases, but beyond 5 cm, the increase in the number of photons is expected to plateau due to the exponential decrease from photon attenuation.

Chapter 3

Design of a Gamma Camera for Combined Molecular/MR Breast Imaging

This chapter presents the design and details of the hardware and software development of the proposed gamma camera system for combined MBI/MRI.

3.1 Hardware Development

The gamma camera consists of the CZT modules, a custom made digital readout board (DRB), power distribution board, microcontroller, heat sink, lead collimator and shielding. Fig. 3.1 shows a cross section of the gamma camera.

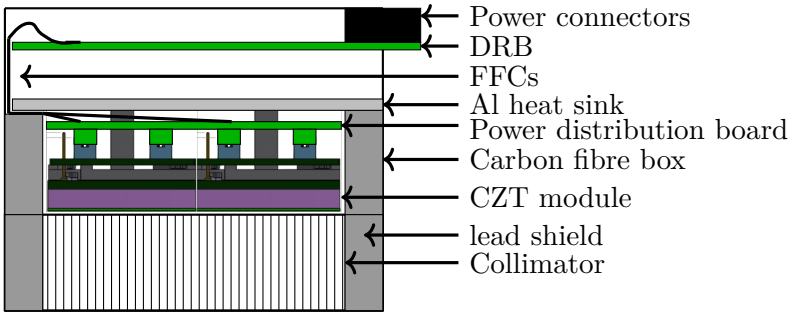

Figure 3.1: Cross section of the gamma camera (Not drawn to scale).

A concern regarding the magnetic field homogeneity (MFH) and the gamma camera design is the requirement of a significant amount of shielding material to prevent scattered photons from entering the detector. A lead collimator was required to discriminate against scattered photons and solid lead was used to attenuate gamma rays from entering the sides of the detector. In addition to the lead, the gamma camera also consisted of several pieces of semiconductor/metallic materials which may be susceptible to induced eddy currents and/or distort the magnetic field homogeneity. Every effort was made to minimize magnetic field inhomogeneities, however some of the components were unavoidable because they were crucial to the operation of the gamma camera. Therefore, evaluation of the MR performance will determine the extent of image degradation, if any. The collimator was made from a low energy high resolution lead collimator (Elscint MSC-4) fitted to cover the camera FOV. The collimator was 2.54 cm thick, with hexagonal holes of inradius 0.55 mm and the modules were surrounded by 7 mm of lead to prevent scattered photons from entering the sides of the modules. The whole system was encased in a 3 mm thick carbon fibre box with outer dimensions, 10 cm × 10 cm× 10 cm (Multimatic Technical Centre, Markham, ON) and surrounded with 0.066 mm thick copper tape to shield the components

from RF emitted from the MRI. Based on shielding calculations, the copper should attenuate frequencies at 128 MHz by 184 dB. Attenuation levels greater than 100 dB are considered impenetrable (See Appendix B for shielding calculations).

The CZT modules were tiled in a 2×2 arrangement for a total of 1024 pixels (32×32 array) and affixed to a separate custom power distribution circuit board. The signals were routed via aluminum shielded flat flexible cables (FFCs) to the DRB as shown in Fig. 3.2. An aluminum heat sink plate was attached to module heat sink on the back side of the modules to provide additional heat dissipation (aluminum heat sink and power distribution board not shown in the figure). Table 3.1 summarizes the front end gamma camera properties.

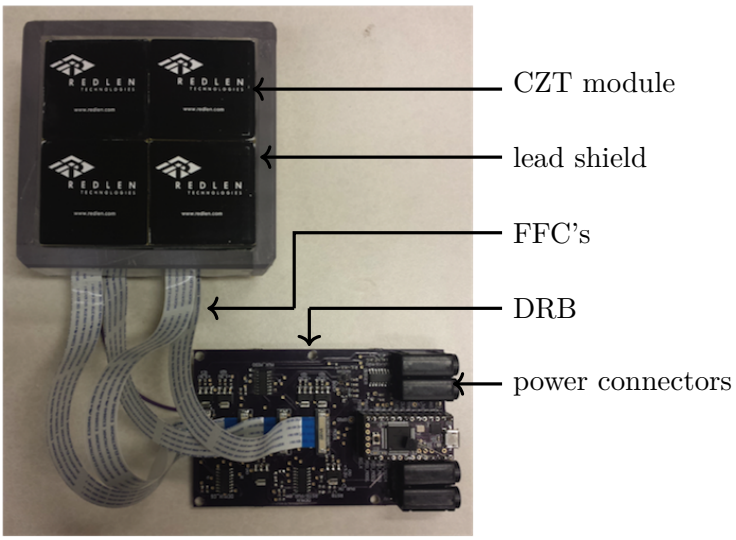

Figure 3.2: 2x2 array of Redlen CZT modules with a custom readout circuit board (Module layout - clockwise from top left: Module 1-4).

The proposed MBI system is comprised of Redlen's 256-pixel CZT detector modules (Redlen Technologies, Saanichton, BC). Each module is composed of a 2×2 array of bulk CZT with 64 pixels (8×8 array - 2.46 mm pixel pitch) and are bonded to a common cathode plate [120]. Spatial localization of electron-hole pairs generated from the absorbed gamma rays are guided by the electric field from the anode and cathode geometry as shown in Fig. 3.3. The module components feature an on-board application-specific integrated chip (ASIC) with a charge sensitive analog front end in the charge collection circuitry to process the induced charge on the CZT electrodes. Signals which exceed a user defined voltage threshold (module default= 70 keV) are subsequently processed by an analog to digital converter (ADC) and the pixel and

Table 3.1: Physical gamma camera properties

Detector Properties	**Collimator Properties**
Material: CZT	Material: Lead
Thickness: 5 mm	Thickness: 2.54 cm
Pixel size: 2.2 mm	Hole inradius: 0.55 mm
Pixel spacing: 2.46 mm	Hole shape: Hexagonal
Module array: 4× 4	**Additional Properties**
Total number of pixels: 1024 (32×32)	Shielding material: Lead
Field of view (FOV): ∼ 8 cm × 8 cm	Shielding thickness: 7 mm
Camera dimensions (Exterior): 10 cm × 10 cm ×10 cm	Heat sink material: Aluminum

energy information from valid events are stored in a 256-event First in First Out (FIFO) buffer on a field programmable gate array (FPGA). Charge collection parameters such as the charge collection peaking time and discharge time, and individual pixel threshold can be defined by the user. However, all of these parameters were maintained at default levels. The peaking and discharging time of the charge collection circuitry can be selected from pre-defined times between 206 ns and 990 ns (default = 990 ns) and between 2.5 µs and 86.9 µs (default=75.6 µs. The global default threshold is 70 keV, but each individual pixel can be fine tuned to a slightly different threshold. The module configuration (further details in the software development section) including charge collection and pixel specific parameters are stored in registers on an internal EEPROM.

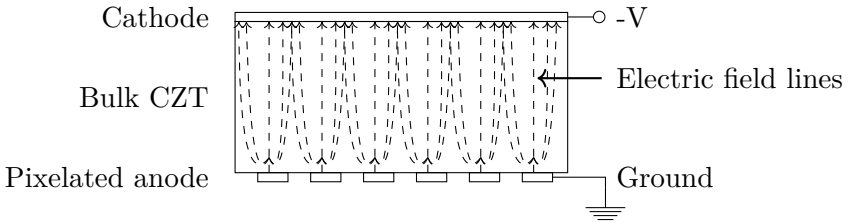

Figure 3.3: Cross section of pixelated CZT.

Communication with the CZT modules was facilitated with a Universal Serial Bus (USB)-based microcontroller development board (Teensy 3.1) featuring a 32-bit ARM Cortex-M4 microcontroller housed on the DRB board and interfaced to a host computer. The module communicates via a serial peripheral interface (SPI) bus using low voltage differential signaling (LVDS) with a maximum clock rate of 24 MHz.

The hardware schematic outlining the connections for one module in the DRB is shown in Fig. 3.4. All dashed lines indicate a common connection to all four modules. The bulk CZT was biased at -450 V and voltage regulators (STMicroelectronics LD1117) were used to drop a 6 V input supply voltage to 1.2 V, 2.5 V, 3.3 V (digital), and 3.3 V and 5 V (analog) to power the analog and digital components on the modules and the integrated circuits on the DRB (voltage regulators not shown in Fig. 3.4). Separate analog and digital ground planes were designed on the power distribution circuit board and combined on the DRB to reduce ground loops and cross talk. At 3 T, the wavelength from RF excitation in tissue is ~ 26 cm [121], therefore cable lengths in multiples of 26 cm were avoided to prevent interference of the RF signal with the power and data lines. The high voltage and low voltage power cables were approximately 12 m in length. A USB extension cord (length = 500 cm) was required to extend the micro-USB to USB cable (185 cm) from the gamma camera to the MRI control room. Low pass filters (Mini-circuits - BLP-30+) were connected to the low and high voltage power lines. (This particular filter reports an attenuation of 76.9 ± 2.8 dB at 127 MHz [122], where 60 dB corresponds to an attenuation ratio of 1×10^6). Ferrite chokes were placed on all cables to further minimize RF interference. See Appendix A for the complete electronic schematic for one module (Fig. A.1), including the circuit board layout (Fig. A.2) and power distribution board layout (Fig. A.3).

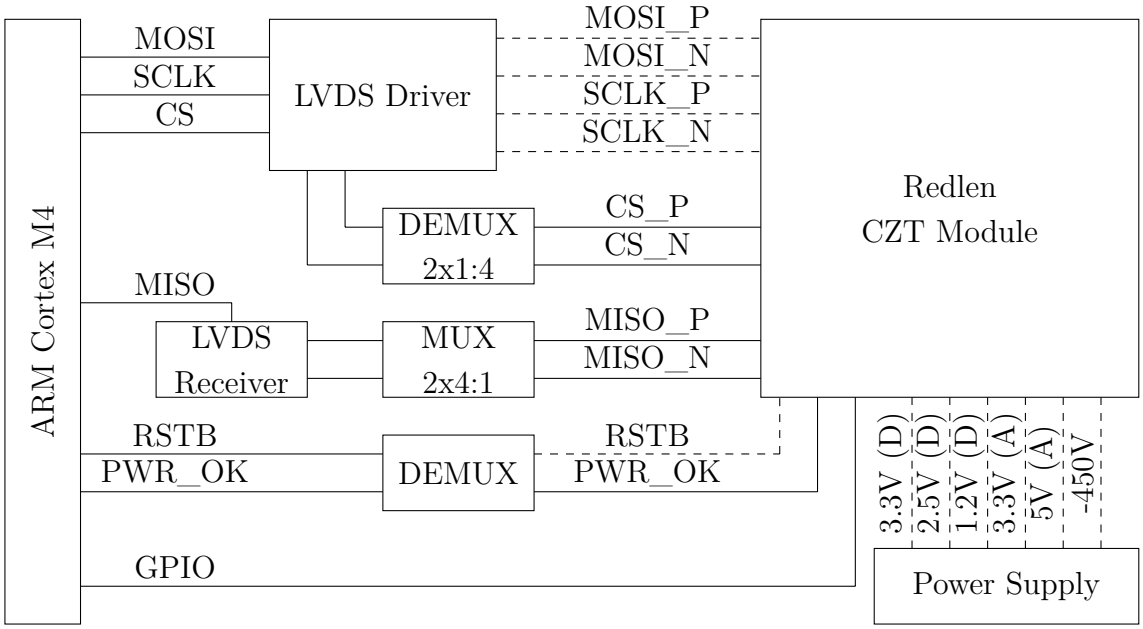

Figure 3.4: Hardware schematic for a single CZT module.

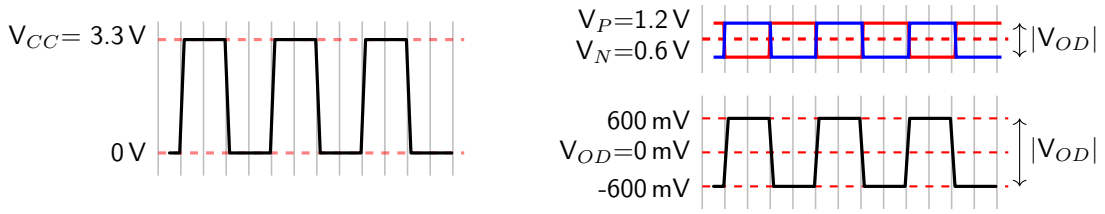

(a) Singled ended SPI (b) Differential LVDS SPI

Figure 3.5: Comparison between single ended SPI and LVDS.

The standard SPI protocol consists of four full-duplex signal lines: 'master in slave out - MISO', 'master out slave in - MOSI', 'clock - SCLK', and 'chip select - CS', with the modules serving as the slave. The LVDS signaling uses two complementary signals which convey the same information as a single-ended signal but is less susceptible to noise and allows for faster communication and lower power consumption. LVDS is advantageous for high speed communication because of a lower voltage swing and inherent noise cancellation with the two differential signal lines. In single-ended SPI, the signal swings through the full 3.3 V when switching logic levels (Fig. 3.5a), whereas in differential signaling, the maximum voltage swing required to switch logic levels is only 600 mV (Fig. 3.5b). In differential signaling, there are two signal lines, one is non-inverting and the other inverting. The non-inverting signal line (denoted by V_P) is logic high at 1.2 V and the inverting signal line (denoted by V_N) is logic low at 0.6 V. The differential voltage required to switch logic levels is the difference between the signal lines as shown in Fig. 3.5b and any noise on the SPI signal appears on both differential lines and is cancelled out.

However, the device controller uses the standard single-ended SPI protocol, so the single-ended master SPI signals (CS, MOSI, and SCLK) from the microcontroller must be converted to LVDS using an LVDS driver (Texas Instruments SN65MLVD047). In return, the MISO signal must be converted from LVDS to a single-ended SPI signal through an LVDS receiver (Texas Instruments SN65LVDS2).

A separate input/output pin was designated the CS pin because the standard SPI protocol deasserted the CS before the full 24-bit frame was transmitted. Bi-directional multiplexers (mux and demux) (Texas Instruments SN54LV4052A) located on the digital readout board were used to drive the CS signal (demuxed) to the selected module and to receive the MISO signal (muxed) from the selected module.

Each CZT module has an RSTB, PWR_OK and GPIO pin. The RSTB pin controls

the software reset on the module and the PWR_OK pin is asserted when the modules are powered up. The GPIO pin is designated as a general purpose input/output pin and is asserted when there are events in the FIFO. The PWR_OK pins from each module are regulated with a bi-directional mux and are demuxed based on the selected module. A separate GPIO pin is monitored for each module to determine which detector module FIFO contains event data to be read by the host computer.

3.2 Software Development

The 32-bit ARM Cortex-M4 microcontroller on the Teensy 3.1 board was programmed using the Arduino 1.0.5 integrated development environment (IDE) and Teensyduino. Teensyduino is a software add-on, for programming compatibility of the Teensy with the Arduino IDE. The main microcontroller code was written using an optimized SPI library [123] which was modified to conform to the protocol specific to the modules. The microcontroller has a maximum clock speed of 96 MHz, but the SPI speed is limited to 24 MHz and matches the maximum communication speed of the CZT modules. The modules were programmed in SPI mode 1 (clock polarity = 0, clock phase = 1), where the MISO is updated on the rising edge and sampled on the falling edge of the clock pulse. However, the CZT modules do not conform to standard SPI protocol. In order for the MISO and MOSI data to align to the same clock edge, the MISO is triggered on the rising edge of an internal clock immediately following the assertion of the chip select line. This allows the first MISO bit to be sampled at the same time as the MOSI bit. However, there is an inherent delay (approximately 21 ns) before the module sees the rising edge of the internal clock, resulting in the MISO updating on the falling edge of the master clock instead of the rising edge. This delay can be seen on the MISO line in Fig. 3.6. A D-type (delay) flip flop (Texas Instruments SN74LVC1G80) was used to introduce a delay so that the MISO would update on the rising clock edge (MISO* in Fig. 3.6), and therefore, the data could be sampled accurately in SPI mode 1.

The module is selected based on the state of the multiplexers. Instructions from the microcontroller are sent to the slave (CZT module) via the MOSI line by asserting the CS line for the corresponding module. Data from the selected module is returned on the MISO line.

The communication protocol consists of sending and receiving 24-bit frames. In-

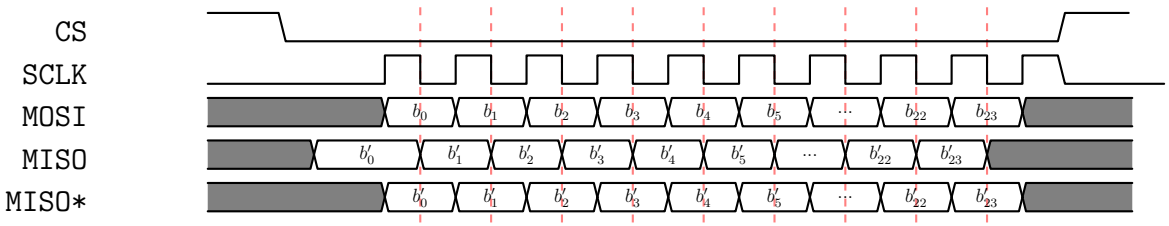

Figure 3.6: CZT Module SPI timing - SPI mode 1.

formation stored on the module can be accessed through either the Module Register Access (MRA) or the Event Data Readout (EDR) mode. The MRA mode allows access to the module configuration and control register settings, and the EDR mode allows access to energy and pixel information from the events detected on the module. When in EDR mode, MRA mode is still accessible and is given priority over EDR mode.

The bit assignments of the MOSI SPI frame in MRA mode are shown in Fig. 3.7. Reading or writing to the module is indicated by the most significant bit (MSB), 'b23', '1' to read and '0' to write. The least significant bit (LSB), 'b0' is designated the even parity bit. Writing to a register requires setting 'b23:b20' to '0'. The second bit is designated the address pointer store (APS) and is reserved for reading from a register. This bit is written low for write commands. The next two bits are reserved and must be held low. The following 19 bits are reserved for the register address (11 bits) and the data (8 bits) belonging to the register. No data is returned on the MISO line when writing to a register.

Figure 3.7: MOSI frame in MRA/EDR mode.

b23	b22	b21	b20	b19	b18	b17	b16	b15	b14	b13	b12	b11	b10	b9	b8	b7	b6	b5	b4	b3	b2	b1	b0
R/W	APS	R	R	A10	A9	A8	A7	A6	A5	A4	A3	A2	A1	A0	D7	D6	D5	D4	D3	D2	D1	D0	PTY

Reading in MRA mode requires two SPI frames. The first frame is used to store the desired address register to the module's address pointer. The first four MSBs are set to '0100', the first to indicate a write operation, the second to set the address pointer store bit, and the next two bits are reserved and held low. The address register is assigned to bits 'b19:b9' and data bits 'b8:b1' are ignored. No data is returned on the MISO line. The second MOSI frame is designated a read command. The MSB and the LSB are set to '1' to indicate a read operation and to set the even parity bit. All remaining bits are kept low. The data register is then returned on the MISO line

in the format shown in Fig. 3.8. The first bit is the busy 'BSY' bit and remains high until the module is ready for the data to be output. If the 'BSY' bit is high, the 'CS' should be deasserted, and reasserted after some delay. The full MISO frame will be read when the 'BSY' bit is low. The second bit indicates if there was an error detected such as a parity error, a FIFO overrun/underrun, or power/voltage levels exceeding predefined thresholds. The error must be cleared in the module status register before attempting to read from the module. The following twelve bits are unused and defaults to '0', the register data is returned on bits 'b8:b1' and the parity bit 'b0' completes the SPI frame.

Figure 3.8: MISO frame in MRA mode.

b23	b22	b21	b20	b19	b18	b17	b16	b15	b14	b13	b12	b11	b10	b9	b8	b7	b6	b5	b4	b3	b2	b1	b0
BSY	ERR	EV	0	0	0	0	0	0	0	0	0	0	0	0	D7	D6	D5	D4	D3	D2	D1	D0	PTY

Figure 3.9: MISO frame in EDR mode.

b23	b22	b21	b20	b19	b18	b17	b16	b15	b14	b13	b12	b11	b10	b9	b8	b7	b6	b5	b4	b3	b2	b1	b0
BSY	ERR	EV	P7	P6	P5	P4	P3	P2	P1	P0	E11	E10	E9	E8	E7	E6	E5	E4	E3	E2	E1	E0	PTY

EDR mode is set by writing to a designated bit in the module status register. This speeds up event readout throughput by requiring only one SPI frame (instead of the standard two frames to read in MRA mode). The MOSI frame in EDR mode is exactly the same as the second MOSI frame when reading in MRA mode - the MSB set to '1' indicating a read operation and the LSB set to '1' for the even parity. The MISO format is similar to MRA mode in that the first three MSBs are the same as shown in Fig. 3.9. Event data is returned on the next twenty bits - 'b20:b13' and corresponds to the pixel (0-255) in which the event was detected, followed by 'b12:b1' indicating the corresponding ADC energy (0 to $(2^{12} - 1)$). However, the dynamic range of energy detection is between 0 and 1365. To exit EDR mode, an MRA mode write frame is sent to the module status register to clear the EDR mode.

The flowchart in Fig. 3.10 outlines the microcontroller code written to communicate with four CZT modules. Upon power-up, all modules were reset by asserting and then deasserting the RSTB pin. Once the PWR_OK pin is asserted, access to MRA or EDR mode is permitted. One of three module options are available to the user: write to a register in MRA mode, read from a register in MRA mode or acquire data in EDR mode.

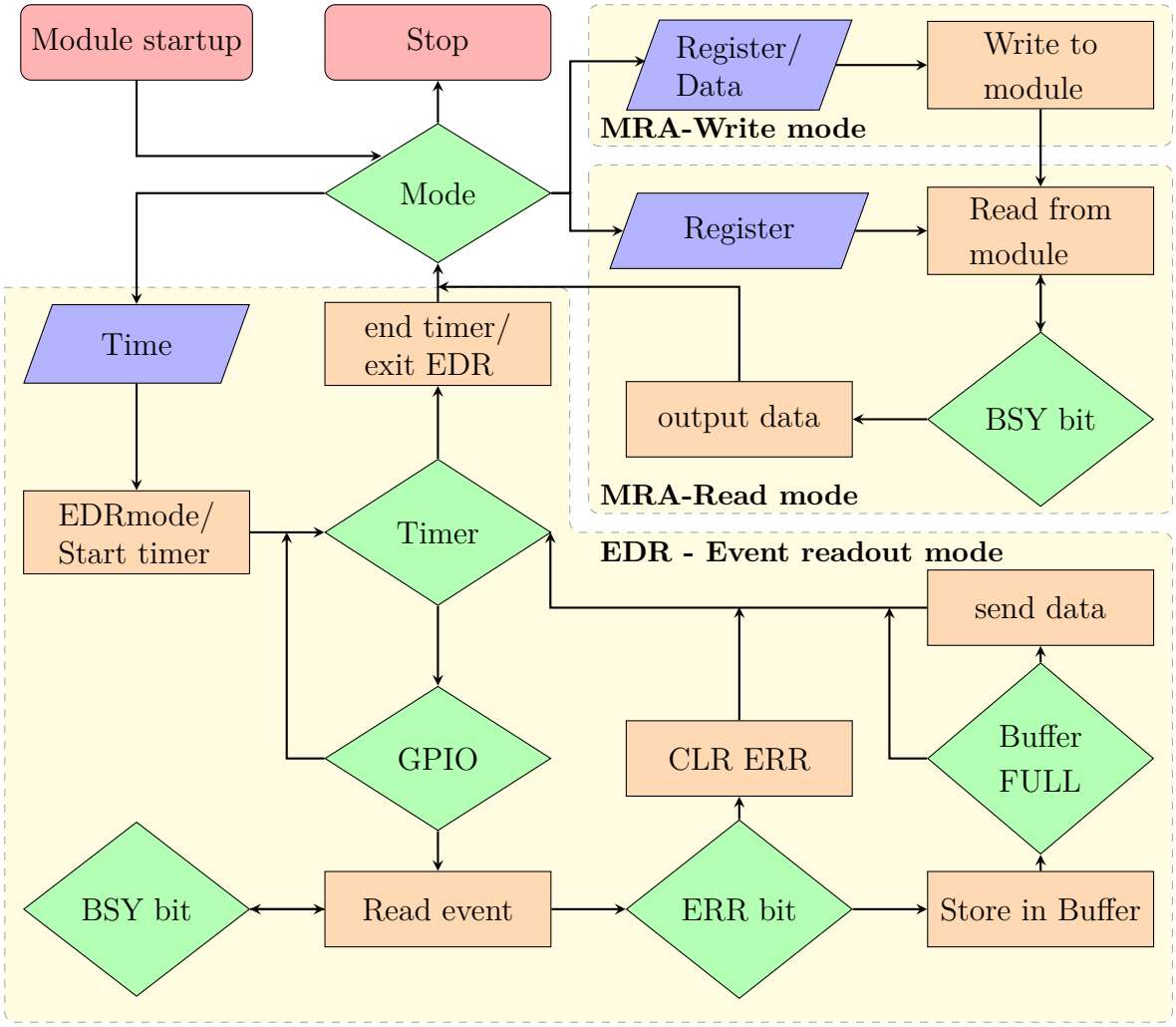

Figure 3.10: Gamma camera software flow chart.

In MRA write mode, the user inputs the selected module(s), the register and register data to be written. A write command is sent from the host computer to the microcontroller and the microcontroller will execute the write frame on the selected modules. A read command is followed by the write frame to ensure that the register data was written correctly. When reading a register frame, the MSB bit ('BSY') must be polled to ensure that the module is ready to send the data belonging to the register. If it is high, the CS is deasserted and reasserted after a short delay. The register data bits are read when the MSB is low and is returned to the host computer to confirm that the correct data was written to the appropriate register. After writing to the desired registers, the module configuration setting can be saved to the internal FLASH

by writing to the store configuration bit in the FLASH control register. The saved configuration can be restored at any time by writing to the restore configuration bit in the same register.

Reading from a register in MRA mode requires a user input of the selected module(s) and the input register. Selected registers which required readout from secondary or tertiary registers were programmed into the microcontroller code. For example, reading the temperature of the module requires reading two registers, therefore, a read command for the second temperature register is issued upon reading the first temperature register.

The third option in the script is to acquire data in EDR mode. To enter the acquisition mode, the user must input the desired acquisition time. A series of write commands are issued to clear the FIFO and reset the charge collection device (CCD) on the module. The CCD includes all the circuity required to process the charge collected from the CZT detector. Finally, the module control register to set into EDR mode. Once in EDR mode, the timer on the microcontroller begins and the master controller polls the GPIO pin of each module to check if there are events available to be read from the FIFO (the default configuration sets the GPIO logic high when there is at least one event in the FIFO). If the GPIO is logic high, the corresponding module is selected by setting the multiplexer. Events will be read continuously from the corresponding module, until either the FIFO is empty or the designated acquisition time is met. When the GPIO pin of the current module switches to logic low, the master controller will subsequently check the GPIO status of the next module. The GPIO pin is polled in a round robin order to ensure all modules are read from equally. The events are stored within a 1024 event frame buffer on the microcontroller and once full are transferred to the host computer via USB. Events will only be read from modules with an asserted GPIO pin. A condition is set to clear any errors that may have set during EDR mode if all GPIO pins are low for a designated period of time. The remaining events that are stored in the buffer are transferred to the host computer upon termination of the timer. EDR is cleared in addition to clearing the FIFO and resetting the CCD.

When reading an event frame, the first bit indicates whether or not the module is ready to send an event. If the module is not ready, the MSB, 'b23' will be set high. If 'b23' is high, the CS is deasserted and after a short pause (42 ns 3 clock cycles at 72 MHz), the CS is reasserted and the first bit will be checked again. If it remains busy

after 3 attempts, the script will skip the current module and check the next module. The second bit is an error bit and is set high if one of several errors occur. The internal FIFO on the module holds 256 events and if events are filled faster than the events are read out, a FIFO overrun error will occur. If there are no events to be read and a read command is issued, a FIFO underrun error will occur. Other possible sources of error occur when the temperature or voltage reading exceeds the predetermined threshold or if there is a parity error on the host SPI bus or charge collection device. If the error bit in the data frame is set, the remaining data bits in the MISO will be discarded and the error must be cleared in the the module status register before continuing to read events. The third bit indicates whether the returned data is an event ('b21' = 1) or data from a register ('b21' = 0). Each event must satisfy the three MSBs - '001' in the 24-bit frame in order for it to count as an event.

Events are stored on the microcontroller in batches of 1024 events. The computer sends a signal to request data. In return, the microcontroller sends a return signal when it is ready to send data. The current batch size along with the data is then sent. An end of data check bit is sent to indicate if there are more events to be read or if it is the final data batch. If the timer is still active, this end of data bit is set to 0 indicating there are more batches to be read. After the timer ends, the last batch is sent with the end of data check set to signify the last batch to be read. A command to exit EDR mode is issued and the module returns to an idle state in which the user can then access any mode on the modules.

MATLAB graphical user interfaces (GUIs) were created to simplify the data readout and module interfacing between the user and the microcontroller (Fig. 3.11a). The main interface (Fig. 3.11a) integrates the C program written exclusively to optimize speed for data processing in EDR mode. As a result, the GUI updates only when the buffer is full. Therefore, at low count rates, there is a significant delay from the time of detection to visualization on the GUI. At higher count rates, the GUI provides near real-time imaging.

From the main interface, the user can enter MRA mode to read and modify the predefined module configuration and control registers such as the minimum threshold energy, selecting which pixels are enabled or disabled and a variety of other features (Fig. 3.11c-3.11d). The pixel enable GUI (Fig. 3.11b) allows the user to view which pixels are currently enabled and to toggle the status of any combination of pixels.

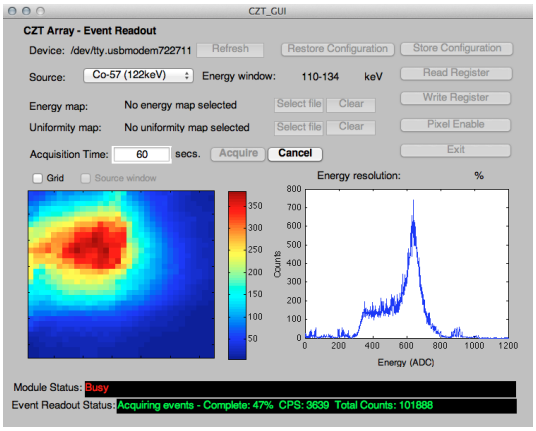

(a) Main GUI window

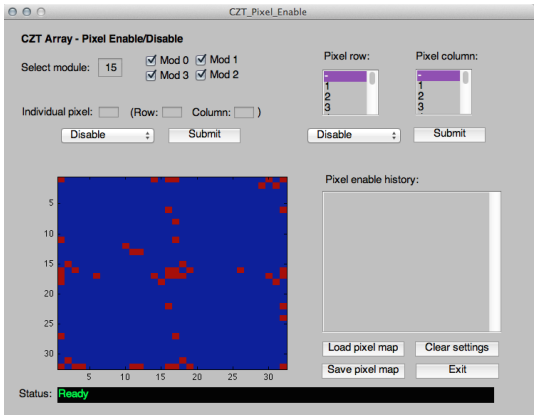

(b) Pixel enable GUI

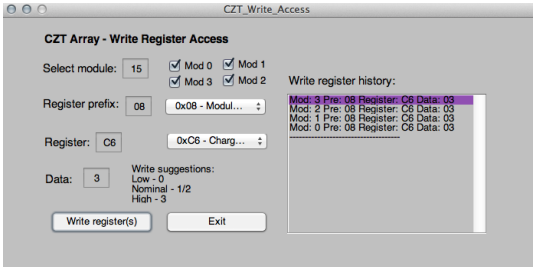

(c) Read-MRA mode GUI

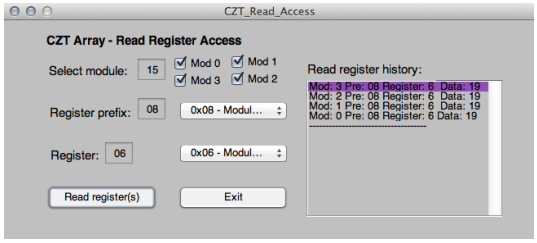

(d) Write-MRA mode GUI

Figure 3.11: MATLAB GUI to communicate between CZT modules and host computer.

3.3 Acquisition Configuration

To perform an acquisition, the modules must be configured prior to entering EDR mode. A set configuration was saved to the internal FLASH/EEPROM by saving the module configuration in the FLASH control register. Prior to each acquisition, the configuration was restored by writing to the restore configuration bit in the FLASH control register. The saved settings included adjustments in the power and individual pixel settings.

The default power setting was initially set to 'nominal' but was subsequently determined to require high power mode for accurate module communication. In the absence of a radioactive source, certain pixels were overactive and would trigger event detection. In addition, in the presence of a radioactive source, a number of pixels did not detect any events. These malfunctioning pixels were consistent from acquisition to acquisition and were therefore disabled through the pixel configuration register to maximize event throughput from active pixels. These defective pixels accounted for

approximately 6 % of all pixels. A 1dead' pixel map was created to identify a list of pixels which were disabled.

Other configuration settings relevant to the EDR mode are the event level threshold and the dynamic energy range setting. The low level threshold was kept at the module default value of 70 keV and any photons detected below this threshold were discarded. The module charge collection circuitry has two dynamic range settings, low (0-300 keV) and high (0-600 keV). The default and saved configuration collects data in the low energy range. Upon restoration of the module configuration, EDR was executed by requesting an acquisition time, and setting the EDR bit in the status register.

3.4 Post-data Correction factors

Event data from the modules is an ADC representation of the charge collected during the photon detection. Several correction factors were implemented on the ADC data in order to ensure accurate gamma camera assessment. An energy correction is required to calibrate the ADC channel to the corresponding gamma energy detected in each pixel since no two pixel responses are identical. A flood map of various radioactive sources spanning the dynamic range of the CZT pixels were used to determine the energy correction factor in the control environment (outside the MRI room). A minimum of 3×10^6 counts were acquired over the entire FOV using Co-57 (122 keV), Tc-99m (140 keV) and In-111 (171 keV and 245 keV).

The Gaussian function in Eq. 3.1 was fitted to the gamma peak of the ADC energy spectrum for each pixel and source where the width of the peak is given by σ, A is the amplitude of the peak and μ is the ADC channel of the energy peak. The dynamic range of the CZT module in the low energy range specified in the CZT module documentation was between 0 and 300 keV. However, the true dynamic range is dependent on each pixel and the 245 keV peak from In-111 was indistinguishable, and therefore, not used for the energy correction. A least squares fit was applied to the peak ADC channel and the corresponding energy peaks for the three sources. Fig. 3.12 shows an example of the correction factor mapping the detected ADC channel to the true energy (in keV) for one pixel. The R^2 was 0.996 indicating the module response was linear over the range of interest. Due to restrictions limiting the use of radioactive materials in the MRI room, all energy correction factors were performed with only Tc-99m. The procedure for determining the energy correction factor was a single

energy peak was similar to the multiple energy peak in that a Gaussian function must be applied to the spectrum of each pixel from a uniform flood source to determine the peak ADC channel corresponding to the 140 keV peak. The calibration factor using the single energy peak is given by 140 keV divided by the peak ADC channel for each pixel. The energy correction for all detected events with each pixel was determined by scaling the ADC channel to the calibration factor as shown in Eqn. 3.2 assuming linear extrapolation through the origin. No prior assumptions can be made about the y-intercept for each pixel because of the unknown effect from the MRI environment.

$$f(x) = Ae^{-(x-\mu)^2/\sigma^2} \tag{3.1}$$

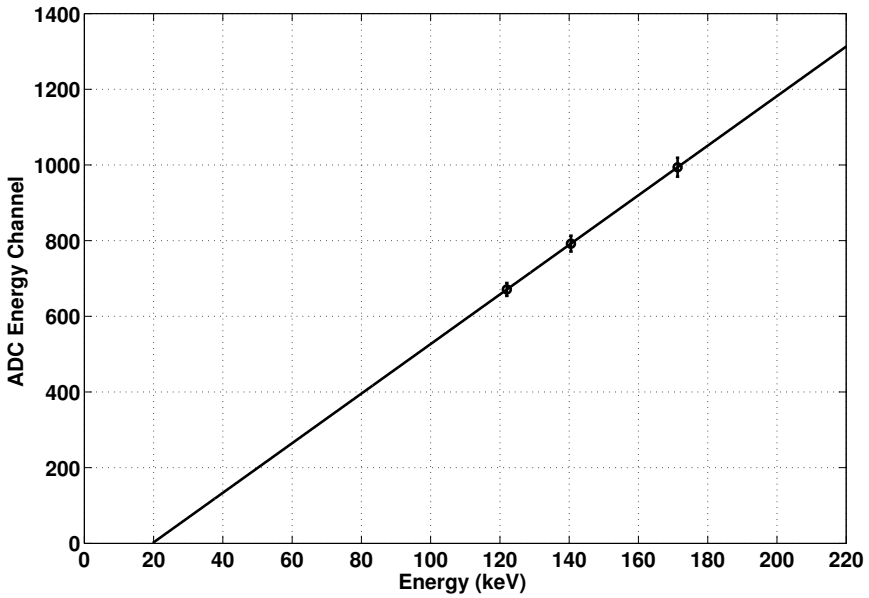

Figure 3.12: Linear regression of the energy correction plot for pixel 150 (row 22, column 5 in the 32×32 detector array): $y = 6.55x - 128.48$, $R^2 = 0.996$.

$$E_{corrected}(keV) = E_{ADC}\frac{140\,keV}{E_{ADC}(140\,keV)} \tag{3.2}$$

In addition to energy correction, a uniformity correction is essential for accurate imaging. A uniform flood source should result in a uniform number of counts detected in each pixel; this goal, however, is not achieved due to the variable response of each pixel. This response is generally energy dependent and a uniformity map over

a range of energies would be required. However, since all experiments in the MRI were performed with Tc-99m, the uniformity maps were calibrated to 140 keV. This correction map was generated by normalizing the total number of counts across all pixels in the FOV, to the mean number of counts across the full FOV. The uniformity corrected number of counts in each pixel is given by Eq. 3.3.

$$FOV(i,j)' = \frac{FOV(i,j)}{max(FOV)} \frac{1}{(x_{max} + y_{max})} \sum_{i=1}^{x_{max}} \sum_{j=1}^{y_{max}} FOV(i,j) \tag{3.3}$$

All disabled pixels were interpolated by averaging the nearest neighbouring pixels. A 3×3 array is centred around pixels to be interpolated. Disabled pixels within the 3×3 boundary are ignored and pixels around the perimeter of the detector are interpolated using only pixels which fall within the 3×3 boundary. Clustered disabled pixels, which have no valid pixels within the boundary, were interpolated after all other pixels were interpolated. All correction factors were applied post acquisition.

Chapter 4

Evaluation of the Gamma Camera and MRI Performance

This chapter is divided into five parts and evaluates planar scintigraphic imaging and MR imaging with the gamma camera developed from Chapter 3: i) The first section presents the methods and imaging results from gamma imaging chronologically, as the results from the prior sections affected the subsequent experimental methods. The gamma camera performance was addressed in four different imaging conditions - in a control environment (outside the MRI room), inside the MRI bore (B_0 field only) and during simultaneous MRI imaging with two common MRI sequences. All gamma camera measurements were performed with a parallel hole collimator in place and all tests involving MRI were performed in a GE Discovery MR750 3.0 T (General Electric Healthcare, Milwaukee, WI). ii) The next section presents the effects of the gamma camera on MRI performance and from this point forward, all remaining experiments were performed with a 16-channel receive breast array coil (Sentinelle by Invivo, Gainesville, Florida) for dedicated breast imaging. MRI performance was compared without the gamma camera, with the gamma camera idle (powered but not operating) and during simultaneous imaging. iii) The results from simultaneous imaging with MRI and scintigraphy were presented. v) Finally, the last section will discuss and summarize the findings from both imaging modalities.

4.1 Effect of MRI on Gamma Camera Performance

4.1.1 Experimental setup

Evaluation of the gamma camera performance inside the MRI scanner is essential to determine if there are any effects influenced by MRI system. These experiments require the use of radioactive materials in the MRI room. Due to the controlled nature of radioisotope handling and the absence of ionizing radiation in MR imaging, permission was required for radioisotope use in the MRI scanner. An internal permit was obtained for up to 925 MBq of Tc-99m for experiments related to this project. Tc-99m was ordered and received by the nuclear medicine department at St. Joseph's Healthcare Hamilton and transported to the PET/CT hot lab located next to the MRI controlled area. Experiments were performed in the MRI scanner room located in the Imaging Research Centre (within St. Joseph's Healthcare Hamilton). Since Tc-99m is not normally used in the PET/CT area, a separate area in the hot lab was designated for

waste and phantom storage. Radioisotope handling for phantom preparation was done in the PET/CT hot lab. The MRI room was temporarily designated a basic nuclear lab and appropriate signage (radiation warning sign and the internal permit) was posted for the duration of the experiment. Decommissioning of the MRI scanner was performed after each experiment with swipe samples from the MRI room, immediate area outside the MRI room, MRI control room and PET/CT hot lab to clear the site for normal use.

The characteristics used to determine the performance of the gamma camera include the energy resolution, uniformity, spatial resolution, and geometric accuracy. The energy resolution and uniformity was measured with a plastic phantom measuring (10 cm ×10 cm × 1 cm) filled with 150 MBq of Tc-99m in water. Both spatial resolution and geometric accuracy were measured using capillary tubes with inner diameter = 1 mm and length = 7.5 cm. A single capillary tube filled with 12 MBq of Tc-99m was used to characterize the spatial resolution. A second capillary tube filled with 10 MBq of Tc-99m was used with the first capillary tube to measure the geometric accuracy (The discrepancy in the absolute activity in the two line sources was due to the introduction of a small air bubble preventing additional Tc-99m from filling a portion of the capillary tube). The two capillary tubes were positioned parallel, 4 cm apart. Gamma imaging was performed with this geometry in both the x- and y-direction.

Scintigraphic imaging was performed in four conditions: in a control environment, inside the MRI bore with the static B_0 field and during simultaneous imaging with two common MRI sequences. The gamma camera was located well beyond the 5 Gauss line outside the MRI scanner room for the control condition.

Dedicated receive-only breast coils are used for breast MR imaging, but they were not used in measuring the gamma camera performance. This was in part due to the passive nature of the breast coil, but principally because the shape and size of the breast coils hindered the ability to perform the gamma camera performance measurements. Due to space constraints, the gamma camera configuration was limited to a location perpendicular to the breast coils as shown in Fig. 4.1 for the MR imaging experiments. In this configuration, a clinical system would be able to image both breasts simultaneously without spillover from the other breast, however, it is acknowledged that the standard breast MR imaging sequence would optimally acquire images in orthogonal planes to the MBI images.

To facilitate gamma camera performance measurements in conditions as close as possible to the breast MRI configuration, the gamma camera was positioned relative to the isocenter as if the breast coils were present. This was approximately 16 cm from the center of a breast-like phantom in the z-direction and 7 cm from the center of the bore in the x-direction, with the detector facing into the bore in the z-direction as depicted in Fig. 4.1. In the diagram, the breast coil frame was removed in order to visualize the placement of the gamma camera relative to the coils. The power cables (not shown in figure) extended down the center of the bed to the perimeter of the room to the DC power supplies located outside the 5 Gauss line. The USB data cable was directed through a penetration panel to the host computer located in the control room.

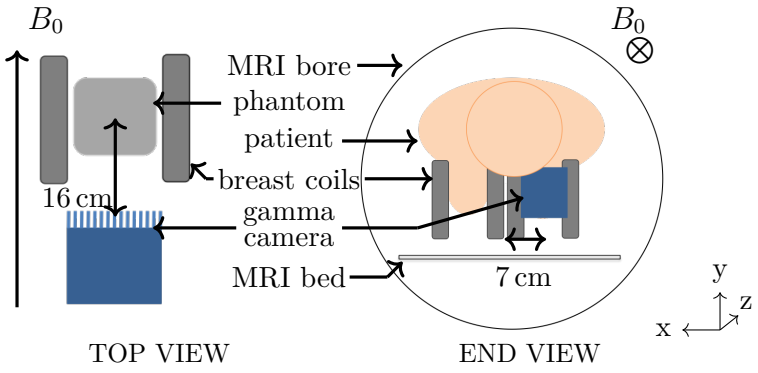

Figure 4.1: Configuration of the gamma camera in the MRI bore - Top view (left) and end view (right) of gamma camera set-up (one set of coils shown).

If a patient were being imaged, the patient would be positioned prone, feet first into the bore with the breasts pendant between each set of breast coils. Imaging was performed with the gamma camera inside the bore with only the static main magnetic field (B_0) field and with two common breast MRI sequences, gradient echo (GRE) and spoiled gradient echo (SPGR). The parameters of each MRI sequence are listed in Table 4.1 below.

Table 4.1: MRI sequence parameters

	TR (ms)	TE (ms)	Flip angle-α	slice (mm)	# slice	space (mm)	FOV (cm)	matrix
GRE	500	10	45°	3	17	1.5	12	256
SPGR	50	8	45°	3	17	1.5	12	256

Preliminary tests indicated that certain pixels in the gamma camera were either over-active or inactive in EDR mode, and were therefore disabled prior to any further acquisitions. This initial set of pixels were disabled for all imaging conditions. Additional pixels were seen to become overactive depending on the MRI sequence used, and therefore, prior to any imaging, a background count for each sequence was acquired and pixels exceeding the background count rate were disabled for subsequent acquisitions for the corresponding sequence.

An acquisition was performed for two minutes in each imaging condition in the absence of any radioactive sources and repeated three times to ascertain the defective pixels. The average background count rate was 20 counts per second (cps). The background count rate increased up to 100 kcps when defective pixels were not disabled. A total of 60 pixels (5.9 % of all pixels) were disabled on the gamma camera for all imaging conditions due to over-activity or non-responsiveness. These pixels were saved to the module configuration as the default pixels to be disabled. During simultaneous acquisition, an additional 180 and 169 pixels were disabled during the GRE and SPGR sequence respectively and the average background count rate increased to 100 cps and 200 cps respectively indicating that some pixels exhibited variable behaviour in the presence of RF during MR acquisition sequences.

Prior to each gamma camera acquisition, the saved module configuration was restored to establish the appropriate module settings and default pixel settings. In addition to the disabled pixels in the saved module configuration, sequence specific pixels were disabled through the pixel register settings in the module MRA mode.

4.1.2 Energy resolution

The energy resolution of the system is the ability to discern two photons of different energies. For example, a system with 10 % energy resolution at 140 keV can not differentiate photons with energy between 133 keV and 147 keV. Energy resolution is important for dual-isotope imaging, but is also important for reduction of scatter contribution in the photopeak window.

A planar phantom was positioned at the collimator face and imaged for 10 minutes to obtain a flood map over the entire camera FOV. The acquisition resulted in a total of 6×10^6 counts. The energy calibration factors to scale each pixel accordingly was generated from the flood map as described in the previous section. Three additional acquisitions were performed with the planar phantom for 5 minutes (3×10^6 counts)

to quantify the energy resolution using the corrections from the first acquisition. This was repeated for each imaging condition to optimize the energy correction map in the event pixel responses were dependent on the effects from the MRI.

The energy resolution is defined as the full width at half maximum (FWHM) divided by the energy peak as given by Eq. 4.1. The summed energy spectrum from all pixels after energy correction were fitted with a Gaussian function where the width of the peak σ, is related to the FWHM by a factor of 2.35.

$$Energy\ resolution(\%) = \frac{FWHM \times 100}{E} = \frac{\sigma \times 2.35 \times 100}{E} \tag{4.1}$$

The average energy resolution for each imaging condition is listed in Table 4.2 and the corresponding spectra are shown in Fig. 4.2. There was no change in the energy resolution from the control environment to the static B_0 field, but there was a marginal increase in the scatter portion of the spectrum during the MRI sequences. The geometry of the system remained the same for all imaging conditions inside the MRI, therefore the increased contribution at lower energy channels was presumably due to increased noise overcoming the internal low energy threshold of the CZT module. This correlates with the increased background count rate. The total number of counts in the photopeak window (126-154 keV) increased by up to 10 % with the GRE sequence which translated to less than 1 % degradation in energy resolution. The effect of this increase is negligible within the photopeak window, as evidenced by the good agreement in energy resolution under different imaging sequences.

Table 4.2: Energy resolution at 140 keV

	Control	B0 field	GRE	SPGR
Energy resolution (%)	7.1	7.1	7.8	7.3

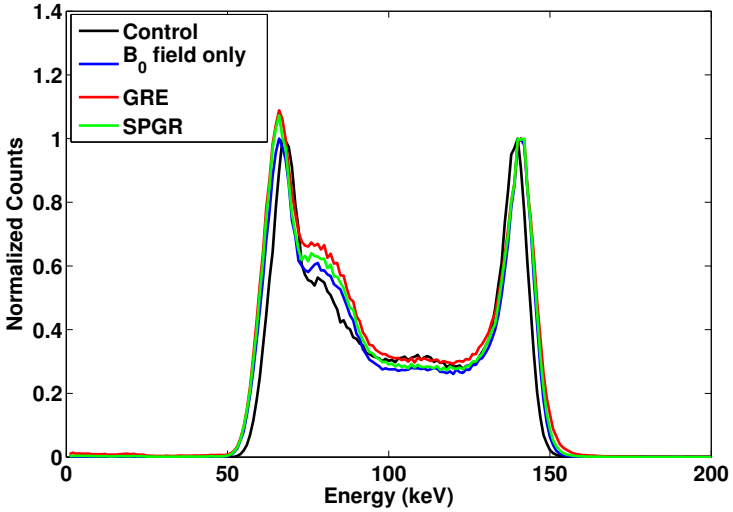

Figure 4.2: Energy spectrum of Tc-99m (A cut-off threshold of 70 keV was set on the ASIC of the CZT module).

4.1.3 Uniformity

The detector uniformity is an important indicator of the sensitivity of the pixels in the gamma camera where the uniform flood source should ideally result in the same number of counts in each pixel. Factoring in the fluctuations due to Poisson statistics, a minimum of 10 000 counts in each pixel would correspond to ±1 % variation in the detected counts. Each detector module and even each pixel has it's own unique set of characteristics from the charge collection efficiency and potential detector impurities. To correct for the individual pixel responses, the uniformity correction map was generated with a 20 % energy window centred at 140 keV from the same flood data set used for the energy correction factors. The uniformity was determined from the subsequent 5 minute acquisitions using the uniformity correction map. The defective pixels were interpolated by averaging the nearest neighbouring pixels after both energy and uniformity correction factors were applied.

Uniformity was quantified with two measurements, the integral uniformity (IU) and differential uniformity (DU) over several FOVs. The IU is the measurement of the maximum variation in the pixel response and the DU is the measurement of the greatest difference in counts within five contiguous pixels in any row or column denoted by k, both for a defined FOV with matrix size n×n (where n=32) given by Eq. 4.2 and 4.3 respectively. Uniformity measurements were calculated based on convolving the

flood map with a 9-point smoothing filter as outlined in the NEMA NU-1 protocol for pixels sizes less than 2.5 mm (where the Redlen CZT module pixel size is 2.2 mm) [124].

$$IU_{FOV} = \frac{max(FOV) - min(FOV)}{max(FOV) + min(FOV)} \tag{4.2}$$

$$DU_{FOV} = \frac{max\left\{FOV(k:k+4)\right\} - min\left\{FOV(k:k+4)\right\}}{max\left\{FOV(k:k+4)\right\} + min\left\{FOV(k:k+4)\right\}} \; ; \; 0 < k < (n-5) \tag{4.3}$$

The IU and DU were reported over the useful field of view (UFOV), central field of view (CFOV) and for each individual module in Tables 4.3-4.4. The UFOV was defined as the inner 30×30 pixels in the 32×32 array of total pixels (Fig. 4.3a) since the majority of disabled pixels were seen to be situated along the outer perimeter of the gamma camera. The CFOV was defined as the inner 26×26 pixels (Fig. 4.3b) encompassing 75 % of the central area of the detector array, as described by NEMA NU 1-2012 [124]. The individual modules are defined clockwise from the top left module as labelled in Fig. 4.3.

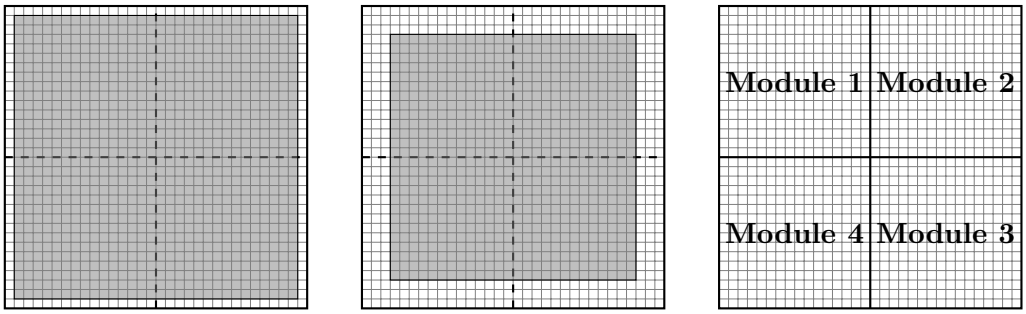

(a) UFOV (30×30 array) (b) CFOV (26×26 array) (c) Module assignment

Figure 4.3: Defined FOVs for uniformity measurements

Table 4.3: Uniformity of the gamma camera UFOV and CFOV

	IU (%)		DU (%)	
	UFOV	CFOV	UFOV	CFOV
Control	5.1	4.8	3.7	3.5
B_0 Field	6.9	6.9	4.2	4.2
GRE	7.9	7.9	5.7	5.7
SPGR	6.8	6.6	5.8	5.5

Both the integral and differential uniformity measured over the UFOV and CFOV increased when inside the MRI. The differential uniformity during the MRI sequences increased 150 % compared to the control condition, but did not vary between the UFOV and CFOV. It is evident that the MRI sequences affected the pixel responses, some severe enough that they must be disabled while others had some minor variation in the total number of counts detected, leading to increased non-uniformities.

Table 4.4: Uniformity of each module.

	Module 1	Module 2	Module 3	Module 4
	IU (%)			
B_0 Field	6.3	5.5	5.7	5.5
GRE	7.2	6.4	5.3	5.5
SPGR	6.3	5.5	6.4	5.6
	DU (%)			
B0 Field	4.8	4.3	4.6	4.3
GRE	5.6	4.8	3.8	4.3
SPGR	5.8	4.3	4.4	4.1

The variation in the IU and DU was consistent across modules 2, 3 and 4. Module 1 consistently reported poorer uniformity inside the MRI in comparison to the other modules which contributed to the overall diminished uniformity. Fig. 4.4 shows an example of the raw flood map data with disabled pixels during a GRE sequence on the left, and with the flood map post correction on the right. Visually, it is apparent that one module in particular appears to be less sensitive than all other modules. Therefore, the non-uniformity associated with the UFOV and CFOV appears to be the result of the reduced sensitivity in the first module location.

Given the abundance of disabled pixels during an MRI sequence, the cluster fraction was reported to establish the extent of interpolation over the FOV. The cluster fraction is a term introduced by NEMA to quantify the distribution of defective pixels in a discrete detector system. If a region in the FOV contains a large number of defective pixels, the majority of those pixels will be interpolated based on the nearest valid pixels, potentially leading to a decrease in image quality. The cluster fraction is given by Eq. 4.4 where N is the number of disabled pixels and the w_j is the cluster weighting factor. If there is more than one defective pixel within a 5×5 region, w_j is equal to one, else it is equal to zero.

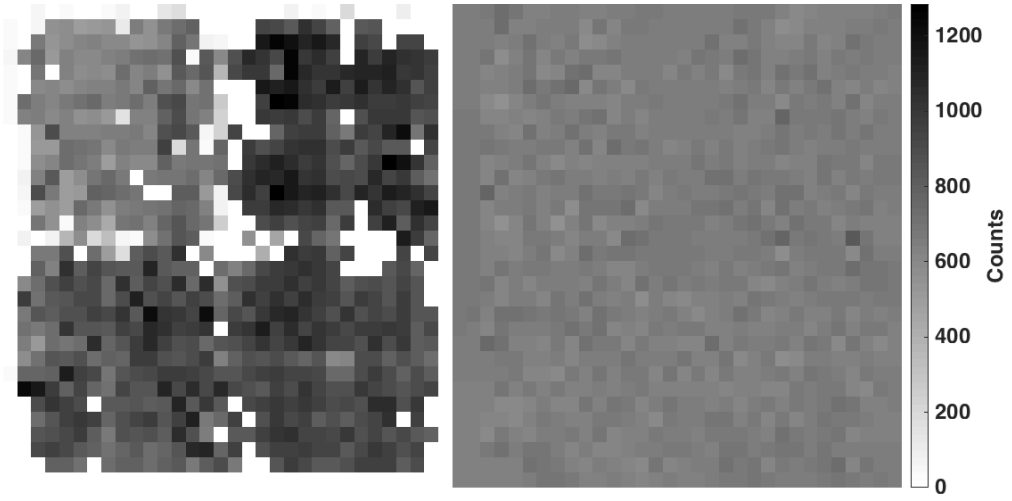

Figure 4.4: Raw flood map (Left) and uniformity corrected flood map (Right).

$$F_{Cluster} = \frac{1}{N_{DefPixel}} \times \sum_{j=1}^{N_{DefPixel}} w_j \tag{4.4}$$

The cluster fraction and the proportion of disabled pixels in the specified FOV is summarized in Table 4.5. Aside from the control and B_0 field condition, the cluster fraction ranged between 77 % and 98 % with approximately 3-13 % of pixels disabled in the UFOV and CFOV respectively. The high cluster fraction implies that the majority of disabled pixels were located within a 5×5 pixel region of another disabled pixel. Image quality may be degraded in these regions, in particular with small lesions and more likely near the module boundaries.

Table 4.5: Pixel cluster fraction

	UFOV		CFOV	
	$F_{cluster}$	% Disabled	$F_{cluster}$	% Disabled
Control/B_0	0.77	3	0.84	3
GRE	0.94	13	0.91	9
SPGR	0.97	12	0.98	9

4.1.4 Spatial resolution

The spatial resolution is defined by the smallest distance two line or point sources can be resolved and is reported in terms of the FHWM. The theoretical resolution of our

gamma camera is ∼2.7 mm, where the total spatial resolution is the quadrature sum of the collimator (mean diameter = 1.2 mm) and intrinsic resolution (2.46 mm). The spatial resolution of the gamma camera was measured with the capillary tube filled with 12 MBq of Tc-99m and imaged for 5 minutes at source to collimator distances of 0 cm, 4 cm, and 10 cm. Two sets of data were obtained with the line source positioned in both the x- and y- directions to take into account the asymmetrical property of the hexagonal collimator. The resulting line profile for photons between 126-154 keV for each row/column of pixels at each distance was then fitted with a Gaussian function and the FWHM determined for each source to collimator distance. The standard deviation in the FWHM determined the variation of the spatial resolution across the gamma camera field of view.

Table 4.6 summarizes the FWHM at various source to collimator distances. At the collimator face, the FWHM is in agreement with the expected resolution. The theoretical resolution based on the geometry of the collimator for a source to collimator distance of 4 cm and 10 cm, were 3.8 mm and 6.1 mm respectively. For a set distance, the measured FWHM remained the same (within experimental error) throughout each imaging protocol and correlated well with the theoretical system resolution. In the control and B_0 only condition, 10 cm from the collimator, the measured FWHM exceeds the expected FWHM by less than 0.5 mm. The increase was minimal and was likely due to a potential positioning error. Therefore, spatial resolution is unaffected by the application of the 3 T magnetic field, with and without an MR acquisition sequence.

Table 4.6: FWHM at various source to collimator distances.

	FWHM (mm)		
	0 cm	4 cm	10 cm
Control	2.8±0.4	4.1±0.5	7.2±0.7
B_0 Field	2.9±0.6	4.3±0.5	7.0±0.4
GRE	2.9±0.7	4.2±0.8	6.5±0.6
SPGR	3.0±0.7	4.3±0.7	6.9±0.9

4.1.5 Geometric accuracy

The purpose of addressing geometric accuracy in scintigraphy is to determine if the location of the source emission is accurate in relation to it's true position. Traditional

gamma cameras are prone to a geometric distortion artifact affecting the spatial linearity due to the positioning algorithm using multiple PMTs. Bar phantoms are typically used to address both geometric accuracy and spatial resolution. The spatial linearity would be characterized by the deviation from a straight line. However, CZT detectors do not exhibit the same artifact due to the method of direct photon detection. It was not expected that there would be any geometric distortions based on previous work testing CZT detectors in magnetic fields. However, it was still necessary to determine if the gamma camera system is able to accurately reproduce the location of the radioactive emissions.

Geometric accuracy of the gamma camera was measured using two capillary tubes, one filled with 10 MBq and the other with 12 MBq. They were affixed to a plastic board parallel to each other, 4 cm apart and imaged at the collimator face for 3 minutes. The sources were then rotated 90° and imaged for a further 3 minutes. A Gaussian function was fitted to each line source for each row/column in the image data shown in Fig. 4.5 and the distance between the peak positions were reported.

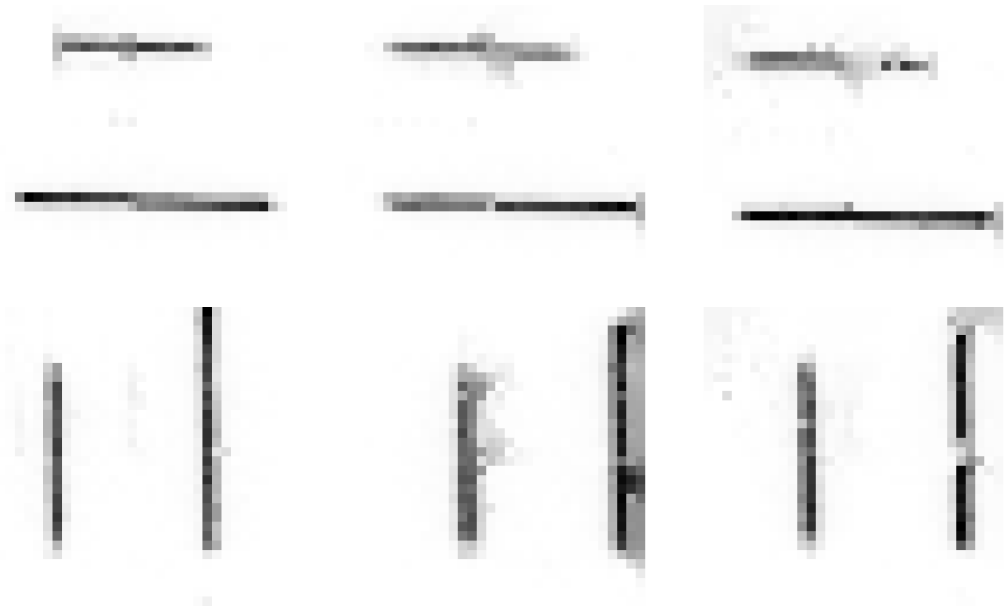

Figure 4.5: Projection image of two parallel lines sources. Top row: x-axis; Bottom row: y-axis (L to R: no sequence, GRE, SPGR).

The average distances measured between the two sources were 39.4±0.4 mm, 39.5±0.7 mm and 39.6±0.6 mm for the main magnetic field only, GRE, and SPGR sequence, respectively, thereby indicating no spatial distortion in the event localiza-

tion when performing simultaneous imaging. When the source was near or within a clustered region of disabled pixels, the defective pixels were interpolated by the nearest neighbouring pixels, which may have shifted the peak location of the line profile resulting in an increase in the uncertainty of the FWHM. The pixel interpolation also contributed to the blurring effect as seen in Fig. 4.5.

The absolute positioning of some of the line sources may appear to span two pixels, however this is expected if the line source is positioned such that it is not directly lined up with one row/column of the detector array. The relative distance between the sources remained the same, resulting in good agreement with the expected geometry.

4.2 Effect of Gamma Camera on MRI Performance

4.2.1 Experimental set-up

MR imaging was performed with a 16-channel array receive coil. For the purposes of testing, only one set of breast coils were used. It would not be expected that the addition of the second set would affect results significantly due to the passive nature of the coils. MR imaging was performed under the control condition, with the powered gamma camera in position but idle and during simultaneous imaging with the gamma camera. In the control condition, only the breast coils were present in the MRI bore (no gamma camera was present). Two different phantoms were used for MR image assessment; i) a breast tissue-mimicking phantom and ii) a water based phantom.

The first phantom was a lipid based phantom used to simulate breast tissue. A solution of 15 mM of sodium dodecyl sulfate (BioShop, Burlington, ON), 2% Agar, (BioShop, Burlington, ON) and gadolinium-DTPA (Magnevist, Bayer Inc.) was emulsified with 50% canola oil [125, 126]. This mixture was set in a plastic phantom measuring approximately 8 cm×8 cm×8 cm. This uniform phantom was used to measure the magnetic field homogeneity. The second phantom was a water based phantom used to simulate lesions for both MR imaging and scintigraphic imaging. Two 1.5 mL Falcon tubes were staggered in a phantom measuring ∼8 cm×10 cm× 10 cm. The Falcon tubes were used to simulate breast tumours and positioned approximately 3 cm apart in each axis, each filled with a ∼30:1 lesion to background activity concentration of Tc-99m along with 0.5 mL of gadolinium for MR contrast. This phantom was used

to characterize the SNR and geometric accuracy during sequential and simultaneous acquisition with the gamma camera.

4.2.2 Magnetic Field Homogeneity

Uniformity of the magnetic field in MRI is essential to accurately reproduce the volume within the specified field of view. Since all materials have some degree of magnetic susceptibility including the phantom/patient, there will always be some distortion in the magnetic field. The magnetic susceptibility, material geometry and size all contribute to the extent of magnetic field distortions. However, MR coils can be shimmed to optimize the MFH and minimize adverse effects in the MRI images. The molar magnetic susceptibility (χ_M) of the main components in the gamma camera are listed in Table 4.7 along with water as a reference material. The lead shielding/collimator and CZT detector exhibit the largest susceptibility values, are the largest components in the gamma camera, and are the closest components to the MR imaging volume, therefore any magnetic field distortions are likely a result of these materials.

Table 4.7: Magnetic susceptibility $\chi_m(10^{-6}\text{cm}^3\text{mol}^{-1})$ of water and materials in the gamma camera.

Material	Water	Pb	Cd	Te	Zn	Cu	C	Al
χ	-12.96	-23	-19.7	-38	-9.15	-5.46	6	16.5

B_0 field maps were acquired over the imaging volume to determine the extent of the magnetic field inhomogeneity over the imaging volume as a result of placing the gamma camera in the MRI bore. A fast gradient echo sequence was used to quantify MFH because the spinning protons dephase due to spin spin interactions and static field inhomogeneities unlike spin echo where the decay is purely from the T2 effect. The shift in the field can be determined by sampling the phase at two different echo times and the shift in the phase is the initial phase (ϕ_0) plus the shift in the Larmor frequency after a time TE given by Eqns. 4.5-4.6.

$$\phi_{TE_1} = \phi_0 + \omega_1 TE_1 \qquad (4.5) \qquad\qquad \phi_{TE_2} = \phi_0 + \omega_2 TE_2 \qquad (4.6)$$

The shift in the magnetic field (ΔB_0(T)) is the difference between the phases at different echo times where ϕ_{TE} is the phase for a specified TE divided by the difference

in echo time ΔTE as given by Eqn. 4.7. Since the gyromagnetic ratio is a constant term, the MFH is generally reported in terms of parts per million (ppm) or Hz, which indicates the variation in the magnetic field from the Larmor frequency. Magnetic field inhomogeneities exceeding 1 ppm ($\pm$63.5 Hz @ 3 T) post shim may result in signal loss and/or geometric distortions.

$$\Delta B_o = \frac{|\phi_{TE2} - \phi_{TE1}|}{\gamma_H \Delta TE} = \frac{\Delta\omega}{\gamma_H} \tag{4.7}$$

The MFH was measured with two gradient echo sequences with a small difference in echo times, according to the AAPM recommendations [110]. The breast-like lipid phantom was imaged using a 2D FGRE sequence (TR = 500 ms, flip angle = 45°)) with TE = 5 ms and TE = 8 ms. The reconstructed magnitude and phase images were reconstructed sagittally and resulted in 36 slices over a FOV = 12 cm$\times$12 cm (matrix size: 128$\times$128) with a slice thickness of 5 mm. Field maps were generated by determining the phase difference between images acquired with two different echo times on a pixel by pixel basis. Due to phase wrapping, the phase images were unwrapped using phUN [127].

The 180° RF pulse in the FGRE sequence was seen to interfere with the gamma camera communication protocol, therefore it was not possible to perform simultaneous imaging using the MRI field map protocol. As a result, B_0 field maps were not created while the gamma camera was operating. Instead, field maps were generated under the control condition (no gamma camera), with the gamma camera in place, and in both power-on and power-off mode. In the power-on state, both low voltage and high voltage power supplies were used, but no acquisition performed.

The B0 field maps were reconstructed in the sagittal plane with a slice through the center of the phantom shown in Fig. 4.6 and was displayed in terms of the shift in frequency ($\Delta\omega$). The round marker in the top left hand corner was used to identify the location of the gamma camera relative to the phantom and is also denoted in the figure. The field maps show the shift in the magnetic field between the control environment and in the presence of the gamma camera (powered only and during simultaneous imaging). A significant shift was observed in the magnetic field along the phantom boundary in the presence of the gamma camera both with and without power.

A line profile of the field map through the center of the phantom in the z-direction

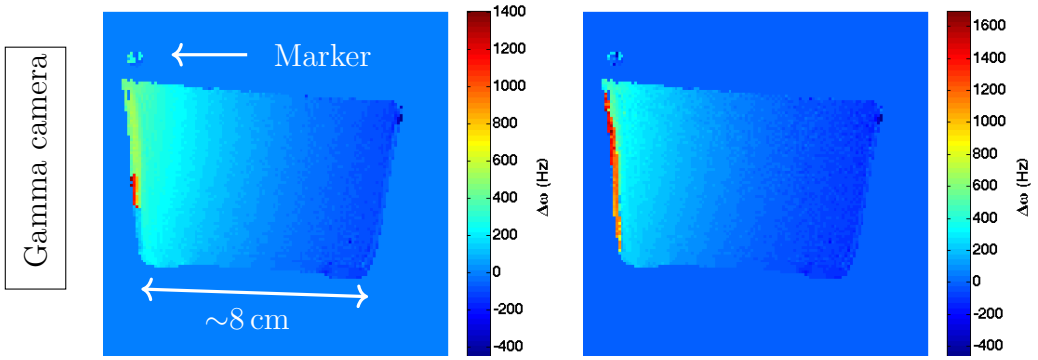

Figure 4.6: Shift in B_0 of the lipid phantom in the sagittal plane between no gamma camera present and with the gamma camera without power (Left) and with power (Right).

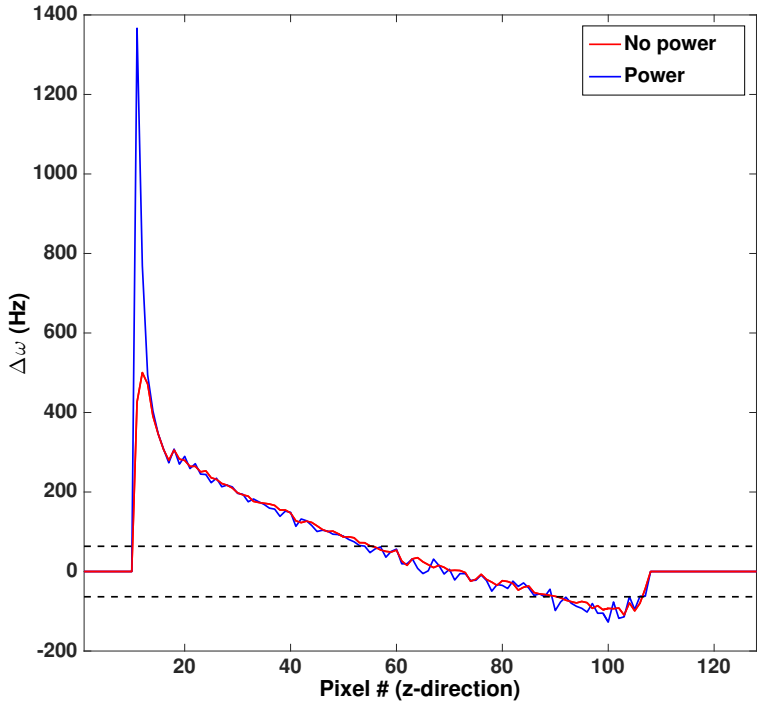

Figure 4.7: Line profile of the B0 field plane with the gamma camera with and without power.

shows the variation in the magnetic field shift in Fig. 4.7. The 1 ppm threshold is denoted by the dashed lines at ±63.5 Hz. The shift in the magnetic field of the phantom was essentially unchanged when the gamma camera was inside the MRI bore, both powered and unpowered, except at the boundary of the phantom. The maximum

shift was 4 ppm when the camera was positioned in the MRI, but not powered on, and 10 ppm while powered on. The MFH then drops to less than 2 ppm beyond 1 cm from the edge of the phantom. This shift at the boundary may manifest itself in terms of signal loss or distortion artifact but does not directly indicate the effect on the magnitude image, therefore it is important to quantify both the SNR and geometric accuracy to determine the extent of the potential impact of the CZT detector module on MRI performance.

4.2.3 Signal-to noise Ratio

The water based/Falcon tube phantom was used to explore the effect of the gamma camera on SNR, geometric accuracy, and simultaneous imaging. The MRI sequences and parameters used for MRI imaging in the control condition (no gamma camera), during sequential imaging (Seq. Img.) with the gamma camera powered but idle and during simultaneous imaging (Simul. Img.) were the same as the previous section and are described in Table 4.1. From preliminary testing, the gamma camera is unable to withstand the transmit gain adjustments during the MR pre-scan, therefore this procedure was performed prior to simultaneous imaging.

To determine if there were any significant changes in the detected RF signal as a result of the gamma camera system, the SNR was quantified using the magnitude images. Because the detected RF signal is a function of distance from the breast coils, SNR was measured in the same region of interest (ROI) for each imaging condition in order to compare resulting noise levels under simultaneous and serial imaging protocols. SNR was calculated using Eqn. 4.8, where μ_{signal} is the mean signal in an ROI specified over the phantom, σ_{noise} is the background standard deviation and 0.66 is a correction factor due to the Rician noise distribution [128]. The SNR was quantified using the magnitude images to determine if there were any significant changes in the detected RF signal as a result of the gamma camera system.

$$SNR = 0.66 \times \frac{\mu_{signal}}{\sigma_{noise}} \tag{4.8}$$

ROIs within the resultant MR images were defined as shown in Fig. 4.8. Within each selected slice containing a falcon tube denoted by 'Slice 1' and 'Slice 2', two ROIs were drawn, one inside the Falcon tube and one in the background. ROI 1 and 2 in 'Slice 1' were located in an axial slice $\sim$6 cm from the gamma camera, while ROI 1

and 2 in 'Slice 2' were in an axial slice ~ 9 cm from the gamma camera. The noise was quantified by identifying four small ROIs in each corner of the image to compensate for the potential noise variation across the field of view in the image. Tables 4.8 and 4.9 summarizes the SNR of each ROI for the two MR sequences, GRE and SPGR for each imaging condition (Fig. 4.9).

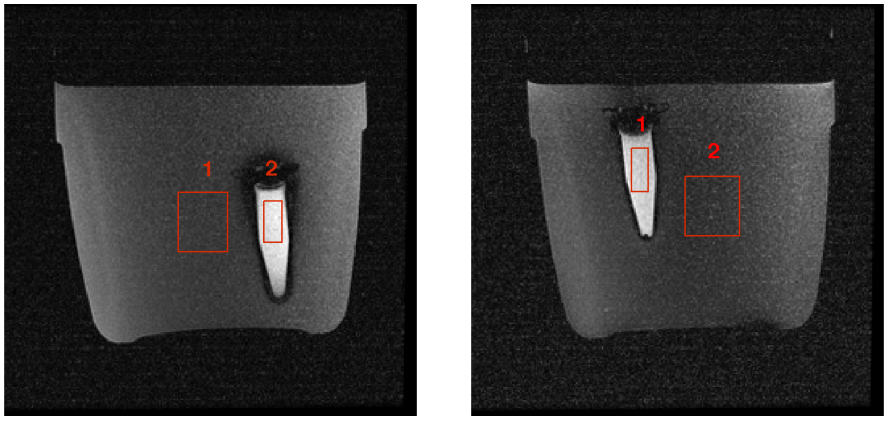

Figure 4.8: SPGR magnitude images of the phantom with powered gamma camera (Seq. Img.). ROIs defined in each slice corresponds to the Falcon tube and background: 'Slice 1' (left) and 'Slice 2' (right).

Table 4.8: SNR of selected ROIs in GRE images in Fig. 4.9.

	'Slice 1'		'Slice 2'	
	ROI 1	ROI 2	ROI 1	ROI 2
Control	82.4	95.0	62.6	78.6
Seq. Img.	16.4	14.7	10.3	11.3
Simul. Img.	2.3	2.1	1.7	1.7

When the powered gamma camera was positioned next to the breast coils, SNR decreased by 80-85 % with the GRE sequence. During simultaneous imaging with the gamma camera, the noise overpowers the signal and SNR dropped by 98 %. Similar to the SPGR sequence, SNR degradation decreased by 70-80 % with the powered gamma camera and by 93-98% during simultaneous acquisition. The decrease in SNR from sequential imaging was not a result from the non-uniformity in the magnetic field caused by the gamma camera because only the magnetic field nearest the gamma camera was significantly distorted. SNR degradation from the magnetic field inhomogeneity would imply poorer SNR near the boundary of the gamma camera and improve along the

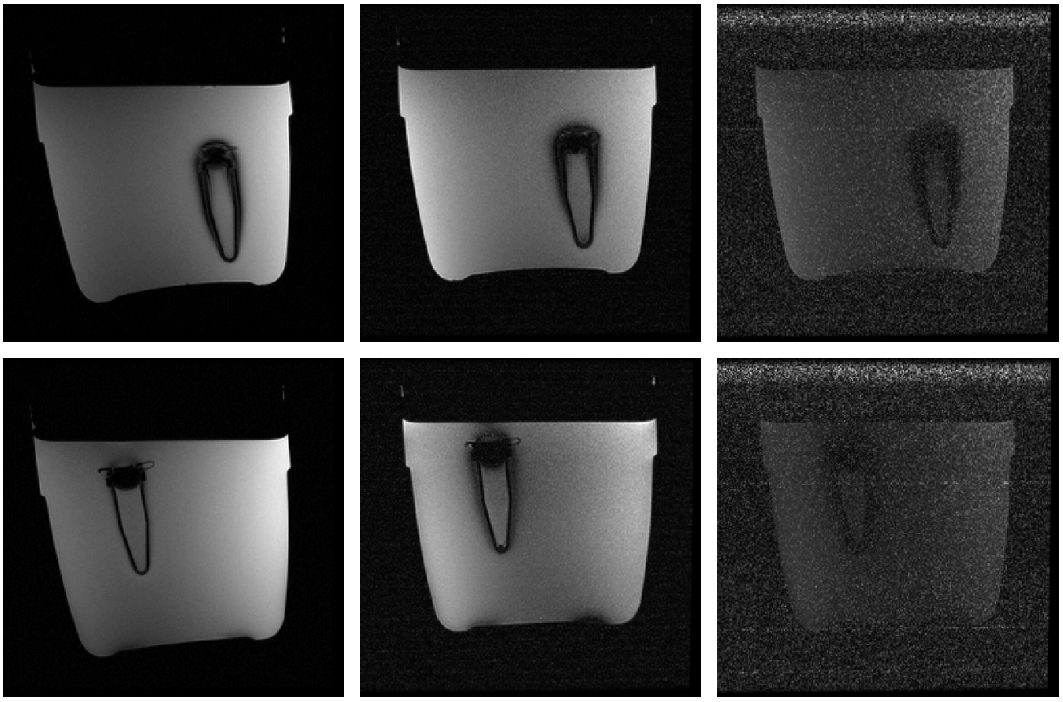

(a) Control (b) Seq. Img. (c) Simul acq

Figure 4.9: GRE magnitude images of 'Slice 1' (Top row) and 'Slice 2' (Bottom row) for each imaging condition.

axis of the bore. However, the noise level was elevated in the entire MRI field of view for all slices along the z-direction (into the bore) affecting overall SNR. While the magnetic field homogeneity was not determined for simultaneous imaging, the increase in noise was consistent across the FOV and in all slices, similar to the images acquired sequentially except with an elevated noise floor. It was evident that the decrease in SNR was a result of increased RF background noise, likely emanating from either the FPGA or ASIC on the CZT modules despite every effort to shield the gamma camera from interfering with the MRI. However, a more thorough investigation would be required to determine the source of the noise.

Table 4.9: SNR of selected ROIs in SPGR images in Fig. 4.10.

	'Slice 1'		'Slice 2'	
	ROI 1	ROI 2	ROI 1	ROI 2
Control	18.3	118.7	72.4	19.6
Seq. Img.	5.8	21.8	14	3.7
Simul. Img.	1.3	2.0	2.0	1.3

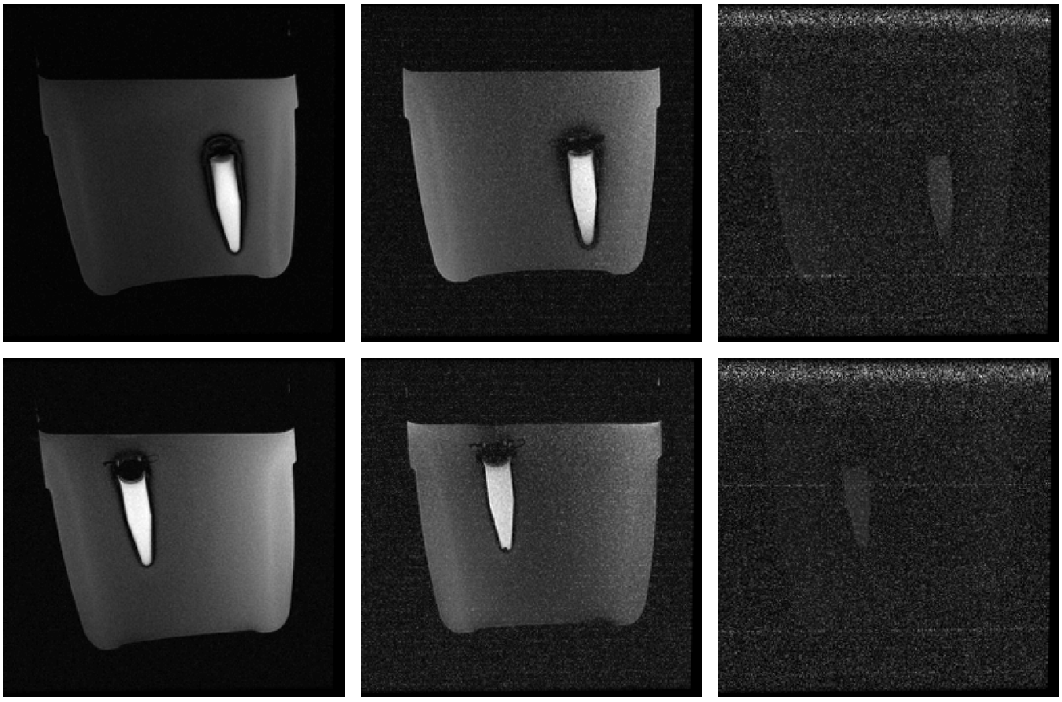

(a) Control (b) Seq. Img. (c) Simul. Img.

Figure 4.10: SPGR magnitude images of 'Slice 1' (Top row) and 'Slice 2' (Bottom row) for each imaging condition.

4.2.4 Geometric accuracy

Shifts in the magnetic field may affect the localization of the received signal potentially resulting in geometric distortions, but no obvious distortions were observed from the images when measuring SNR. In order to measure the presence of any geometric distortion as a result of interference from the gamma camera system, MR images were co-registered with CT images of the phantom. CT images were acquired with a Siemens Biograph 16 (Siemens Medical Solutions, Knoxville, TN) and used as the true reference for the phantom geometry. CT scan parameters were 32 mA (tube current), 120 kVp (tube voltage), 500 ms (exposure time), 3 mm (slice thickness) and matrix size 512×512 (0.59 mm pixels).

The resulting CT and MR images were manually co-registered through a series of linear transformations using several landmark positions as reference. An example of the co-registered images of the CT and MRI (acquired simultaneously with scintigraphic imaging) are shown separately in Fig. 4.11 for a slice passing through each Falcon tube. As the phantom was filled with water and the MR scanner bed was not completely flat

unlike the CT, the co-registration between the CT and MRI were slightly misaligned at the top boundary where the water mixture inside the phantom was not level for the MR imaging. However, several landmark positions were identified in other regions of the images for co-registration. The landmark positions were identified for each slice containing a Falcon tube denoted by 'Slice 1' and 'Slice 2' and the difference between the MRI landmark and the true location in the corresponding CT image were measured to determine if any geometric distortions were present. The measured shifts are summarized in Tables 4.10-4.13.

Three landmark positions were unresolvable and were then omitted from localization of the landmark positions. The difference between the landmark positions were fairly consistent. Any variations were less than 3 mm and were dependent on the resolvability of the phantom boundary in the presence of noise. It was found that the average shift was less than <1 pixel in both the x and y direction for each imaging condition, thereby suggesting minimal, if any geometric distortion in the MR images as a result of simultaneously acquiring gamma camera data.

Table 4.10: Difference in landmark positions between control MR image and reference CT (Images acquired sequentially).

	Control-'Slice 1'		Control - 'Slice 2'	
ROI	Δ x (mm)	Δ y (mm)	Δ x (mm)	Δ y (mm)
1	0.7	0	-0.7	1.1
2	1.1	0.7	-0.7	-0.4
3	0.7	0.7	1.1	0.4
4	-1.1	0.4	1.1	0.4
5	0.4	0	-0.7	-0.4
6	0.4	-1.1	1.1	0.4
7	-0.7	0	-1.1	0.4

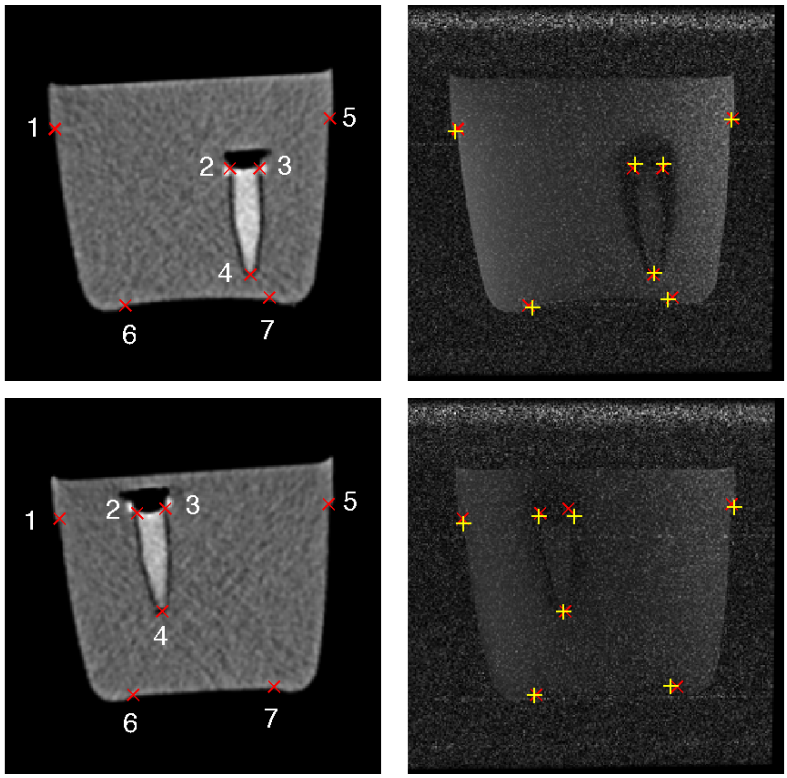

Figure 4.11: Co-registered CT image (left) and GRE image (right) acquired during simultaneous acquisition with gamma camera. Landmark positions are denoted by red x's and labelled in the CT image and are overlayed with the yellow crosses in the corresponding MR image. Top row: 'Slice 1', Bottom row: 'Slice 2'

Table 4.11: Difference in landmark positions between GRE image and reference CT (Images acquired sequentially).

	B_0 field-'Slice 1'		B_0 field -'Slice 2'	
ROI	Δ x (mm)	Δ y (mm)	Δ x (mm)	Δ y (mm)
1	0	0.4	-0.4	0.4
2	0	-0.7	1.4	-0.7
3	0.4	-1.4	1.1	0
4	0.7	0.7	0.4	0
5	0.4	0.4	-0.4	0
6	0.7	0.4	-1.1	0.4
7	-1.4	0	0	0.4

Table 4.12: Difference in landmark positions between GRE image and reference CT (Images acquired simultaneously).

	GRE sequence - 'Slice 1'		GRE sequence - 'Slice 2'	
ROI	Δ x (mm)	Δ y (mm)	Δ x (mm)	Δ y (mm)
1	-0.7	0.4	0.7	1.1
2	0.7	-1.1	0.4	1.1
3	0.4	-1.1	1.8	-1.4
4	0	-0.7	-0.7	-0.4
5	-0.4	1.1	0.7	1.1
6	0.4	0.7	0.4	1.8
7	-1.4	0.4	-1.4	-1.1

Table 4.13: Difference in landmark positions between SPGR image and reference CT (Images acquired simultaneously).

	SPGR sequence - 'Slice 1'		SPGR sequence - 'Slice 2'	
ROI	Δ x (mm)	Δ y (mm)	Δ x (mm)	Δ y (mm)
1	0.4	-0.4	0	1.1
2	0.4	0.7	0.4	-2.8
3	0	1.4	0.7	-0.4
4	0.7	-0.7	1.1	0.4
5	N/A	N/A	N/A	N/A
6	N/A	N/A	N/A	N/A
7	N/A	N/A	N/A	N/A

4.3 Simultaneous Imaging

With each imaging system evaluated independently, images from each modality were then co-registered to show the feasibility of combining the images. Scintigraphic images of the breast phantom were obtained simultaneously with the MRI sequences performed in the previous section. Despite the decreased SNR, we performed both sequential and simultaneous MR/MBI imaging using the breast-like phantom with Falcon tubes as hot spots. The phantom and the two simulated lesions (1.5 mL Falcon tubes) were filled with 0.2 MBq/mL and 6 MBq/mL of Tc-99m in water respectively. The lesions also contained 0.5 mL of gadolinium from the MRI imaging experiments. As mentioned in the previous section, the gamma camera was unable to withstand the transmit gain adjustments during the MR pre-scan, therefore this procedure was performed prior the gamma camera acquisition.

Scintigraphic data was acquired over 3 minutes into 32x32 pixel images using a 126-154 keV photopeak energy window. A total of 3×10^6 counts were obtained. The appropriate uniformity and energy correction factors from each MR acquisition sequence were applied to the gamma camera images and resultant images for no sequence, GRE and SPGR sequences are shown in Fig. 4.12. Qualitatively, there were no discernible differences in the projection images when running any of the MRI sequences. Both lesions are clearly identified for each acquisition in the scintigraphy images and no significant image artifacts are present.

The contrast to noise ratio (CNR) of each lesion was quantified to determine if there were any effect from the MRI. The CNR given in Eq. 4.9 is defined by the difference in the mean signal/counts of a defined ROI (S_L) to the mean background signal/counts (S_B) divided by the noise given by the standard deviation in the background counts σ_B. Four different ROIs were defined and highlighted in Fig. 4.12. The background ROI was selected to avoid clustered regions of disabled pixels because the interpolation of these pixels would inherently decrease the noise, thereby artificially increasing the CNR. These measurements are summarized in Table 4.14.

$$CNR = \frac{|S_L - S_B|}{\sigma_B} \tag{4.9}$$

The mean number of counts for each MRI sequence were determined in each ROI and the variation in the counts observed were within the standard deviation of the

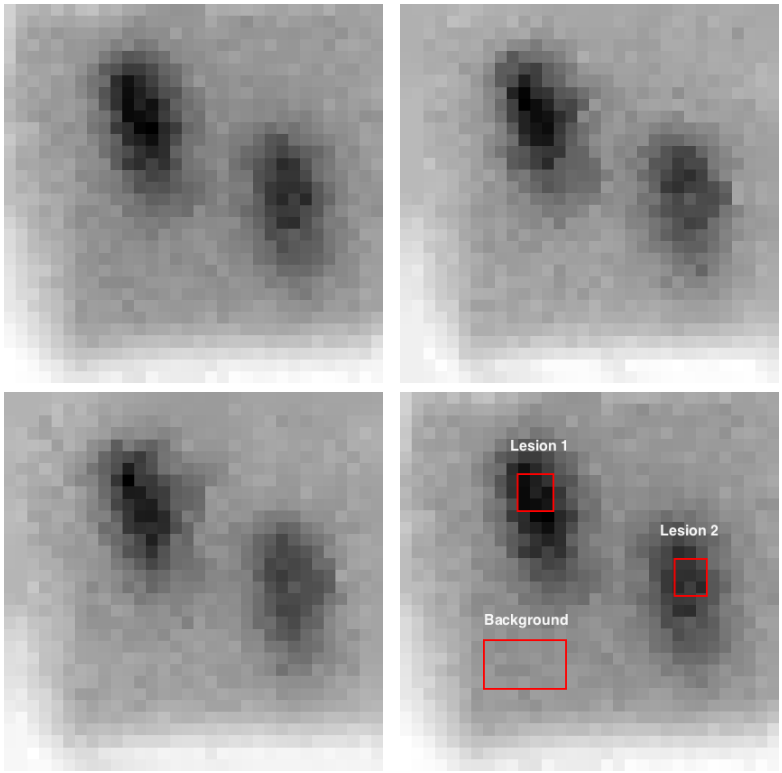

Figure 4.12: Projection images of phantom inside MRI scanner. Top row: no sequence (Left), GRE (Right). Bottom row: SPGR (Left), no sequence with overlayed ROIs for CNR quantification (Right).

mean number of counts for no MRI sequence. In 'Lesion 1', contrast increased by 6 % with the GRE sequence as compared to the condition with the B_0 field only, and decreased by less than 2 % with the SPGR sequence. 'Lesion 2' exhibited a decrease in contrast of less than 1 % and 3 % for the GRE and SPGR sequence respectively.

The noise level increased 10 % when simultaneously imaging with the GRE sequence decreasing the CNR for 'Lesion 1 and 2' by 3.5 % and 10 % respectively. There were negligible changes in CNR between no MRI sequence and the SPGR sequence. Overall, there was minimal effect from the MRI sequences on the ability to quantify CNR in regions with minimal disabled pixels. It is expected that the noise level may be skewed if there are a large proportion of disabled pixels in the background ROI.

Similar to the fused CT/MRI images, the projection images from the gamma camera were manually co-registered to the MR images. Due to lack of geometric structure in the scintigraphic image, co-registration was based on the perimeter of the phantom and the signal from the lesions. Once co-registration parameters were

Table 4.14: Contrast to noise ratio of lesions defined in Fig. 4.12

	Lesion 1		Lesion 2		Background	
	μ_{counts}	CNR	μ_{counts}	CNR	μ_{counts}	σ_{noise}
B_0 Field	2605	26.1	2258	19.3	1274	51
GRE	2638	25.2	2208	17.5	1229	56
SPGR	2562	26.0	2167	18.4	1209	52

obtained, the same transformations were performed on subsequent images acquired during the same imaging session.

While the gamma camera acquires a single 2D projection image, MRI acquires 3D multi-slice images and in this case was reconstructed along the z-direction. A maximum intensity projection of the SPGR MRI data was used to highlight the lesions in order to co-register the scintigraphy and MR images (the minimum intensity projection was used for the GRE due to decreased signal in the lesions). Fig. 4.13 depicts the fused images from sequential imaging and with simultaneous imaging.

Although the imaging area of the gamma camera was smaller than the MRI field of view, the gamma camera was able to image both lesions in addition to a portion of the phantom boundary for co-registration. The interpolation of some pixels near the lesion boundaries resulted in some minor non-uniformities, however, this effect is minimal and is dependent on the size and location of the source relative to the disabled pixels. It should be noted that the CZT modules used in this study were deemed defective by the supplier and it is expected that non-defective modules should not suffer from the same effects. These early results are promising for quantitative testing to characterize the gamma camera performance in simultaneous imaging conditions but additional work is required to address the SNR degradation in the MR images.

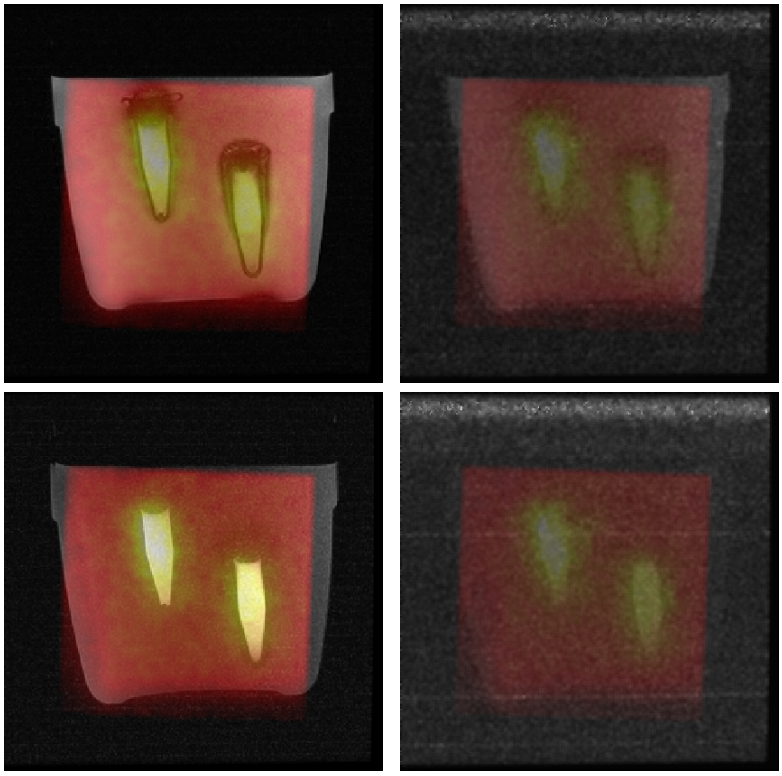

Figure 4.13: Projection image fused with projected MRI images. Top row: GRE sequence acquired sequentially (Left) and simultaneously (Right). Bottom row: SPGR sequence acquired sequentially (Left) and simultaneously (Right)

4.4 Discussion

4.4.1 Design

With careful consideration of avoiding the use of ferromagnetic components, an MRI-compatible gamma camera using CZT detectors was developed with promising results. The design was based on a small area gamma camera prototype with the ability to be tiled into a larger area array similar to that of a commercial MBI system. The proposed system required minimal adaptation to the existing MRI system.

MBI would ideally be performed with the gamma camera parallel to the breast coils so that the projection images would be in the plane with the least amount of scattering tissue. However, the structure of the frame holding the breast coils prevented the gamma camera from fitting between the coils and the bore boundary. Therefore, initial tests for simultaneous imaging with the gamma camera were performed with it oriented

down the centre of the bore, perpendicular to the coils. Dedicated MBI is performed with the patient sitting upright similar to mammography, but in the combined system, the patient is lying prone. This configuration improves the FOV coverage for MBI because the breast tissue is naturally pulled away from the chest wall by gravity.

Part of the design requirement is that the gamma camera must be compact enough to fit within the bore with the breast coils while maximizing the system performance. Our gamma camera readout system was designed to alternate between four modules via a single microntroller. Each module can theoretically detect up to 1×10^6 cps but the maximum observable count rate of the system was 100 kcps (when the defective pixels were not disabled) which is less than the maximum count rate for current scintigraphic imaging systems (300-500 kcps). However, the main count rate limitation is due to the CZT module as detailed by the manufacturer's documentation with a maximum detectable count rate of 60 kcps per module [129, 130]. The overhead time requirement associated with the multiple module readout included the time to enable the chip select, check if the module was ready to send the event, and read the entire event frame. The amount of time to process one event was approximately 2.5 µs, limiting the system to a theoretical count rate of 200 kcps (which is greater than the module count rate limit). In addition, the GPIO pin and timer must be sampled after each event to determine if there are still events available to be read from the FIFO.

Given the results of the current gamma camera system and the count rate capability of each individual module, adjustments to the readout process such as dedicated microcontrollers for each module, or implementation of an FPGA, and including timer interrupts could improve the event through-put and increase the count rate. However, the size of the gamma camera would increase substantially with a 1:1 module to microcontroller design, if more modules were to be tiled to a larger array to match the FOV of a typical MBI system.

4.4.2 Effect of MRI on Gamma Camera Performance

In the absence of a radioactive source in normal imaging conditions and in the presence of a static 3 T magnetic field, there were negligible counts detected. Background counts were induced in the CZT detector modules during each MRI sequence. The extent of the induced counts were dependent on the sequence and location with respect to the isocentre. The additional counts originated from specific pixels in the CZT module since each detected event satisfied the error checks implemented in the event readout

process. Considering the majority of the pixels (∼90%) were unaffected by the MRI sequences (in the UFOV and CFOV) and the CZT detector modules used for this investigation were rejected from the factory for unknown reasons, it might be expected that production modules should have fewer defective pixels.

Energy resolution remained mostly unaffected by MRI acquisition sequences with an average energy resolution at 140 keV equal to approximately 7.3 % when operated both outside and inside the MRI bore. The maximum increase during an MRI sequence was less than 1 %, indicating a minimal effect. The measured energy resolution at 140 keV exceeded the manufacturer's expected 6.4 % at 122 keV. This occurred because the energy correction was performed with only the 140 keV peak, assuming a linear response to 0 keV. In actuality, the response of the detector was linear as shown in Fig. 3.12, but did not extrapolate through the origin as assumed for the purposes of testing inside the MRI. The energy calibration factors obtained outside the MRI using three different energy peaks (122 keV, 140 keV and 171 keV) resulted in a 6.2 % FWHM energy resolution at 122 keV, matching the manufacturer's specification. Due to the unknown pixel response inside the MRI bore, the energy correction factors could not be applied between different imaging conditions. For consistency and comparison to the measurements inside the MRI scanner, Tc-99m was used for all performance measurements and a separate energy correction map was generated for each imaging condition. To determine if the different imaging conditions had an effect on the energy calibration factors, pixel maps of the difference in peak ADC channel between two sets of data acquired in the control condition were generated and compared with the pixel maps between the control and each imaging condition in Fig. 4.14 (Recall from Eq. 3.2 that the energy calibration factor for each pixel is $140/\mathrm{E}_{ADC}(140\,\mathrm{keV})$, therefore the calibration factor is proportional to the peak ADC channel). The mean shift of the peak ADC channel ($\overline{\Delta E_{ADC}}$) from each imaging condition to the control condition was reported. The disabled pixels were excluded when calculating the mean peak ADC channel. The mean shift in the peak ADC channel with the gamma camera outside the MRI was 4±12 between each acquisition. In the presence of the B_0 field only, during the GRE and SPGR sequence, the mean shift was 18±41, 9±36, and 8±34. For each of the imaging conditions inside the MRI bore, the mean shift in the ADC channel for the B_0 field only was approximately 4.5 times greater than the mean shift from acquisitions outside the MRI room and during simultaneous imaging, the mean shift was two times the mean shift observed outside the MRI room. Simultaneous imaging

affected these defective pixels such that they had to be disabled prior to imaging. However, the sensitivity of these pixels inside the MRI scanner were not severe enough to affect overall performance but did contribute to an increase in the mean peak ADC shift.

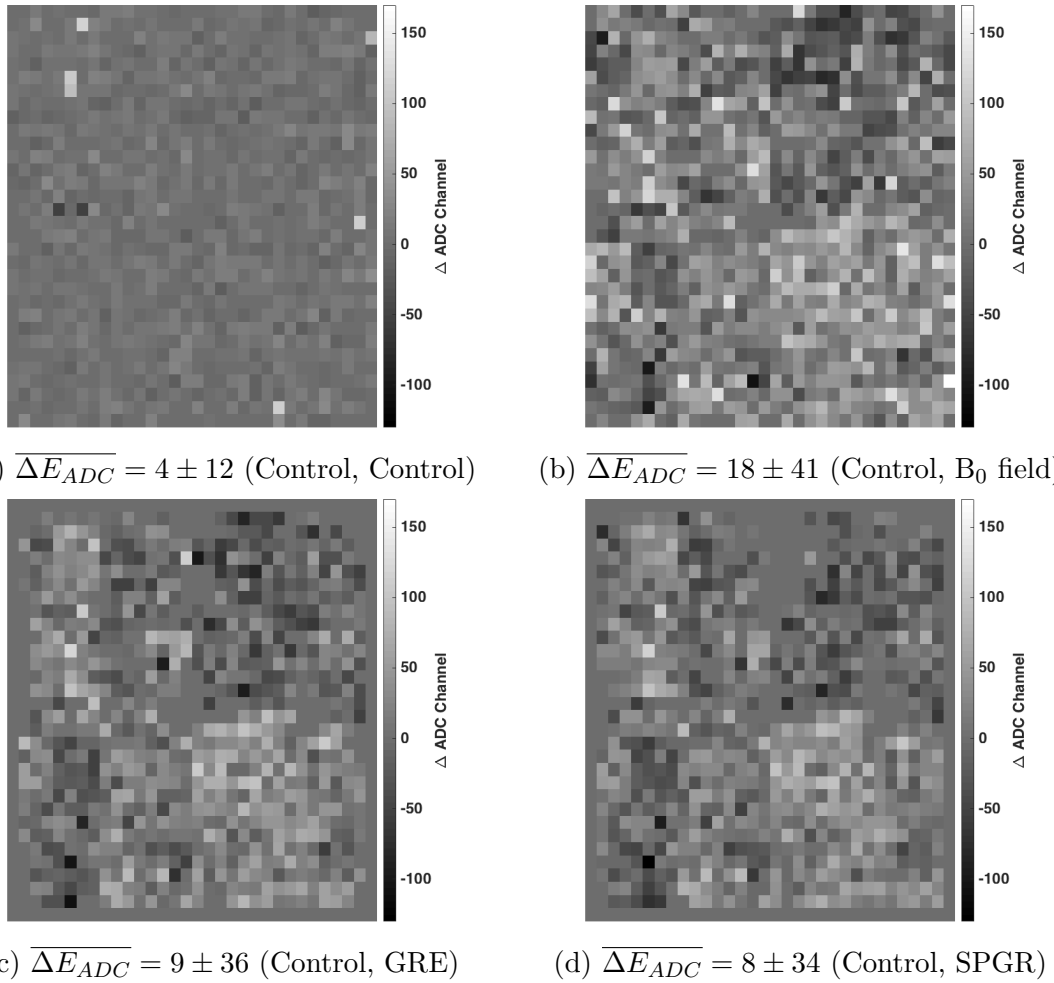

(a) $\overline{\Delta E_{ADC}} = 4 \pm 12$ (Control, Control)

(b) $\overline{\Delta E_{ADC}} = 18 \pm 41$ (Control, B_0 field)

(c) $\overline{\Delta E_{ADC}} = 9 \pm 36$ (Control, GRE)

(d) $\overline{\Delta E_{ADC}} = 8 \pm 34$ (Control, SPGR)

Figure 4.14: Pixel map of the shift in peak ADC channel compared to the control condition (outside the MRI room).

In addition, the pixel map showing the energy resolution of each individual pixel is shown in Fig. 4.15. The average energy resolution of the individual pixels excluding disabled pixels from each imaging condition based on one energy peak were within the standard deviation expected for the control condition. Overall, there were no significant effects on the energy resolution except that while inside the MRI bore, there tended to be some variation in the ADC peak channel. Additional acquisitions would

confirm the reproducibility of these results for each imaging condition. Evaluation with multiple energy peaks in the MRI would confirm the the appropriate energy correction factors. While there may be a shift in response from the control condition, the response from all three imaging conditions inside the MRI scanner were comparable.

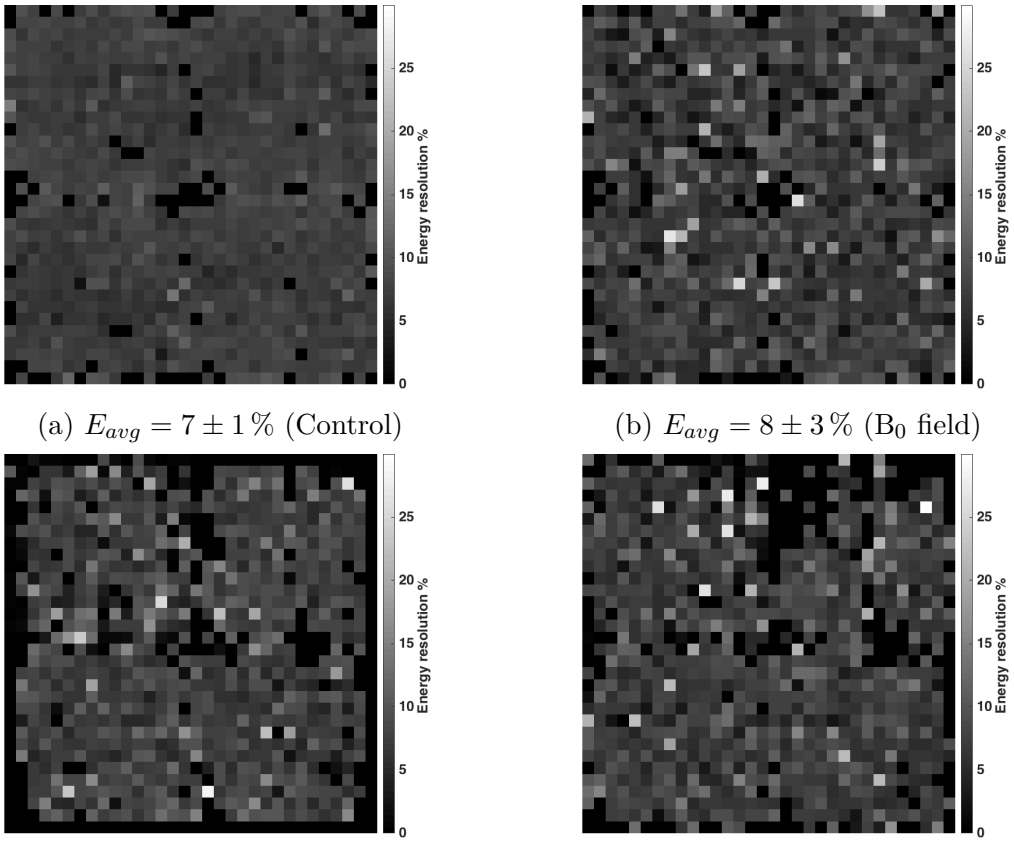

(a) $E_{avg} = 7 \pm 1\,\%$ (Control)

(b) $E_{avg} = 8 \pm 3\,\%$ (B_0 field)

(c) $E_{avg} = 9 \pm 3\,\%$ (GRE)

(d) $E_{avg} = 9 \pm 3\,\%$ (SPGR)

Figure 4.15: Energy resolution pixel map for each imaging condition.

Despite the variation in the peak ADC channel, the average resolution remains essentially the same. These results were not surprising, since other groups investigating CZT for use in large magnetic fields noted similar responses [105, 131] and the energy resolution is comparable to current MBI systems. In addition, the discrepancy in energy resolution poses minimal effect on image quality, as a previous study showed that varying levels of energy resolution did not significantly affect tumour contrast in MBI [132].

The proposed gamma camera system exhibits on average, slightly higher non-uniformities, IU = 5-8 % and DU = 4-6 % in comparison to standard gamma cameras

(IU and DU typically $\leq$4 % and $\leq$2 % respectively). The module in location '1' consistently exhibited larger non-uniformities compared to the other modules, thus contributing to the larger values for the UFOV and CFOV. This was observed regardless of the imaging condition and the physical module in that particular module location in the gamma camera. Yet, this effect was not observed when any combination of 1-3 modules were active. Therefore, the non-uniformity in module location '1' was most likely due to a sampling error when reading the status of the GPIO pins. Each of the GPIO pins are sampled sequentially and a logic high indicates events are available to be read from the corresponding module.

An increase in the non-uniformity was also observed for each individual module as well as the UFOV and CFOV. Since the modules were considered defective from the manufacturer, some potential crystal defects may make pixels more susceptible to certain MRI sequences, thus accounting for slight changes in the uniformity during different MR acquisitions. Improvements in the the manufacturing process of Redlen CZT modules have led to minimal defects suggesting that fewer pixels would have to be disabled in modules which satisfy the quality standards [133].

The cluster fraction is indicative of the relative locations of defective pixels to one another. The more clustered the pixels are, the higher the probability that pixel interpolation will be based on other interpolated pixels, thus lowering image quality. The drawback of the cluster fraction is that it doesn't define the distribution of the clustered pixels. It doesn't characterize if they are grouped all in the centre, spread around the perimeter, or sectioned into smaller groups based on the definition of the cluster fraction. Most of the disabled pixels were located around the the perimeter of each module. During each MRI sequence, a number of additional pixels were deemed to be defective, but mostly along each of the module boundaries with some larger clusters located near the boundaries.

The spatial resolution of the gamma camera system during simultaneous imaging remained comparable to the spatial resolution when measured outside the MRI. The maximum shift in the FWHM for each source to collimator distance and each imaging condition was less than 0.7 mm ($<$ 1 pixel) indicating negligible effect on the spatial resolution. In addition, the gamma camera system was able to reproduce the spatial position of two Tc-99m line sources consistently and accurately in both dimensions. The interpolation of disabled pixels increased the error associated with the peak position. However, based on these results, the MRI was seen to exhibit minimal effect on the

overall performance of the gamma camera when operated with the GRE and SPGR acquisition sequences.

Given that simultaneous imaging is feasible with the gamma camera inside the MR bore, performance measurements would benefit from the calibration between two gamma energies within the dynamic range of the detector.

4.4.3 Effect of Gamma camera on MRI Performance

In terms of MR imaging performance, we have noted a significant shift (up to 10 ppm) of the B_0 map in the region closest to the gamma camera, but decreasing to 2 ppm within 1 cm of the phantom. The clinically acceptable threshold for field inhomogeneity is approximately 1 ppm @ 3 T over a spherical diameter of 35 cm and while our system introduces inhomogeneities which exceed this value, no noticeable spatial distortion in the resultant images were noted. Clinical MR breast imaging typically makes use of a fat saturation technique to suppress signal from adipose tissue because the resonance of fat is similar to water (Fig. 4.16). However, this requires a MFH of 1.7 ppm to differentiate the 3.4 ppm chemical shift between hydrogen nuclei in fat vs. water [134]. Based on our B_0 field maps, fat saturation may be possible in regions with a shift less than 1.7 ppm, but is not feasible within the entire imaging volume. Therefore, there may be some limitations in which sequences are useful for combined MBI/breast MRI.

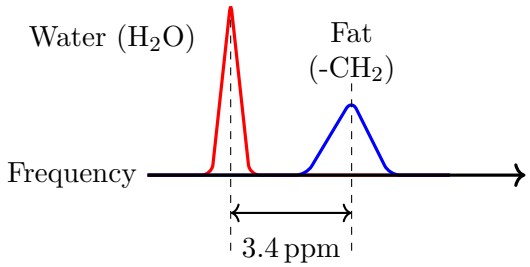

Figure 4.16: Resonance spectrum of fat and water.

In reference to Chapter 2, the main sequences used in a breast MRI protocol are GRE and SE. The typical SE sequence is comprised of an initial 90° RF pulse followed by a 180° refocusing pulse. The GRE uses a flip angle less than 90° and the echo is generated with a bipolar gradient. Some breast protocols use SPGR, a variant of the GRE which spoils any residual transverse magnetization from the echo prior to the next RF excitation. The transmit gain of the B1 field (applied RF pulse) is dependent

on the properties of the phantom and the requirements of the scan parameters. During the pre-scan, the transmit gain is adjusted such that the RF signal detected matches the voltage range of the ADC converter. Initial tests determined the intensity of the 180° RF pulse in the spin echo sequence caused the microcontroller to miscommunicate with the modules rendering EDR mode inoperable and requiring the gamma camera to be reset. EDR mode was successfully executed simultaneously with the GRE and SPGR sequence which used a lower flip angle and no 180° rephasing pulse.

The SNR in each ROI was determined over several regions in the MRI images and a significant increase in noise was observed in the entire field of view overshadowing any effect from any magnetic field inhomogeneities. A previous study investigating dual modality imaging using a 2.54 cm×2.54 cm area CZT detector inside a 4 T MRI reported a decrease in MR SNR of ∼50 % [97]. However, we have seen reductions of upwards of 98 % in our system during simultaneous acquisition, rendering the phantom and the simulated lesions nearly unresolvable. It should be noted that across all images, there was an increase in noise rather than a decrease in signal. The RF noise was seen to increase two-fold when the camera is powered on, but increased nearly 15 times when acquiring data simultaneously.

It is postulated that the breast coils were sensitive to the extraneous RF noise from the gamma camera, despite every effort to shield the gamma camera from both interference from the MRI and to the gamma camera. This effect was seen to correlate with the detected count rate, thus indicating the source being from either the analog front-end or the digital readout of the gamma camera system. Based on the results from previous studies investigating RF shielding, it was expected that the combination of the carbon fiber casing and copper tape shielding should have been sufficient to attenuate the RF to impenetrable levels. The regions not covered with the copper tape were located at the power connector openings and the holes were less than 2 cm in diameter. For optimal shielding it was recommended that the any apertures in the shielding should not exceed $\lambda/20$ for a 40 dB attenuation and $\lambda/50$ for a 60 dB attenuation [135], which corresponds to apertures of 12 cm and 5 cm respectively (for f=127.74 MHz). The aperture of in the gamma camera is well below the recommended limits for up to a 60 dB attenuation. All cables were grounded to both the penetration panel of the MRI room and shielded. The lengths of the cables were specifically chosen to be long enough to extend to the perimeter of the room except the USB cable which extended to the control room, but it was ensured that the cable lengths were not

multiples of the RF wavelength at 3 T (26 cm). It is evident that although there was no significant degradation in the gamma camera performance, both modalities suffered from effects resulting from inadequate or inefficient shielding. A reassessment of the current shielding configuration may address the RF contamination from the gamma camera in the MRI signal and vice versa.

4.4.4 Combined Molecular/MR breast Imaging

The fused scintigraphy/MR images showed that the two images are well correlated. In the particular phantom used, there were no significant effects from the interpolation of defective pixels during simultaneous acquisition. CNR of the simulated lesions were minimally affected. However, if lesions were comparable in size to the defective pixel cluster region and located within the pixel cluster region, an underestimation of the uptake may lead to a false negative diagnosis. As stated earlier, the majority of the pixels were unaffected with simultaneous imaging with MRI, and disabled pixels were most likely a result of the defective nature of the module. However, further testing with modules which satisfies the manufacturer's quality control standards would be required to confirm this. There were no obvious geometric distortions in the fused scintigraphy/MRI images and aside from the degradation in SNR, the feasibility of simultaneous MBI/MRI is promising.

Chapter 5

Backscatter Imaging in MBI

Dose reduction remains an ongoing objective in MBI and the investigation of backscatter photons within the scatter spectrum may potentially increase count sensitivity and/or image contrast to noise. If the contrast to noise ratio improves with backscatter photons, a decrease in administered dose to the patient may be possible if image quality metrics are on par with the full dose protocol without backscatter photons. These backscatter photons undergo a 180° scatter with the same spatial information as primary photons, but are blurred by the response from the collimator more than primary photons because the distance from the interaction to the collimator is greater.

Projection images are based on setting an energy window around the primary photopeak. The remaining spectrum consists of single and multiple Compton scatters (including backscatter photons) as well as characteristic X-rays from the collimator and shielding material. Scattered photons contaminate the projection image decreasing image contrast because of the inability to discriminate photons based on the origin of the emission. The effect of scattered photon contribution is also significant for dual isotope imaging because of down-scatter from the higher energy peak into the lower photopeak window. Backscatter photons cannot be isolated from the scatter spectrum because of insufficient spatial information. Therefore, some form of scatter correction must be applied to compensate for the inclusion of multiple Compton scattered photons from the backscatter photons. While no method can strictly remove all scattered photons, the scatter contribution can be estimated based on energy based methods such as dual energy and triple energy window (TEW) compensation and spatial based methods using scatter models. In this chapter, a window based scatter estimation method called the triple energy window (TEW) method was investigated to extract the backscatter photons from the total energy spectrum of a Tc-99m filled source within several geometries described in the following section. The TEW method was selected for it's success in dual isotope imaging for removing down-scattered and multiple Compton scatters from the lower energy peak [116]. For Tc-99m with a primary emission of 140 keV, the energy of the backscatter peak according to the Compton scattering equation is 90.4 keV. The TEW estimates the scatter contribution around the backscatter peak using a trapezoidal approximation and scaling the number of counts in the upper and lower energy windows directly adjacent to a defined backscatter window. Several energy windows were investigated for the main and subwindow widths in the TEW equation (Eq. 2.8) and compared to the true backscatter photons.

Following this, the optimal TEW parameters were applied to a lesion simulation study to determine if there was any appreciable increase in the contrast to noise ratio (CNR) from backscatter photons.

5.1 Simulation Parameters

Monte Carlo simulations of the gamma camera using the parameters of the system designed in Chapter 4, with several different phantom geometries were performed using GATE (GEANT4 application for tomographic emission) [136]. For the purposes of this simulation study, the CZT detector was modeled as an ideal semiconductor. While GATE includes the appropriate physical processes for all materials defined, CZT exhibits a characteristic response specific to semiconductor detectors which results in a low energy tail in the energy spectrum that was not modelled in the Geant4 platform. The system parameters for the GATE simulation are summarized in Table 5.1 below. The minimum energy threshold was set to 5 keV and the maximum to 150 keV.

Table 5.1: Gamma camera parameters

Collimator Parameters	Detector Parameters
Material: Lead	Material: CZT
Hole length: 2.54 cm	Thickness: 5 mm
Hole inradius: 0.55 mm	Pixel size: 2.4 mm × 2.4 mm
Hole shape: Hexagonal	Pixel array: 32 × 32

Before investigating the TEW method, the true backscatter photons were determined by simulating a phantom with a radioactive source and analyzing the single Compton-scattered photons in the Monte Carlo generated energy spectrum. This served as the baseline comparison for the optimal energy windows to recover backscatter photons using TEW. For the true backscatter photons, simulations were performed with a line source (tube with inner diameter = 1 mm and length = 10 cm) filled with 45 MBq of Tc-99m inside a cubic phantom (density = 1.02 g/cm^3) measuring 10 cm×10 cm with thickness ranging from 1 cm to 6 cm in 1 cm increments (Fig. 5.1a). The source and phantom were positioned at the collimator face and the gamma camera was simulated with 0.1 % and 7 % energy resolution at 140 keV. Each backscatter thickness was simulated for a 1 minute acquisition.

The next set of simulations compared the true backscatter photons to the TEW estimated backscatter photons with varying levels of forward and back scatter thicknesses with an idealized line source. The simulation specifications were the same as the previous parameters except the phantom thickness was fixed at 6 cm and the line source was simulated at various source to collimator distances ranging from 1 cm to 6 cm (Fig. 5.1b). Each backscatter thickness was simulated with a 1 minute acquisition time. This correlated with a decrease in forward scatter material as backscatter material increased to match the thickness of the breast phantom. The count sensitivity and spatial resolution were measured with this phantom geometry and the backscatter photons were compared with the photopeak data. An example of the GATE visualization with the gamma camera and phantom is shown in Fig. 5.2.

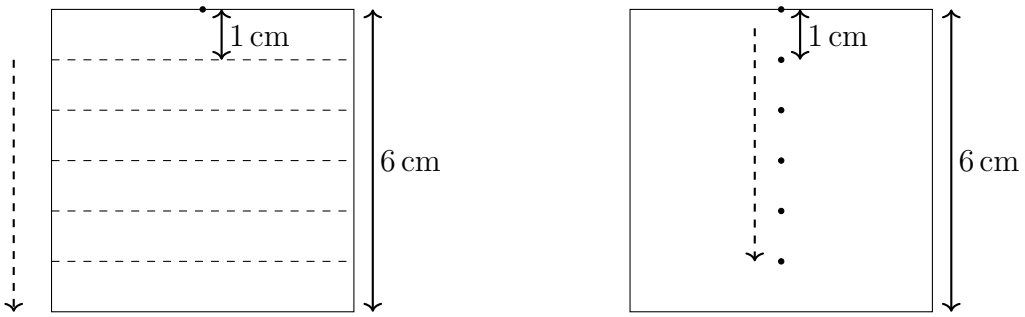

(a) Fixed source with increasing backscatter material thickness

(b) Fixed phantom thickness with increasing source to collimator distance

Figure 5.1: Phantom geometry with backscatter material only (Left) and phantom geometry including forward and back scatter material (Right).

To determine the effect of backscatter photons on the lesion contrast to noise ratio (CNR), the same phantom geometry was used as in the previous simulations except four lesions of various radii replaced the line source. Three sets of simulations were performed with four different lesions with radii 1.5 mm, 2.5 mm, 5 mm and 10 mm labeled L1-L4, respectively with a system resolution of 7 % at 140 keV. The first simulation S1, was performed with 1 cm of backscatter material and 5 cm of forward scattering material, S2 had equal amounts of forward and back scatter material (3 cm). In the third set of simulations S3, lesions were positioned with 1 cm of forward scatter material and 5 cm of backscatter material. Each geometry was simulated for a 1 minute acquisition acquisition time. All lesions were composed of simulated breast tissue and filled with a 20:1 lesion to background activity concentration of Tc-99m. Previous phantom studies showed that this activity concentration correlated with the clinically

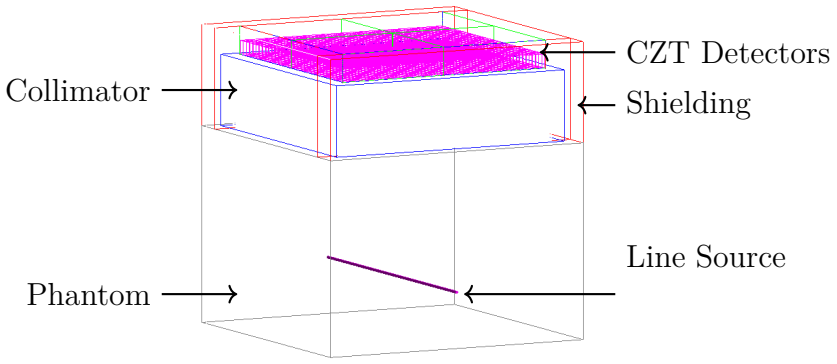

Figure 5.2: Visualization of the GATE simulation - Gamma camera with a line source within a phantom.

observed lesion CNR [64, 137]. The absolute concentration of the four lesions were 0.02 MBq/cm^3 each and 0.001 MBq/cm^3 in the phantom and the arrangement of the lesions are illustrated in Fig. 5.3. The ability to extract the backscatter photons and quantify the effect on image quality will determine if the inclusion of backscatter photons improved image quality.

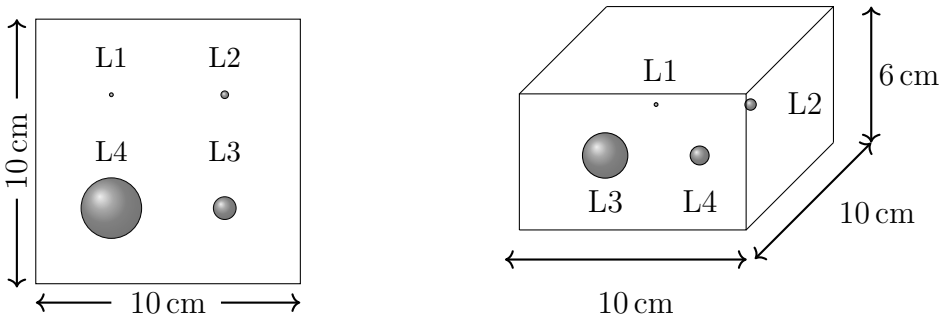

Figure 5.3: Lesion arrangement for GATE simulations: Gamma projection plane (Left) and phantom cross section with 3 cm of forward scatter and 3 cm of back scatter material (Right).

5.2 True Backscatter Photons

The number of true backscatter photons is dependent on the energy resolution and angle acceptance window of wide angle scatters. The backscatter acceptance window is the quadrature sum of these two effects, where E_{sys} is the energy resolution of the

gamma camera system of the Tc-99m backscatter peak at 90.4 keV and E_{comp} is the energy window corresponding to a defined angle acceptance window. A 7 % energy resolution at 140 keV corresponds to an E_{sys} of 10.8 % ($\sim$ 11 %) energy resolution at 90.4 keV. This means that true backscatter photons could be detected within $\pm$4.9 keV from the backscatter peak which corresponds to an angle acceptance of up to 135° from the incident photon (or $\pm$45° from the backscatter angle). If we only accept true backscatter photons ($\pm$1°), the energy window due to Compton scattering (E_{comp}) would be 0.1% at 90.4 keV. The backscatter energy window is then limited by the energy resolution of the system and the backscatter energy window is approximately 11% as given in Eq. 5.1.

$$Backscatter\ energy\ window = \sqrt{E_{sys}^2 + E_{Comp}^2} \tag{5.1}$$

Fig. 5.4 summarizes the total energy spectrum and the single Compton scatter spectrum with 0.1 % and 7 % energy resolution at 140 keV for 6 cm of backscatter material, illustrating the differences in single Compton scatters between a purely angle-dependent energy window and the system energy resolution of a typical gamma camera. The energy resolution of the system has the greatest impact in the photopeak window, whereas the scatter portion of the energy spectrum was mostly unaffected because of the continuum of scattered photon energies. If we consider backscatter photons with one Compton interaction within a $\pm$8° range (0.1 % energy resolution at 140 keV corresponds to a resolution of 0.5 % centred at 90.4 keV) from a 180° scatter for the near-perfect system, the total number of true backscatters account for less than 1 % of the photopeak photons and there is minimal scatter contribution to the line profile as illustrated in Fig. 5.5. In the case of the system with 7 % energy resolution at 140 keV, the total number of photons in a 0.5% window are approximately the same, however, the backscatter photons have a wider spatial distribution within the scatter spectrum increasing the spatial FWHM. So while the scatter spectrum looks similar for both systems, the spatial distribution of the photons are dependent on the energy resolution of the system as evident in the summed line profiles of the corresponding energy windows in Fig. 5.5. A 7 % energy resolution at 140 keV corresponds to an energy window of 11 % to encompass all spatially relevant backscatter photons. This includes photons scattered 45° from the photopeak, but it is postulated that the decrease in spatial resolution will be insignificant because there is a higher probability of interaction near the source of origin rather than further away due to photon attenuation. For

a system resolution of 0.1 %, the spatial distribution of the line profile for an 11 % energy window is equal to the 7% system because both include all backscatters plus additional scattered photons.

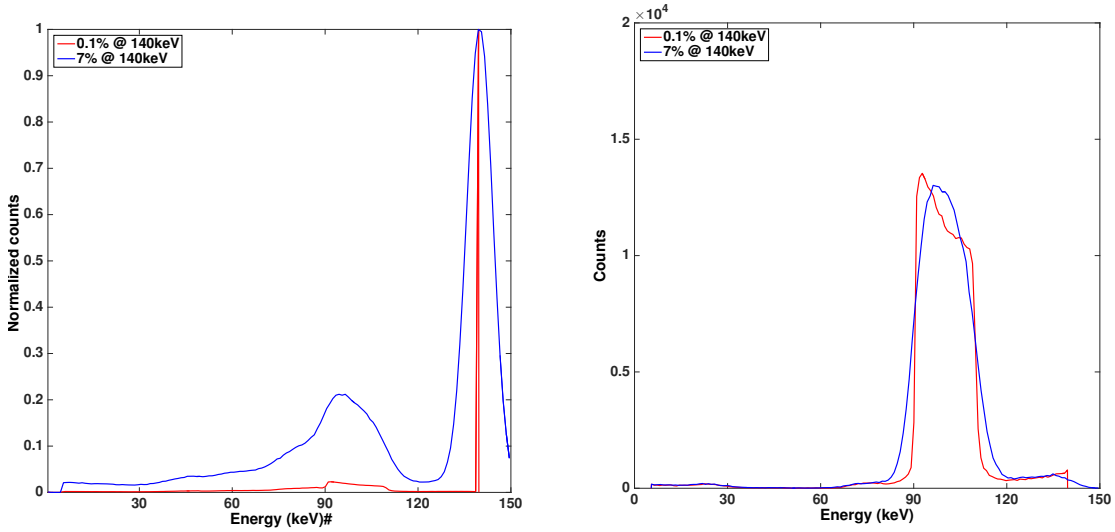

Figure 5.4: Energy spectra of Tc-99m for the phantom geometry shown in Fig.5.1a with 6 cm of backscatter material: Total (left) and first order scatter (right)

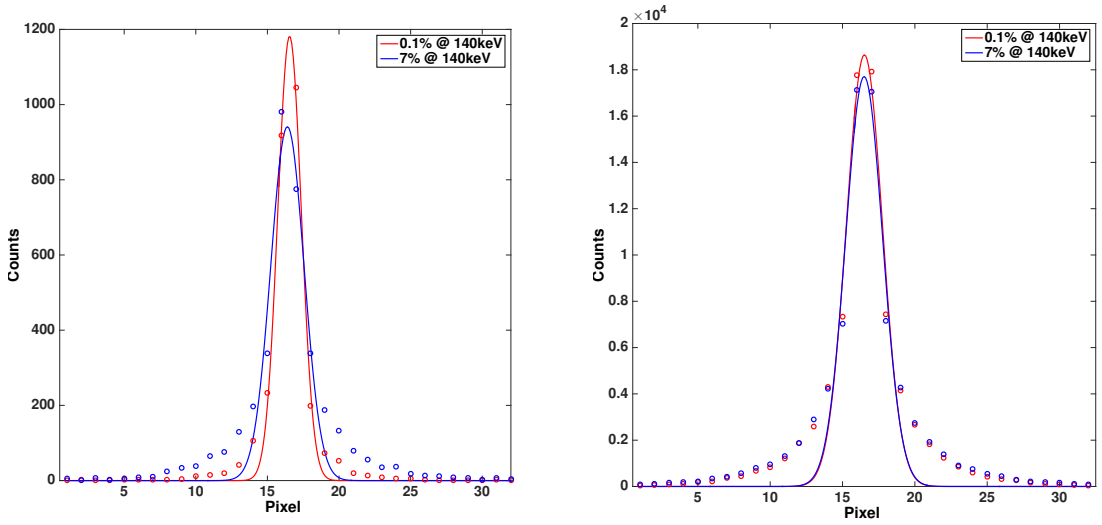

Figure 5.5: Summed line profile with 6 cm of backscatter material represented by circle data points with a Gaussian fit over the peak represented by a solid line: 0.5% window (Left) and 11% window (Right) centred at 90.4 keV

While the probability of backscattering is not influenced by the amount of forward scatter material, the proportion of backscatter photons to photopeak photons is depen-

dent on the amount of forward and backscatter material present due to attenuation. The backscatter photon yield and spatial resolution were compared for two phantom geometries as a function of backscatter thickness in Fig. 5.6 using the gamma camera with 7 % energy resolution. For the first phantom geometry, the source was fixed at the collimator face with increasing backscatter thickness ranging from 1 cm to 6 cm in the absence of forward attenuating/scatter material. The second geometry used a fixed phantom thickness with the source to collimator distance increasing from 1 cm to 6 cm (ie. For 1 cm of backscatter material, there was 5 cm of forward scatter material). The number of backscatter photons detected was dependent on the amount of attenuation material present as depicted in Fig. 5.6 (Left). In the case of backscatter material only, the yield increased with increasing backscatter thickness, but pleateaued around 5 cm when the probability of backscatter matched that of further photon attenuation. When the line source was moved away from the collimator, the proportion of forward scatter material increased for decreasing backscatter thickness It was evident that an increase in forward scatter material significantly degraded the total number of backscatter counts due to attenuation. This was also in part due to the decreased ratio of back to forward scatter material. The spatial resolution was determined by fitting a Gaussian function to the summed line profile. The FWHM is defined by Eqn. 5.2, where σ is the standard deviation of the Gaussian function and 2.4 mm is the intrinsic resolution of the system.

$$FWHM(mm) = \sigma(pixel) \times 2.35 \times 2.4mm/pixel. \tag{5.2}$$

The FWHM of the backscatter peak with and without forward scatter material was plotted as a function of the backscatter thickness in Fig. 5.6 (Right). The FWHM increased due to the blurred collimator response function from interactions with increasing backscatter thickness but also plateaued from the limited yield of backscatter photons. The FWHM for the phantom with fixed thickness increased by 70-80 % for 1-3 cm backscatter thickness due to the increase in attenuating material between the backscatter material and collimator.

To compare the ratio of backscatter photons to the photopeak photons for a fixed phantom thickness, the true number of photopeak photons was determined by summing the number of primary photons (only photons with no interactions) within a 20 % energy window centered at 140 keV. The absolute number of photopeak and backscatter photons are summarized in Table 5.2. The theoretical gain in the total number of

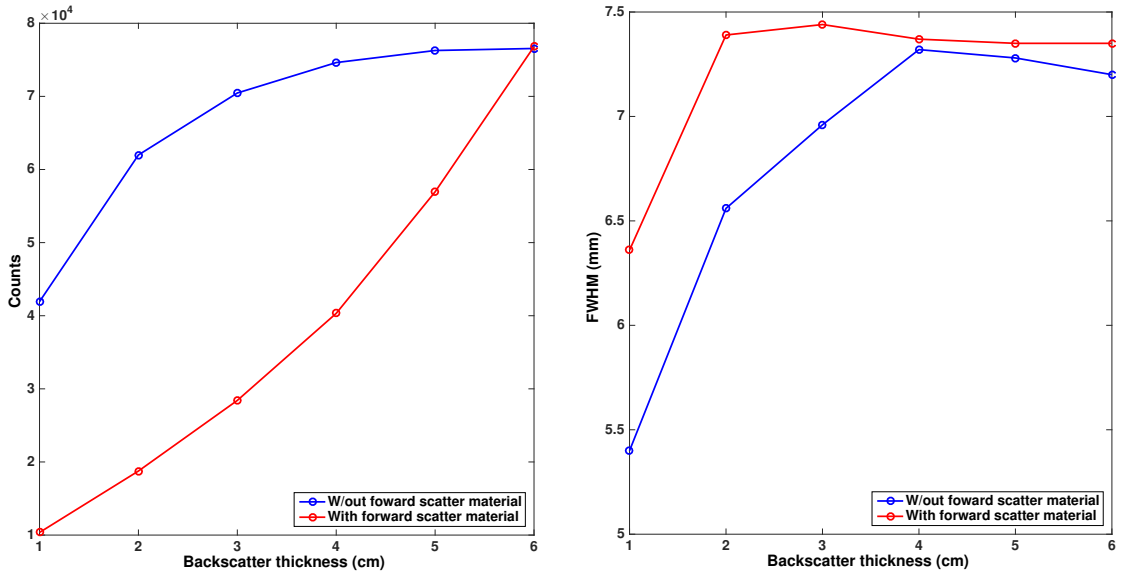

Figure 5.6: Total backscatter counts (with and without forward scatter material) as a function of backscatter thickness) within an 11 % energy window around the backscatter peak energy (Left) and the corresponding FWHM of the summed line profile as a function of backscatter thickness (Right).

counts is 7 % for 6 cm of backscatter material.

Table 5.2: Theoretical number of photopeak and backscatter photons.

Backscatter thickness (cm)	Forward scatter thickness (cm)	Number of photopeak photons ($\times 10^5$)	Number of backscatter photons ($\times 10^5$)	Theoretical Gain (%)
1	5	2.39	0.10	4.2
2	4	3.25	0.19	5.8
3	3	4.42	0.28	6.3
4	2	5.93	0.40	6.7
5	1	7.70	0.57	7.4
6	0	10.51	0.77	7.3

In a simulation study, the photons can be separated based on the number of interactions and their energy information. However, in normal imaging, the acquired data are limited to the energy deposited in the detector. Therefore, the TEW method investigated is only capable of discriminating photons based on energy. In the presence of forward scattering material, a multiple Compton scatter could potentially deposit

energy into the gamma camera with energy equivalent to the backscatter peak. Provided that the TEW method is able to extract the backscatter photons while minimizing multiple Compton scatters, the count sensitivity could potentially increase by 4-7 %. The true backsatter photons were used as a baseline comparison for the backscatter photons estimated from the TEW method.

5.3 TEW Estimated Backscatter Photons

Scattered photons contribute to image degradation and can not be separated out in a normal imaging study. To compensate for the scattered photons, the scatter contribution from the TEW method was estimated by defining two subwindows (W_L and W_R) abutted to the backscatter peak with window width (W_m), one located above and the other below. To reiterate from Chapter 2, the backscatter counts using the TEW method is given by Eq. 2.8, where the C_M, C_L and C_R correspond to the counts in the main window and the left and right subwindows respectively. The total number of counts in the scatter windows were scaled to the main window width and subtracted from the total counts in the main window to obtain the scatter compensated counts, C_P.

In MBI, a photopeak window of 20%($\pm$10%) around the 140 keV peak is generally accepted to ensure that all primary photons are included for a system resolution of 7% at 140 keV. A small proportion of scattered photons are included in this window but can be compensated by using the dual energy or triple energy window scatter correction. Recall from Eq. 2.8, the TEW method approaches the dual energy window approximation as the upper scatter window tends to zero. To compare the backscatter photon yield to the photopeak, the TEW was simplified to the dual-energy window method by setting the high energy subwindow to zero and applied to the photopeak. A 20 % energy window (126-154 keV) centered at 140 keV with a 3 keV subwindow width, 123-126 keV was used to remove scattered photons from the photopeak [118].

Selection of the appropriate backscatter window width for both primary and scatter windows were important to optimize the scatter estimation. A small main window, W_M would decrease the scatter angle acceptance but would also discard the true backscatter photons limited by the energy resolution of the system. In contrast, a large window width increases the angle acceptance window but also includes a greater proportion of wide angle scatters. For example, if a 20 % energy window is centred at

90.4 keV, photons scattered 60° from the backscatter angle are accepted in the main window versus a 10 % energy window which would accept Compton scatters ±40° from the backscatter angle. Since the scatter portion of the spectrum is very different from the photopeak, the optimal combination of the main window and subwindow widths are required to minimize higher order scatter and wide angle Compton scatters, while maximizing the proportion of true backscatter photons. The main backscatter window widths (W_M) investigated are listed in Table 5.3 centred around 90.4 keV, along with the scatter angle acceptance window. For each W_M, the scatter component was estimated with subwindow widths (W_L and W_R) of 3-6 keV with 1 keV increments.

Table 5.3: TEW parameters

	Energy window (%)	Energy range (keV)	Scatter angle
W_{P2}	18 %	82.3-98.5	±58°
W_{P3}	20 %	85.9-94.9	±42°
W_{P4}	22 %	80.5-100.3	±64°

The TEW method was applied to the Monte Carlo simulated data using the window widths defined above. The number of backscatter photons was determined by subtracting the estimated scatter (from the subwindows) from the total number of counts in the backcatter window on a pixel by pixel basis. For each set of simulations with increasing backscatter thickness, the amount of forward scatter material increased proportionately to maintain the simulated average thickness.

Fig. 5.7 summarizes the total number of backcatter counts estimated by the TEW method using different sub-window widths determined from the simulated data for W_M=18 %, 20 % and 22 % windows centred at 90.4 keV compared to the true number of backscatter photons with an 11% energy window. For W_M=18 % (Fig. 5.7a), the TEW method overestimated the scatter contribution and was unable to recover enough of the backscatter photons for all subwindow widths and backscatter thicknesses except for the condition with 1 cm of backscatter material. On the other hand, a W_M=22 % was deemed too large due to an underestimation of scatter, resulting in a larger number of backscatter counts than expected (Fig. 5.7c), except for a backscatter thickness equal to 5 and 6 cm. Using W_M=20 % (Fig. 5.7b), the 5 keV subwindow recovered on average 95 % of the true backscatter photons over the full range of backscatter thicknesses. For smaller backscatter thicknesses, there was a general tendency for the TEW method to underestimate the scatter contribution and for larger backscatter thicknesses, the

TEW method tended to overestimate the scatter contribution. The maximum yield of true backscatter photons occurred when the source was located in the centre of the phantom with equal amounts of forward and back scatter material. A W_m=20 % and subwindow width(W_L, W_R) of 5 keV yielded the optimal estimation of backscatter photons.

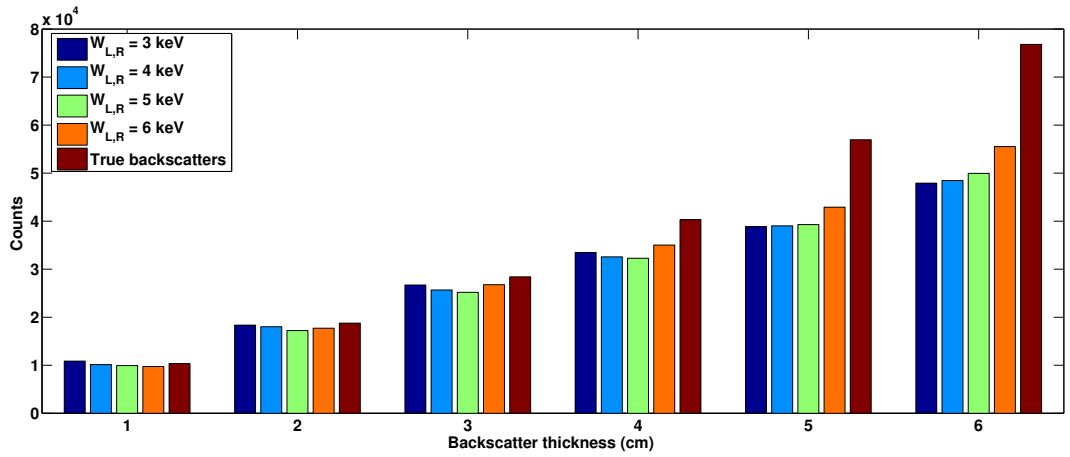

(a) W_m=18%

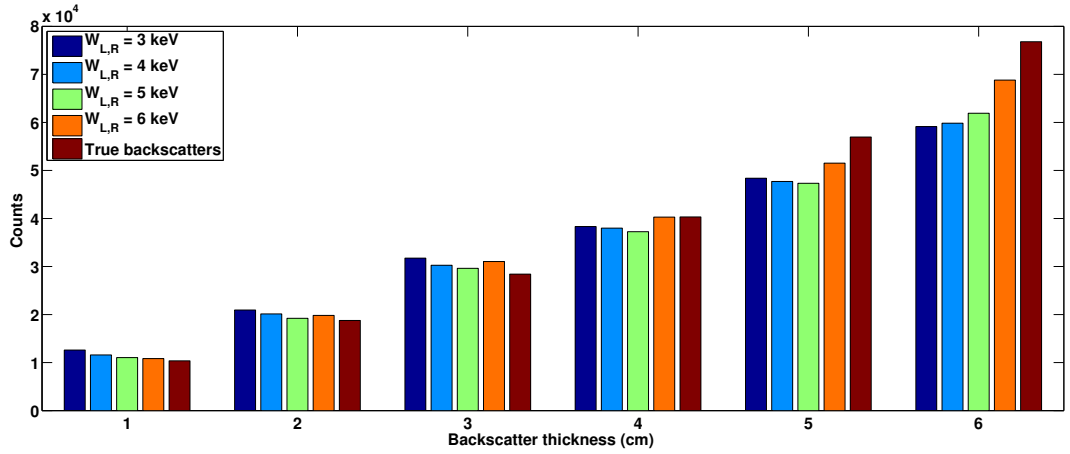

(b) W_m=20%

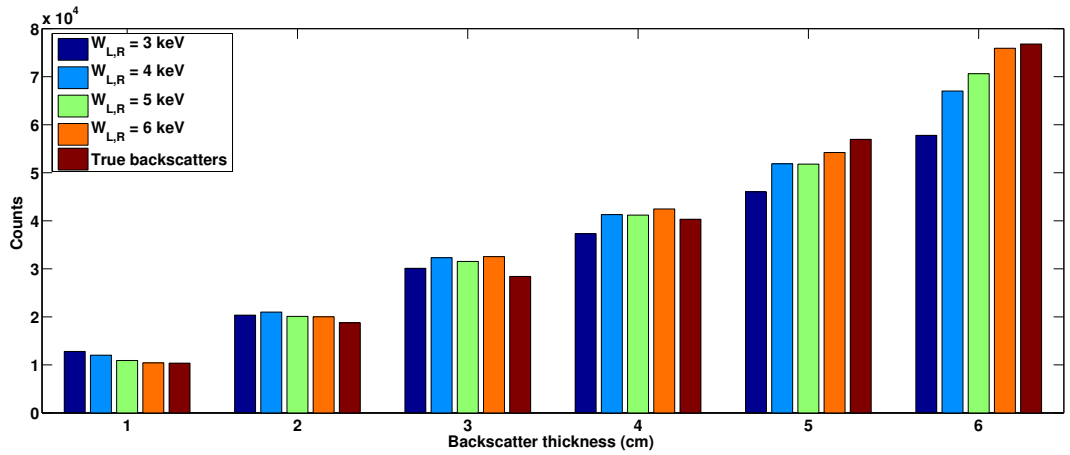

(c) W_m=22%

Figure 5.7: Total number of backscatter photons using the TEW method for a system resolution of 7 % at 140 keV (with window widths W_m, W_L, and W_R) and the true number of backscatters as a function of backscatter material thickness.

5.4 Count sensitivity

The count sensitivity is a measure of how many counts are detected on the gamma camera per unit activity and per unit time. This term factors in the sensitivity of the collimator and gamma camera. To compare the improvement in count sensitivity from the phantom geometry with fixed thickness (6 cm) and backscatter thicknesses ranging from 1 cm to 6 cm, the TEW method was applied to the photopeak and backscatter data with a 20% energy window with 3 keV and 5 keV subwindows to determine the number of scatter compensated photopeak and backscatter counts respectively. The photopeak photons were used as a baseline comparison for evaluating the effect from backscatter photons. For a fixed phantom geometry, the distance from the line source to the collimator decreased as the backscatter thickness increased and the forward scatter material decreased proportionately to maintain the simulated thickness.

The count sensitivity for both the photopeak and backscatter data was determined by taking the scatter corrected counts divided by the total acquisition time (60 secs.) and source activity (45 MBq). Table 5.4 summarizes the increase in count sensitivity from backscatter photons for varying backscatter thicknesses.

Table 5.4: TEW Correlated backscatter count sensitivity

Backscatter thickness (cm)	Photopeak sensitivity (x10^{-5}cps/Bq)	TEW backscatter sensitivity (x10^{-5}cps/Bq)	Measured gain(%)	Theoretical gain(%)
1	9.73	0.41	3.9	4.2
2	12.84	0.71	5.4	5.8
3	17.01	1.10	6.4	6.3
4	22.14	1.38	6.2	6.7
5	27.85	1.75	6.3	7.4
6	37.89	2.29	6.1	7.3

The theoretical gain in backscatter photons is the increase in count sensitivity from the addition of true backscatter to the true photopeak photons, whereas the measured gain is the count sensitivity increase from backscatter photons using the TEW scatter correction method. Since the phantom is fixed with 6 cm positioned at the collimator face, as the backscatter thickness increased, the forward scatter materials decreased by a proportionate amount resulting in increased count sensitivity.

The theoretical gain in count sensitivity from the addition of backscatters was 6-7% and the backscatter count sensitivity increased by 4-6 % for backscatter thicknesses less than 3 cm. Beyond 3 cm, the measured gain from the TEW method plateaued at 6 %. The TEW method was able to match the improvement in count sensitivity as determined by the single Compton scatter analysis for up to 3 cm. At larger backscatter thicknesses, the TEW method overestimated the scatter component by about 10%, resulting in an underestimation of the true backscatter photons.

5.5 Spatial resolution

The spatial resolution of the backscatter peak was expected to be larger than the photopeak due to inclusion of multiple Compton scattered photons and the additional attenuation material between the backscatter interaction and the detector (a backscatter interaction occurs at some distance away from the origin of the source, increasing the distance from the point of interaction to the collimator). The effect of the backscatter photons on the photopeak spatial resolution was determined by comparing the FWHM of the summed profile of the line source for backscatter photons only, photopeak only and the sum from both projections. The summed line profile in Fig. 5.8 shows the increase in backscatter counts relative to backscatter thicknesses ranging from 1 cm-5 cm. The line profile of the backscatter window prior to scatter correction (denoted by the dashed lines in Fig. 5.8) contained a large portion of unwanted scattered photons but the majority were removed through the TEW method. The spatial resolution was determined by fitting the scatter compensated line profile with a Gaussian function for each backscatter thickness.

The relationship between spatial resolution and backscatter thicknesss is summarized for each condition in Table 5.5. The FWHM of the line profile increased by less than 1 mm with the addition of backscatter photons in both the theoretical- and TEW-based scatter correction. The spatial resolution in the backscatter peak was slightly degraded using the TEW method in comparison to the true case because the TEW method underestimated the scatter portion. However, the overall differences were negligible, as the differences in FWHM were less than the intrinsic resolution of the gamma camera (R_{int}= 2.46 mm). The full width at tenth maximum (FWTM) was reported to confirm the spatial distribution of the backscatter photons. The Gaussian function did not factor in the scatter component of the line source when measuring

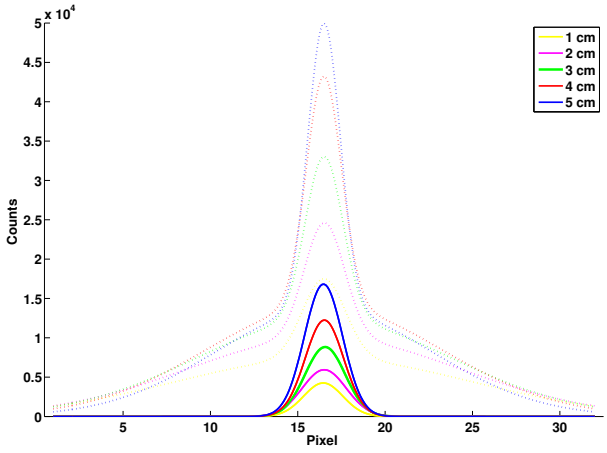

Figure 5.8: Summed line profile of a line source (Counts versus pixel position) for backscatter thicknesses ranging from 1 cm to 5 cm (Dashed lines corresponds to the pre-scatter corrected line profile and solid lines are the scattered corrected backscatter profile).

the FHWM because the spatial distribution is not Gaussian, therefore the FWTM was determined by interpolation of the summed line profile and summarized in Table 5.6. There was no effect on the FWTM in the photopeak and minimal effect on the FWHM when backscatter photons were included which confirmed that there was minimal scatter contribution of photons in the line profile.

Table 5.5: FWHM of photopeak, backscatter and combined line profile.

	FWHM (mm)					
Backscatter thickness (cm)	True backscatter (TB)	True peak (TP)	TB+TP	TEW backscatter (TEW_B)	TEW peak (TEW_P)	TEW_B+ TEW_P
1	6.02	3.38	3.45	5.33	3.61	3.64
2	6.77	3.23	3.35	6.34	3.46	3.54
3	6.72	2.94	3.11	7.1	3.17	3.28
4	6.64	2.64	2.9	6.47	2.79	2.99
5	6.64	2.59	2.89	6.18	2.46	2.77
6	6.63	2.51	2.85	6.17	2.4	2.76

Projection images of the line source in Fig. 5.9 illustrate the spatial distribution for the backscatter window pre- and post-correction for 5 cm backscatter thickness. It is apparent that within the backscatter window, there are photons which contribute the same spatial information as photopeak photons, confirming the use of these spatially

Table 5.6: FWTM of photopeak, backscatter and combined line profile.

	FWTM (mm)					
Backscatter thickness (cm)	True backscatter (TB)	True peak (TP)	TB+TP	TEW backscatter (TEW_B)	TEW peak (TEW_P)	TEW_B+ TEW_P
1	17.04	6.96	6.96	4.08	6.96	6.96
2	21.36	6.96	6.96	23.76	6.96	6.96
3	23.52	6.96	6.96	29.04	6.96	6.96
4	23.28	6.96	6.96	24.11	6.96	6.96
5	23.21	6.96	6.96	20.40	6.96	6.96
6	23.28	6.96	6.96	17.76	6.96	6.96

relevant backscatter photons.

(a) backscatter window (W_{M2} = 83.6-97.1 keV) (b) backscatter window - TEW correction - no correction

(c) scatter corrected photopeak (d) Scatter corrected photopeak + backscatter

Figure 5.9: Comparison of backscatter profiles for 5 cm of backscatter thickness ranging and 1 cm of forward scatter material

The TEW method was able to recover most if not all of the true backscatter photons. Overall, there was less than a 1 mm increase in the FWHM when backscatter photons extracted from the TEW method were added to the photopeak photons indicating the spatial resolution was relatively unaffected for all backscatter thicknesses from Table 5.4. From an additional 4-6 % increase in count sensitivity is possible with the inclusion of backscatter photons using the TEW method, with minimal effect on spatial resolution.

5.6 Contrast to noise ratio

The second portion of the backscatter photon investigation focused on the effect of lesion contrast to noise ratio (CNR). In MBI, two gamma cameras are used to maximize the count sensitivity and minimize the distance from the breast to the camera contributing to decreased image quality. Deeper lesions tend to be more difficult to detect due to the presence of scatter. The average breast thickness when compressed in MBI is approximately 6 cm [138], therefore, the maximum distance from the lesion to the gamma camera is less than 6 cm.

Recall from Eq. 4.9, the contrast to noise ratio was determined by measuring the difference in the mean signal between a lesion (S_L) and the background (S_B) divided by the noise level (σ_B) in the image. In order for a lesion to be considered resolvable, the CNR must meet a threshold requirement of at least 3-5 designated by the Rose criterion [139]. This corresponds to a difference in the mean signal between a lesion and the background exceeding the noise by at least a factor of 3.

The CNR of the simulated lesions (L1-L4 with radii, r=1.5 mm,2.5 mm, 5 mm and 10 mm) with and without backscatter photons are summarized in Table 5.7 for various amounts of forward scatter and backscatter material where 'summed' refers to the lesion CNR for the photopeak plus backscatter photons. For each simulation geometry denoted by S1, S2 and S3, where S1 corresponds to 1 cm of forward scatter/5 cm of backscatter material, S2 corresponds to 3 cm of forward scatter and 3 cm of backscatter material and S3 corresponds to 5 cm of forward scatter and 1 cm of backscatter material. In the S1 and S2 simulations (1 cm and 3 cm of backscatter material, respectively), the CNR of L1 did not satisfy the threshold required by the Rose criterion to be detectable. Overall, CNR decreased by 4-7 % depending on the lesion size. The decrease in CNR was greater for smaller lesions. The contrast increased marginally with the addition of

backscatter photons for all simulations, but noise exceeded the improvement in contrast due to the pixel to pixel fluctuation in the TEW corrected backscatter projection leading to an overall decrease in CNR.

Table 5.7: Contrast to noise ratio of lesions L1-L4 filled with a 20:1 lesion to background activity concentration - Photopeak and summed (photopeak+backscatter).

	S1		S2		S3	
	Photopeak	Summed	Photopeak	Summed	Photopeak	Summed
L1	0.5	0.5	1.4	1.7	4.7	4.4
L2	4.9	4.9	9.8	9.1	22.5	20.4
L3	11.7	11.7	23.1	22.2	47.4	43.2
L4	17.8	17.8	33.3	32.2	63.3	58.3

The projection images for each simulation with the photopeak photons only, the TEW scattered corrected backscatter photons and the summed projections images (photopeak + TEW scatter corrected backscatter) are shown in Fig. 5.10. Upon visual inspection of the TEW backscatter projection image, only L4 was resolvable among all simulations. There were no distinct differences between the photopeak and the summed projection images and L2, L3 and L4 were resolvable in all simulations. L1 was resolvable in only the S3 simulation (5 cm of backscatter material) but approached the limit for lesion detectability.

The count statistics and spatial distribution differ significantly when the TEW method is applied to a photopeak overlapping a scatter spectrum versus an energy window around the backscatter peak from a pure scatter spectrum. Noise in the backscatter projection images is artificially increased due to the TEW method, which is implemented on a pixel by pixel basis. To compensate for this, the backscatter projection image was smoothed with a Gaussian filter ($\sigma = 1$) to minimize any local variation introduced by the TEW method. Fig. 5.11 summarizes the CNR improvement with the filtered backscatter projection image. The Gaussian filter helped to alleviate the artificial noise level in the backscatter projection images. The filtered backscatter photons recovered and even improved CNR by up to 4 % for L2-L4 from the original photopeak data. The CNR for L1 improved by about 30 %, but the absolute value from the photopeak approached the background signal level rendering the L1 lesion still unresolvable even with the backscatter photons. The projection images for S1-S3 using the filtered backscatter photons are shown in Fig. 5.12. Similar to the unfiltered backscatter image, there were still no discernible differences between the photopeak

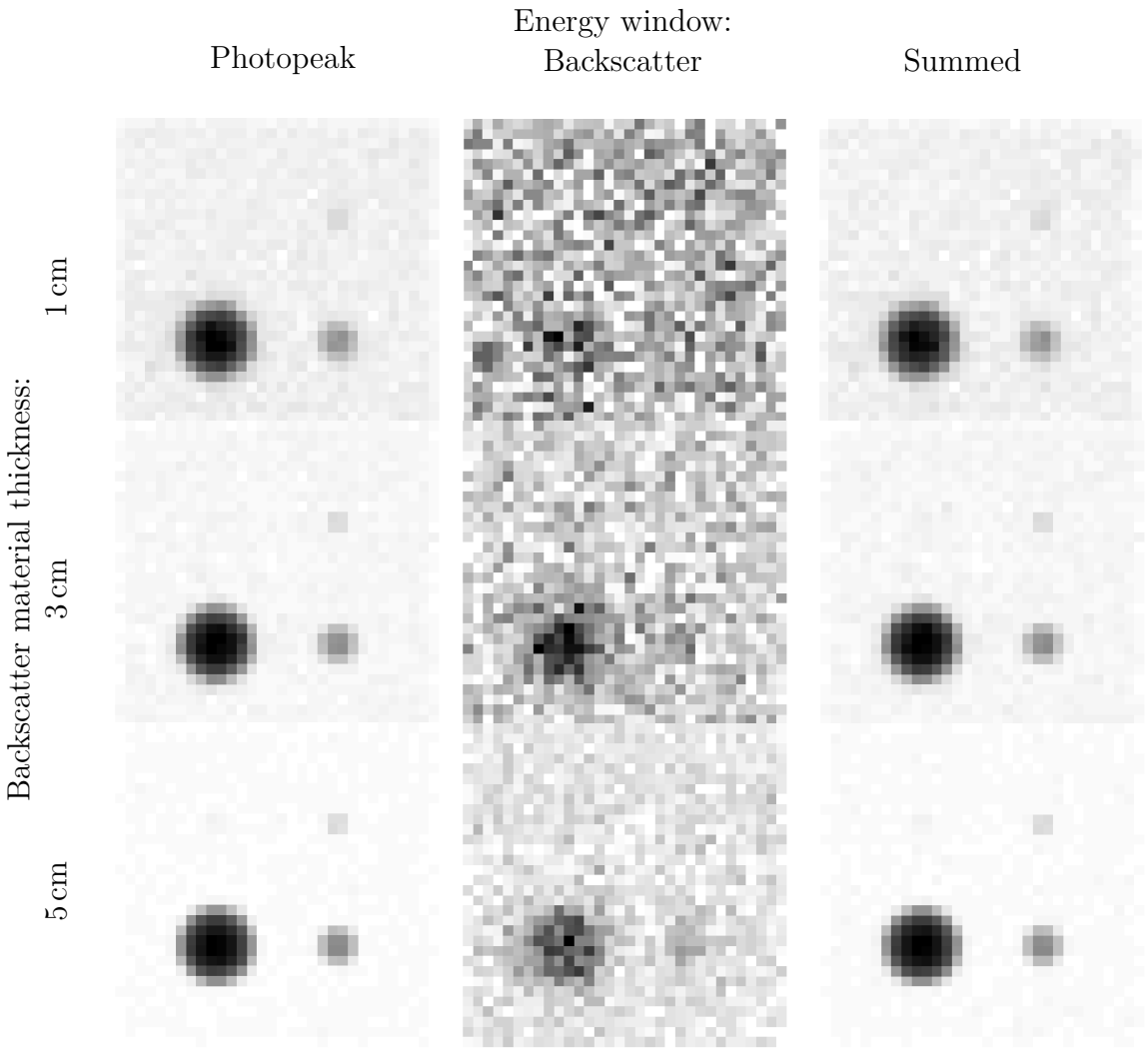

Figure 5.10: Photopeak, backscatter, and the summed projection of the photopeak and backscatter photons for the different lesion configurations.

and the summed projection images. Therefore, the inclusion of the backscatter photons do not degrade nor do they provide any appreciable improvements to the lesion CNR.

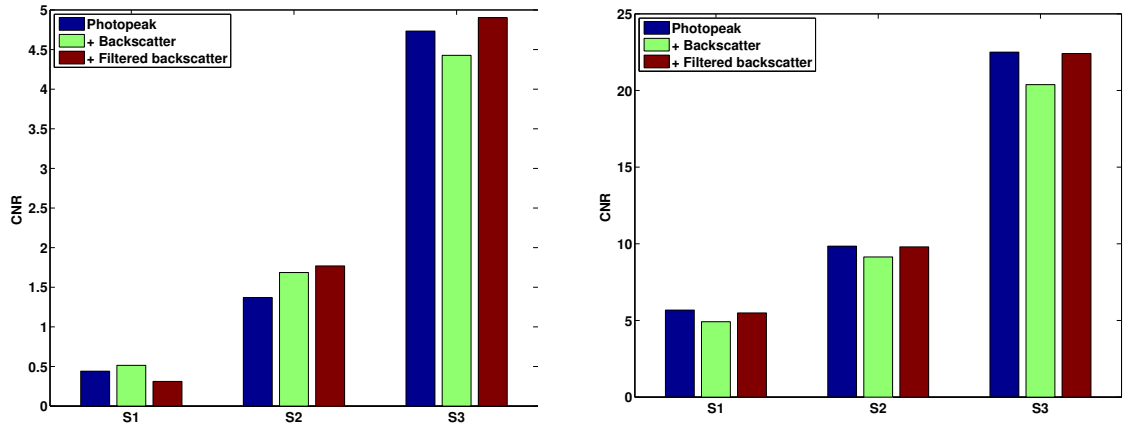

(a) L1 (r=1.5 mm)

(b) L2 (r = 2.5 mm)

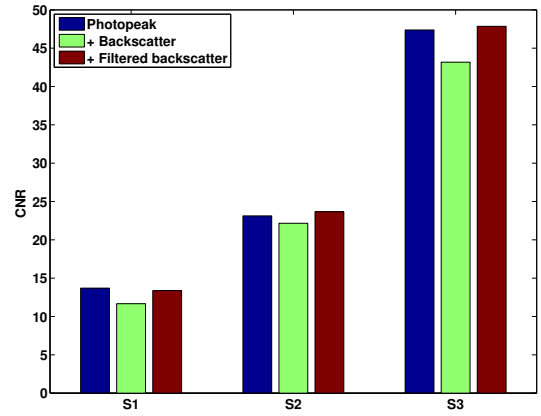

(c) L3 (r=5 mm)

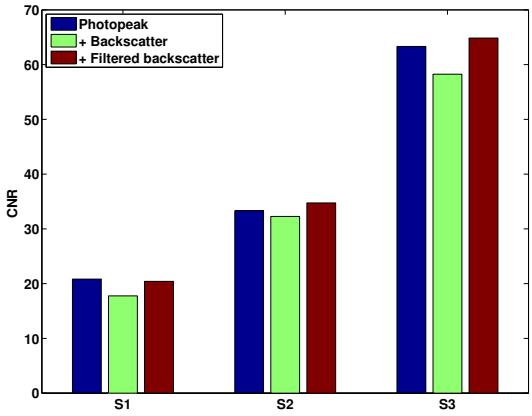

(d) L4 (r=10 mm)

Figure 5.11: Comparison of CNR between the photopeak projection image, with backscatter photons and with filtered backscatter photons for lesions L1-L4 (S1 (1 cm of forward scatter, 5 cm of backscatter material), S2 (3 cm of forward scatter and 3 cm of backscatter material), S3 (5 cm of forward scatter, 1 cm of backscatter material)).

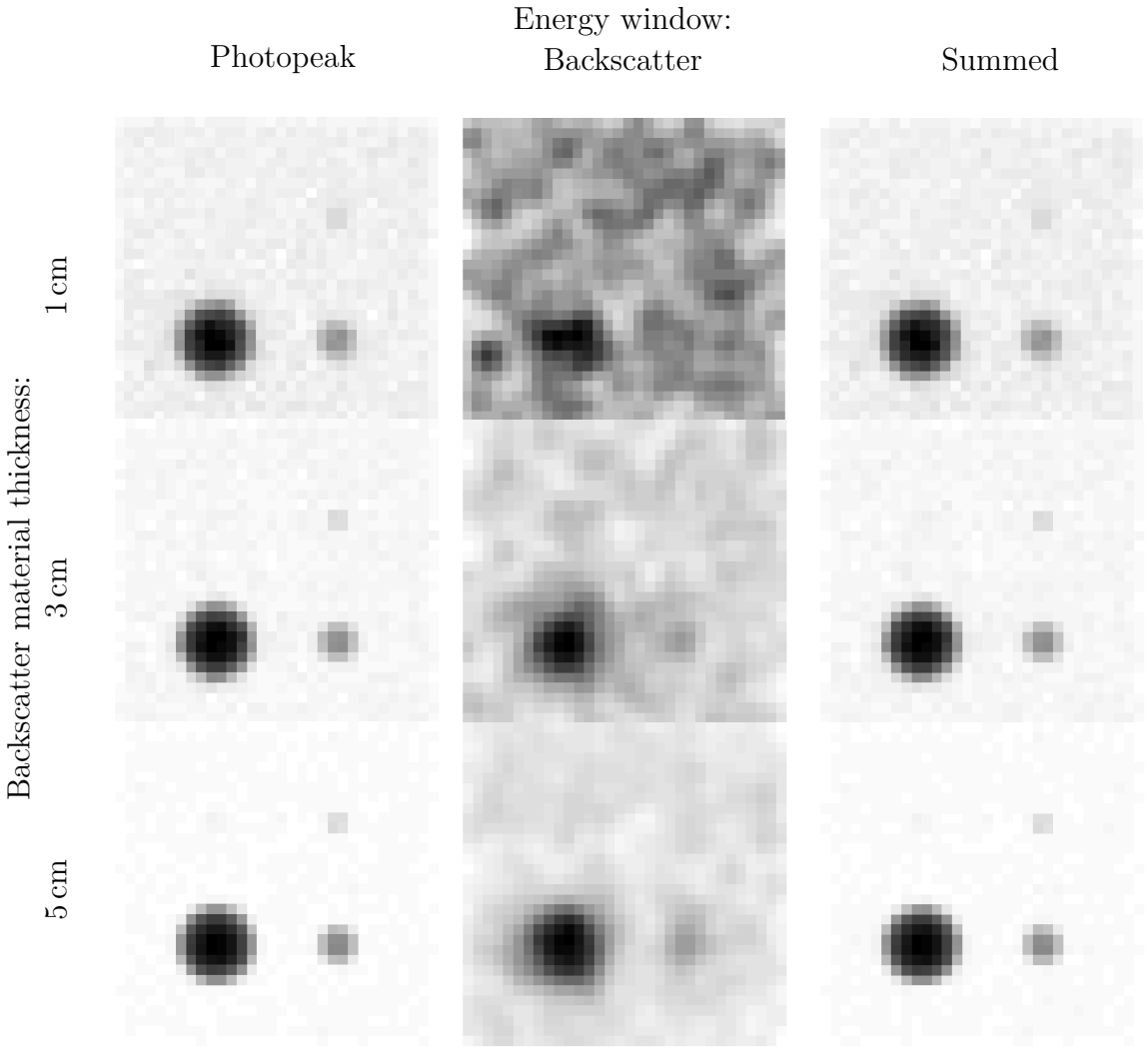

Figure 5.12: Photopeak, filtered backscatter, and the summed projection of the photopeak and filtered backscatter photons for the different lesion configurations.

5.7 Discussion

The TEW method was implemented to estimate the contribution of scattered photons to the backscatter peak using a set of upper and lower subwindows around the main peak window. Previous studies using the triple energy window correction method were applied for dual isotope imaging. The subwindow widths ranged between 1 - 5 keV [118, 140–143]. The primary peak of the lower energy emission is distinct within the scatter spectrum, however, the backscatter photons are contained within the spectrum of scattered photons. Therefore, several window widths had to be investigated to estimate the scatter proportion while retaining as much of the backscatter peak data as possible. The optimized window width to recover an 11 % energy window around 90.4 keV was $W_M = 20\,\%$ with $W_{L,R}= 5$ keV.

The number of true backscatter photons increased as the backscatter thickness increased but plateaued around 5 cm. Larger backscatter thicknesses were not simulated because the average thickness of the breast in MBI is 6 cm, but it is expected that any increase in backscatter photons from an increase in thickness would be offset by additional photon attenuation.

The TEW method was able to recover 80-100 % of all backscatter photons compared to the expected number from single Compton scatter analysis. The phantom geometry affected the ability to recover the backscatter photons because of the presence or lack of forward scattering material. For smaller backscatter thicknesses, the TEW method was unable to remove the larger proportion of multiple Compton scatters, whereas with larger backscatter thicknesses, the TEW method overestimated the scatter contribution. There were no combinations of main and subwindow widths that were able to fully recover larger backscatter thicknesses. Backscatter photon recovery was optimal in the presence of equal forward and backscatter thickness and there was a marked increase in count sensitivity (by up to 6 %) for the same geometry.

Despite inclusion of wide angle Compton scatters, the spatial resolution was not significantly affected, likely due to the subtraction of most multiple Compton scatters using the TEW method. Residual wide angle scatters post-TEW method contributed to spatial degradation but no appreciable effect was observed because there was a higher probability of interaction closer to the source origin due to photon attenuation. This was observed with a minimal increase in the FWHM from the backscatter photons and no change in the FWTM. In both the true and TEW estimated backscatter

photons, the overall spatial resolution (FWHM) increased by less than 1 mm and this effect was deemed negligible.

The TEW scatter correction method is typically used in conjunction with dual isotope imaging, where the proportion of counts in the lower energy photopeak is greater than the scattered photons. However, since the count levels of the backscatter photons are similar to the rest of the scatter spectrum, the TEW method was more susceptible to noise in the scatter estimates on a pixel to pixel basis. Therefore, the use of a Gaussian filter was necessary for noise suppression in the TEW projection image. For all lesions, the TEW method using Gaussian smoothing was able to recover the CNR from the increased noise in the unfiltered image and contrast increased marginally when added to the photopeak data.

Chapter 6

Conclusion

This thesis investigated two techniques to increase the use of molecular breast imaging. First, a solid-state scintigraphic imaging system was designed and built for simultaneous molecular/MR breast imaging. The system was designed to be small enough to fit within the bore of a 3 T MRI, is magnetically safe and does not currently require any alterations to the existing MR hardware system. While the current detector area does not yet match the imaging area of a clinical MBI system, the system design allows for scaling of multiple modules together into a larger area array with minimal spacing between modules.

Secondly, the TEW method, a software based scatter compensation strategy was used to investigate the inclusion of backscatter photons that are typically discarded as a potential dose reduction technique. This method improved count sensitivity up to 6 % while preserving spatial resolution but the effect on CNR from various thicknesses of backscatter material ranged from -3 to 4 % from the photopeak CNR. Overall, there is insufficient evidence to support dose reduction. These backscatter photons contain the same spatial information as photopeak photons as evidenced in the spatial resolution with no significant degradation in CNR and extracting backscatter photons from the Compton scattering spectrum is feasible using the TEW method but no significant advantage was indicated. The following addresses some of the future plans to further optimize these techniques investigated for molecular breast imaging.

6.1 Future Work

In the dual-modality imaging investigation, no geometric distortions were evident in either the MR or gamma camera projection images, however SNR was degraded significantly in the former images. While the presence of the gamma camera in the MRI bore presented with decreased SNR, the specific process of acquiring events in EDR mode increased the count-rate dependent noise level rendering the phantom nearly unresolvable in the MR images. Future work should involve further investigation of potential solutions to improve SNR through changes to the detector module (e.g., different operating clock speed) or increased RF shielding of the detector to suppress the significant RF noise contaminating the MR signal.

In terms of the gamma camera performance, the next step would be to quantify the count sensitivity of the system. The count sensitivity is a key parameter in the performance of the gamma camera and the collimator properties is one of the leading

factors affecting the count sensitivity. The current gamma camera system uses a parallel hole lead collimator optimized for high resolution imaging with low energy gamma rays as it is inexpensive and a common shielding material using in nuclear medicine. However, a study by Hruska et al. determined that the count sensitivity improved substantially with a matched tungsten collimator [64]. While we would expect count sensitivity to improve with a similar collimator, an investigation of the compatibility between the tungsten collimator and MRI performance must be evaluated. In addition to gamma camera optimization, a more comprehensive quantitative analysis should be performed to quantify the contrast to noise ratio of variable-sized lesions.

From a design perspective, the current breast coils are positioned within a frame that is not ideal for the inclusion of a gamma camera directly adjacent to the breast coils. The gamma camera is also manually positioned which means that registration parameters change between acquisitions performed on different days. A redesign or removal of the frame would allow gamma camera testing in the plane with the least amount of scattering and attenuation and to fix the location of the gamma camera with the respect to coils.

Regarding the backscatter photons, it was hoped that the increase in count sensitivity may lead to improved contrast. The count sensitivity improved but the distribution of the backscatter photons increased the noise level leading to decreased CNR. A Gaussian filter was applied to the backscatter data which helped to recover the CNR but the noise level remained similar to the photopeak data. The results from the use of backscatter photons indicate that while these photons do contribute to improved count sensitivity with contrast preservation, there are insufficient counts to significantly decrease the noise statistics. There may be merit in investigating the TEW method with differing tissue densities because the probability of interaction is approximately proportional to the density of the material. The probability of backscatter was uniform in the entire phantom because it was simulated with uniform density and lesions which may be more dense then surrounding tissue may increase the backscatter yield improving the contrast. Given the marginal increase in CNR with a uniform phantom, improvements in CNR from more dense lesions may contribute to the threshold in terms of whether or not a lesion is considered resolvable. In addition, other scatter compensation methods which are less susceptible to noise such as scatter model based methods could be investigated for extracting the backscatter photons.

6.2 Concluding Remarks

Although the MR images suffered from severe SNR degradation when the gamma camera was actively acquiring data, both systems were seen to operate simultaneously. It is anticipated that the RF interference is rectifiable given the results from previous unrelated studies investigating CZT inside the MRI bore [90, 99]. The imaging performance of the gamma camera essentially remain unchanged with and without the presence of simultaneous 3 T MR imaging. Currently, the gamma camera distorts the magnetic field homogeneity by up to 8 ppm which exceeds the limit required for spectroscopy, but no geometric distortion was observed in either the MR or scintigraphy images which is promising for combined MBI/breast MR imaging.

Planar scintigraphy was once regarded as having poor spatial resolution in comparison to other imaging modalities and lacking in anatomical landmarks. This MR compatible gamma camera addresses the need for complementary information of anatomical structures with the functional uptake with improved spatial resolution using a semiconductor based gamma cameras.

While the intent of the MR-compatible gamma camera insert was designed specifically for breast imaging, the design could be modified for dedicated extremity imaging and/or simultaneous dual-isotope imaging. The ability to combine gamma imaging with a system sensitive to a wide range of gamma energies with MRI creates more opportunities for other imaging applications. For example, this system could be extended for detection of rheumatoid arthritis (RA). Radiography is insufficient for early detection and treatment of RA because the inflammation process begins well before morphological changes. Scintigraphic imaging with radiotracers such as Tc-99m labelled diphosphonates targets areas of bone metabolism and In-111 labelled leukocytes highlights the high uptake in inflammatory regions. The combination of scintigraphy with MRI could better improve the monitoring and localization of RA disease progression/regression.

The optimal yield of backscatter photons using the TEW method required energy an energy window of 20 % at 90.4 keV for W_{M2} and 5 keV abutted subwindows for W_{L2} and W_{R2}. The TEW method was able to recover most if not all of the backscatter photons while maintaining the spatial resolution, but no significant impact on CNR was observed. Therefore the inclusion of backscatter photons do not necessarily degrade but also does not significantly improve image quality. Considering this initial simulation

study was performed with a uniform phantom, a marginal increase in CNR may warrant further investigation of backscatter photons with varying levels of tissue density in lesions versus normal breast tissue to aid in MBI studies.

Bibliography

[1] *Canadian Cancer Statistics - Special topic : Predictions of the future burden of cancer in Canada*. Canadian Cancer Society, 2015. URL: www.cancer.ca (cit. on pp. 2, 8).

[2] L. Humphrey, M. Helfand, K. S. Benjamin, B. K. S. Chan, and S. H. Woolf. "Breast cancer screening: A summary of the evidence for the U.S. Preventive Services Task Force". *Annals of Internal Medicine* 137.5 (2002), pp. 347–367 (cit. on p. 2).

[3] S. Hofvind, B. M. Geller, J. Skelly, and P. M. Vacek. "Sensitivity and specificity of mammographic screening as practised in Vermont and Norway." *The British Journal of Radiology* 85.1020 (2012), pp. 1226–32 (cit. on p. 2).

[4] M. T. Mandelson, N. Oestreicher, P. L. Porter, S. H. Taplin, and E. White. "Breast density as a predictor of mammographic detection: Comparison of interval- and screen-detected cancers". *Journal of the National Cancer Institute* 92.13 (2000), pp. 1081–1087 (cit. on p. 2).

[5] F. Sardanelli et al. "Multicenter comparative multimodality surveillance of women at genetic-familial high risk for breast cancer (HIBCRIT study): interim results". *Radiology* 242.3 (Mar. 2007), pp. 698–715 (cit. on p. 2).

[6] N. F. Boyd et al. "Heritability of Mammographic Density, a Risk Factor for Breast Cancer". *The New England Journal of Medicine* 347.12 (2002), pp. 886–894 (cit. on p. 2).

[7] V. A. McCormack and I. dos Santos Silva. "Breast density and parenchymal patterns as markers of breast cancer risk: a meta-analysis". *Cancer Epidemiology Biomarkers and Prevention Biomarkers Prev* 15.6 (2006), pp. 1159–1169 (cit. on p. 2).

[8] G. Maskarinec, I. Pagano, G. Lurie, L. R. Wilkens, and L. N. Kolonel. "Mammographic density and breast cancer risk: the multiethnic cohort study." *American Journal of Epidemiology* 162.8 (Oct. 2005), pp. 743–52 (cit. on p. 2).

[9] T. M. Kolb, J. Lichy, and J. H. Newhouse. "Comparison of the performance of screening mammography, physical examination, and breast US and evaluation of factors that influence them: an analysis of 27,825 patient evaluations." *Radiology* 225.1 (2002), pp. 165–175 (cit. on p. 2).

[10] R. Z. Bigenwald et al. "Is mammography adequate for screening women with inherited BRCA mutations and low breast density?" *Cancer Epidemiology Biomarkers and Prevention* 17.3 (2008), pp. 706–711 (cit. on p. 2).

[11] C. K. Kuhl. "Mammography, Breast Ultrasound, and Magnetic Resonance Imaging for Surveillance of Women at High Familial Risk for Breast Cancer". *Journal of Clinical Oncology* 23.33 (2005), pp. 8469–8476 (cit. on pp. 2, 13, 19).

[12] M. Kriege et al. "Efficacy of MRI and mammography for breast cancer screening in women with a familial or genetic predisposition." *The New England Journal of Medicine* 351.5 (2004), pp. 427–37 (cit. on pp. 2, 13).

[13] A. I. Hagen, K. A. Kvistad, L. Maehle, M. M. Holmen, H. Aase, B. Styr, A. Vabø, J. Apold, P. Skaane, and P. Møller. "Sensitivity of MRI versus conventional screening in the diagnosis of BRCA-associated breast cancer in a national prospective series". *Breast* 16.4 (2007), pp. 367–374 (cit. on pp. 2, 13).

[14] E. Warner et al. "Surveillance of BRCA1 and BRCA2 Mutation Carriers With Magnetic Resonance Imaging, Ultrasound, Mammography, and Clinical Breast Examination". *The Journal of the American Medical Association* 292.11 (2004), pp. 1317–25 (cit. on pp. 2, 13, 19).

[15] D. Ford, D. F. Easton, D. T. Bishop, S. A. Narod, and D. E. Goldgar. "Risks of cancer in BRCA1-mutation carriers". *The Lancet* 343.8899 (1994), pp. 692–695 (cit. on p. 2).

[16] R. Wooster, G. Bignell, J. Lancaster, S. Swift, S. Seal, N. Collins, S. Gregory, C. Gumbs, and G. Micklem. "Identification of the breast cancer susceptiblity gene BRCA2". *Nature* 378.6559 (1995), pp. 789–792 (cit. on p. 2).

[17] Y. Miki et al. "A strong candidate for the breast and ovarian cancer susceptibility gene BRCA1". *Science* 265.5182 (1994), pp. 66–71 (cit. on p. 2).

[18] C. W. Piccoli. "Contrast-enhanced breast MRI: factors affecting sensitivity and specificity". *European Radiology* 7.S5 (1997), S281–S288 (cit. on pp. 2, 14).

[19] S. G. Orel and M. D. Schnall. "MR imaging of the breast for the detection, diagnosis, and staging of breast cancer." *Radiology* 220.1 (2001), pp. 13–30 (cit. on pp. 2, 14).

[20] M. O'Connor, D. Rhodes, and C. Hruska. "Molecular breast imaging". *Expert Review of Anticancer Therapy* 9.8 (Aug. 2009), pp. 1073–80 (cit. on pp. 3, 13, 16, 20, 25).

[21] D. J. Rhodes, C. B. Hruska, A. L. Conners, C. L. Tortorelli, R. W. Maxwell, K. N. Jones, A. Y. Toledano, and M. K. O'Connor. "Molecular breast imaging at reduced radiation dose for supplemental screening in mammographically dense breasts". *American Journal of Roentgenology* 204.2 (2015), pp. 241–251 (cit. on pp. 3, 20).

[22] *CAR Practice Guidelines and Technical Standards for Breast Imaging and Intervention*. Canadian Association of Radiologists, 2012 (cit. on pp. 3, 8, 12, 14).

[23] B. H. Hasegawa, J. K. Brown, S. C. Blankespoor, T. F. Lang, S. C. Liew, B. M. W. Tsui, and C. Ramanathan. "Object-specific attenuation correction of SPECT with correlated dual-energy X-ray CT". *IEEE Transactions on Nuclear Science* 40.4 (1993), pp. 1242–1252 (cit. on p. 4).

[24] D. W. Townsend, T. Beyer, P. E. Kinahan, T. Brun, R. Roddy, R. Nutt, and L. G. Byars. "The SMART scanner: A combined PET/CT tomograph for clinical oncology". *IEEE Nuclear Science Symposium Conference Record* 2.M5-1 (1998), pp. 1170–1174 (cit. on p. 4).

[25] F. A. Mettler, W. Huda, T. T. Yoshizumi, and M. Mahesh. "Effective doses in radiology and diagnostic nuclear medicine: A catalog." *Radiology* 248.1 (2008), pp. 254–263 (cit. on pp. 5, 8, 16, 18).

[26] R. E. Hendrick. "Radiation doses and cancer risks from breast imaging studies". *Radiology* 257.1 (2010), pp. 246–53 (cit. on pp. 5, 8, 17, 18).

[27] SEER. *Cancer of the Breast (Female) - SEER Stat Fact Sheets*. URL: `http://seer.cancer.gov/statfacts/html/breast.html` (cit. on p. 8).

[28] R. G. Blanks. "Effect of NHS breast screening programme on mortality from breast cancer in England and Wales, 1990-8: comparison of observed with predicted mortality". *BMJ* 321.7262 (Sept. 2000), pp. 665–669 (cit. on p. 8).

[29] C. J. D'Orsi, E. A. Sickles, E. B. Mendelson, and E. A. Morris. *ACR BI-RADS® Atlas, Breast Imaging Reporting and Data System.* Reston, VA: American College of Radiology, 2013 (cit. on p. 9).

[30] F. Sardanelli, G. M. Giuseppetti, P. Panizza, M. Bazzocchi, A. Fausto, G. Simonetti, V. Lattanzio, and A. Del Maschio. "Sensitivity of MRI versus mammography for detecting foci of multifocal, multicentric breast cancer in Fatty and dense breasts using the whole-breast pathologic examination as a gold standard." *American Journal of Roentgenology* 183.4 (Oct. 2004), pp. 1149–57 (cit. on p. 9).

[31] N. F. Boyd, J. W. Byng, R. A. Jong, E. K. Fishell, L. E. Little, A. B. Miller, G. A. Lockwood, D. L. Tritchler, and M. J. Yaffe. "Quantitative classification of mammographic densities and breast cancer risk: results from the Canadian National Breast Screening Study." *Journal of the National Cancer Institute* 87.9 (May 1995), pp. 670–5 (cit. on p. 9).

[32] A. Smith. "The Principles of Contrast Mammography". *Hologic* (2014) (cit. on p. 9).

[33] C. Dromain, C. Balleyguier, S. Muller, M. Mathieu, F. Rochard, P. Opolon, and R. Sigal. "Evaluation of tumour angiogenesis of breast carcinoma using contrast-enhanced digital mammography". *American Journal of Roentgenology* 187.5 (2006), W528–W537 (cit. on p. 9).

[34] M. Jochelson, D. Dershaw, J. Sung, A. Heerdt, C. Thornton, C. Moskowitz, J. Ferrara, and E. Morris. "Bilateral contrast-enhanced dual-energy digital mammography: Feasibility and comparison with conventional digital mammography and MR imaging in women with known breast carcinoma". *Breast Imaging* 266.3 (2013), pp. 743–751 (cit. on p. 9).

[35] F. Diekmann, M. Freyer, S. Diekmann, E. Fallenberg, T. Fischer, U. Bick, and A. Pöllinger. "Evaluation of contrast-enhanced digital mammography". *European Journal of Radiology* 78.1 (2011), pp. 112–121 (cit. on p. 9).

[36] C. Dromain, F. Thibault, F. Diekmann, E. Fallenberg, R. Jong, M. Koomen, E. Hendrick, A. Tardivon, and A. Toledano. "Dual-energy contrast-enhanced digital mammography: Initial clinical results of a multireader, multicase study". *Breast Cancer Research* 14.3 (2012), R94 (cit. on p. 9).

[37] R. Jong, M. Yaffe, M. Skarpathiotakis, R. Shumak, N. Danjoux, A. Gunesekara, and D. Piewes. "Contrast-enhanced digital mammography: Initial clinical experience". *Radiology* 228.3 (2003), pp. 842–850 (cit. on p. 9).

[38] *Tests and Procedures - Mammogram*. 2016. URL: `http://www.mayoclinic.org/tests-procedures/mammogram/multimedia/breast-density-mdash-the-four-levels/img-20008862` (cit. on p. 10).

[39] M. Helvie. "Digital Mammography Imaging: Breast Tomosynthesis and Advanced Applications". *Radiologic Clinics of North America* 48.5 (2015), pp. 917–929 (cit. on p. 9).

[40] T. M. Svahn, N. Houssami, I. Sechopoulos, and S. Mattsson. "Review of radiation dose estimates in digital breast tomosynthesis relative to those in two-view full field digital mammography". *The Breast* 24.2 (2015), pp. 93–99 (cit. on p. 9).

[41] D. Gur, G. S. Abrams, D. M. Chough, M. A. Ganott, C. M. Hakim, R. L. Perrin, G. Y. Rathfon, J. H. Sumkin, M. L. Zuley, and A. I. Bandos. "Digital breast tomosynthesis: Observer performance study". *American Journal of Roentgenology* 193.2 (2009), pp. 586–591 (cit. on p. 10).

[42] H. M. Jeufack, L. Vidarsson, C. Piron, and D. B. Plewes. "Parallel Imaging Performance at 16 Channels Dedicated Breast Coils at 3T". *European Congress of Radiology* C-3263 (2010) (cit. on p. 12).

[43] R. S. Butler, C. Chen, R. Vashi, R. J. Hooley, and L. E. Philpotts. "3.0 Tesla vs 1.5 Tesla breast magnetic resonance imaging in newly diagnosed breast cancer patients." *World Journal of Radiology* 5.8 (2013), pp. 285–94 (cit. on p. 13).

[44] R. Price. "Pulse Sequences and Acquisition Techniques for Breast MRI ACR Breast MRI Accreditation Program". May (2010), pp. 1–9 (cit. on p. 13).

[45] C. Westra, V. Dialani, T. S. Mehta, and R. L. Eisenberg. "Using T2-weighted sequences to more accurately characterize breast masses seen on MRI". *American Journal of Roentgenology* 202.3 (2014), pp. 183–190 (cit. on p. 13).

[46] C. Kuhl, P. Mielcareck, S. Klaschik, C. Leutner, E. Wardelmann, J. Gieseke, and H. Schild. "Dynamic breast MR imaging: Are signal intensity time course data useful for differential diagnosis of enhancing lesions?" *Radiology* 211.1 (1999), pp. 101–110 (cit. on pp. 13, 14).

[47] D. Saslow et al. "American Cancer Society Guidelines for Breast Screening with MRI as an Adjunct to Mammography". *CA: A Cancer Journal for Clinicians* 57.2 (2007), pp. 75–89 (cit. on pp. 13, 14).

[48] M. O. Leach et al. "Screening with magnetic resonance imaging and mammography of a UK population at high familial risk of breast cancer: A prospective multicentre cohort study (MARIBS)". *Lancet* 365.9473 (2005), pp. 1769–1778 (cit. on p. 13).

[49] P. C. Stomper, J. S. Winston, S. Herman, D. L. Klippenstein, M. A. Arredondo, and L. E. Blumenson. "Angiogenesis and dynamic MR imaging gadolinium enhancement of malignant and benign breast lesions." *Breast cancer research and treatment* 45.1 (1997), pp. 39–46 (cit. on p. 14).

[50] M. Benndorf, P. A. T. Baltzer, T. Vag, M. Gajda, I. B. Runnebaum, and W. A. Kaiser. "Breast MRI as an adjunct to mammography: Dose it really suffer from low specificity? A retrospective analysis stratified by mammographic BI-RADS classes". *Acta Radiologica* 51.7 (2010), pp. 715–721 (cit. on p. 14).

[51] W. Huang, P. R. Fisher, K. Dulaimy, L. A. Tudorica, B. O'Hea, and T. M. Button. "Detection of breast malignancy: Diagnostic MR protocol for improved specificity." *Radiology* 232.2 (2004), pp. 585–591 (cit. on p. 14).

[52] P. A. T. Baltzer, M. Benndorf, M. Dietzel, M. Gajda, I. B. Runnebaum, and W. A. Kaiser. "False-positive findings at contrast-enhanced breast MRI: A BI-RADS descriptor study". *American Journal of Roentgenology* 194.6 (2010), pp. 1658–1663 (cit. on p. 14).

[53] K. Glunde, Z. M. Bhujwalla, and S. M. Ronen. "Choline metabolism in malignant transformation". *Nature Reviews: Cancer* 11.12 (2011), pp. 835–848 (cit. on p. 14).

[54] R. Katz-Brull, P. T. Lavin, and R. E. Lenkinski. "Clinical utility of proton magnetic resonance spectroscopy in characterizing breast lesions." *Journal of the National Cancer Institute* 94.16 (2002), pp. 1197–1203 (cit. on p. 14).

[55] L. Bartella, E. A. Morris, D. D. Dershaw, L. Liberman, S. B. Thakur, C. Moskowitz, J. Guido, and W. Huang. "Proton MR spectroscopy with choline peak as malignancy marker improves positive predictive value for breast cancer diagnosis: preliminary study." *Radiology* 239.3 (2006), pp. 686–692 (cit. on p. 14).

[56] C. M. Sutherland, R. J. Campeau, and K. A. Kronemer. "Concordant uptake of Tc-99m sestamibi and Tl-201 in unsuspected breast tumor". *Clinical Nuclear Medicine* 17.12 (1992), pp. 936–7 (cit. on p. 15).

[57] C. Aktolun, H. Bayhan, and M. Kir. "Clinical Experience with Tc-99m MIBI Imaging in Patients with Malignant Tumors Preliminary Results and Comparison with Tl-201". *Clinical Nuclear Medicine* 17.3 (1992), pp. 171–6 (cit. on p. 15).

[58] C. H. Kao, S. J. Wang, and T. J. Liu. "The use of technetium-99m methoxyisobutylisonitrile breast scintigraphy to evaluate palpable breast masses". *European Journal of Nuclear Medicine* 21.5 (1994), pp. 432–6 (cit. on p. 15).

[59] I. Khalkhali, J. A. Cutrone, I. G. Mena, L. E. Diggles, R. J. Venegas, H. I. Vargas, B. L. Jackson, S. Khalkhali, J. F. Moss, and S. R. Klein. "Scintimammography: the complementary role of Tc-99m sestamibi prone breast imaging for the diagnosis of breast carcinoma". *Radiology* 196.2 (1995), pp. 421–6 (cit. on p. 15).

[60] L. I. Delmon-Moingeon, D. Piwnica-Worms, A. D. Van den Abbeele, B. L. Holman, A. Davison, and A. G. Jones. "Uptake of the cation hexakis(2-methoxyisobutylisonitrile)-technetium-99m by human carcinoma cell lines in vitro." *Cancer Research* 50.7 (1990), pp. 2198–202 (cit. on p. 15).

[61] D. Piwnica-Worms, J. F. Kronauge, and M. L. Chiu. "Uptake and retention of hexakis (2-methoxyisobutyl isonitrile) technetium(I) in cultured chick myocardial cells. Mitochondrial and plasma membrane potential dependence." *Circulation* 82.5 (1990), pp. 1826–38 (cit. on p. 15).

[62] N. Weidner, J. P. Semple, W. R. Welch, and J. Folkman. "Tumor Angiogenesis and Metastasis - Correlation in Invasive Breast Carcinoma". *The New England Journal of Medicine* 324.1 (1991), pp. 1–8 (cit. on p. 15).

[63] B. Hesse et al. "EANM/ESC procedural guidelines for myocardial perfusion imaging in nuclear cardiology". *European Journal of Nuclear Medicine and Molecular Imaging* 32.7 (2005), pp. 855–897 (cit. on p. 16).

[64] C. B. Hruska, A. L. Weinmann, and M. K. O'Connor. "Proof of concept for low-dose molecular breast imaging with a dual-head CZT gamma camera. Part I. Evaluation in phantoms." *Medical Physics* 39.6 (2012), pp. 3466–75 (cit. on pp. 17, 18, 20, 89, 111).

[65] *Nuclear Medicine Breast Imaging (Scintimammography)*. 2016. URL: `http://www.imaginis.com/nuclear-medicine/nuclear-medicine-breast-imaging-scintimammography` (cit. on p. 17).

[66] *Research: BSGI tracks down hidden cancers*. URL: `http://medicalphysicsweb.org/cws/article/research/36965` (cit. on p. 17).

[67] *Discovery NM750b*. 2016. URL: `http://www3.gehealthcare.com` (cit. on p. 17).

[68] R. E. Hendrick. *Breast MRI: Fundamentals and technical aspects*. New York, NY: Springer, 2008 (cit. on p. 18).

[69] B. Huang, M. W. M. Law, and P. Khong. "Whole-Body PET/CT Scanning: Estimation of Radiation Dose and Cancer Risk". *Radiology* 251.1 (2009), pp. 166–174 (cit. on p. 18).

[70] N. Prionas, S. Aminololama-Shakeri, K. Yang, S. Martinez, K. Lindfors, and J. M. Boone. "Contrast-enhanced dedicated breast CT detection of invasive breast cancer preceding mammographic diagnosis". *Radiology Case Reports* 10.2 (2015), pp. 1–4 (cit. on p. 18).

[71] N. Prionas, K. Lindfors, S. Ray, S. Huang, L. Beckett, W. Monsky, and J. Boone. "Contrast-enhanced Dedicated Breast CT: Initial Clinical Experience". *Radiology* 256.3 (2010), pp. 714–723 (cit. on p. 18).

[72] A. Connell, D. Conover, Y. Zhang, P. Seifert, W. Logan-Young, C. Lin, L. Sahler, and R. Ning. "Cone-Beam CT for Breast Imaging: Radiation Dose, Breast Coverage, and Breast Coverage". *American Journal of Roentgenology: Women's Imaging* 195.2 (2010), pp. 496–509 (cit. on p. 18).

[73] K. Lindfors, J. Boone, T. Nelson, K. Yang, A. Kwan, and D. F. Miller. "Dedicated Breast CT: Initial Clinical Experience". *Radiology* 246.3 (2008), pp. 725–733 (cit. on p. 18).

[74] Y. Davoudi, B. Borhani, M. P. Rad, and N. Matin. "The Role of Doppler Sonography in Distinguishing Malignant from Benign Breast Lesions". *Journal of Medical Ultrasound* 22.2 (2014), pp. 92–95 (cit. on p. 19).

[75] W. T. Yang, J. Chang, and C. Metreweli. "Patients with Breast Cancer: Differences in Color Doppler Flow and Gray-Scale US Features of Benign and Malignant Axillary Lymph Nodes1". *Radiology* 215.2 (2000), pp. 568–573 (cit. on p. 19).

[76] P. Burns, M. Halliwell, P. Wells, and A. Webb. "Ultrasonic Doppler studies of the breast". *Ultrasound in Medicine & Biology* 8.2 (1982), pp. 127–143 (cit. on p. 19).

[77] D. D. Adler, P. L. Carson, J. M. Rubin, and D. Quinn-Reid. "Doppler ultrasound color flow imaging in the study of breast cancer: Preliminary findings". *Ultrasound in Medicine & Biology* 16.6 (1990), pp. 553–559 (cit. on p. 19).

[78] L. S. J. Sim, J. H. C. L. Hendriks, and S. M. C. Fook-Chong. "Breast ultrasound in women with familial risk of breast cancer". *Annals of the Academy of Medicine Singapore* 33.5 (2004), pp. 600–606 (cit. on p. 19).

[79] M. Podkrajsek, M. Marolt Music, M. Kadivec, J. Zgajnar, N. Besic, A. Pogacnik, and M. Hocevar. "Role of ultrasound in the perioperative staging of patients with breast cancer". *European Radiology* 15.5 (2005), pp. 1044–50 (cit. on p. 19).

[80] W. Teh and A. R. Wilson. "The role of ultrasound in breast cancer screening. A consensus statement by the European Group for Breast Cancer Screening". *European Journal of Cancer* 34.4 (1998), pp. 449–450 (cit. on p. 19).

[81] E. Y. Ng, L. N. Ung, and L. S. Sim. "Statistical analysis of health and malignant breast thermography". *Journal of Medical Engineering and Technology* 25.6 (2001), pp. 253–63 (cit. on p. 19).

[82] A. Bremond, V. Ollier, and E. Drapier-Faure. "Thermography of the breast. Sensitivity, specificity and reproducibility". *Bulletin du Cancer* 75.2 (1988) (cit. on p. 20).

[83] M. Moskowitz, J. Milbrath, P. Gartside, A. Zermeno, and D. Mandel. "Lack of efficacy of thermography as a screening tool for minimal and stage I breast cancer". *The New England Journal of Medicine* 295.5 (1976) (cit. on p. 20).

[84] C. B. Hruska, M. K. O'Connor, and D. A. Collins. "Comparison of small field of view gamma camera systems for scintimammography". *Nuclear Medicine Communications* 26.5 (2005), pp. 441–445 (cit. on p. 20).

[85] B. Mueller, M. K. O'Connor, I. Blevis, D. J. Rhodes, R. Smith, D. a. Collins, and S. W. Phillips. "Evaluation of a small cadmium zinc telluride detector for scintimammography." *Journal of Nuclear Medicine* 44.4 (2003), pp. 602–609 (cit. on p. 20).

[86] M. Stabili, J. Stubbs, and R. Toohey. *Radiation Dose Estimates For Radiopharmaceuticals*. Oak Rdige Institue for Science and Education, 1996 (cit. on p. 20).

[87] C. B. Hruska, A. L. Weinmann, C. M. Tello Skjerseth, E. M. Wagenaar, A. L. Conners, C. L. Tortorelli, R. W. Maxwell, D. J. Rhodes, and M. K. O'Connor. "Proof of concept for low-dose molecular breast imaging with a dual-head CZT gamma camera. Part II. Evaluation in patients". *Medical Physics* 39.6 (2012), p. 3476 (cit. on pp. 20, 25).

[88] O. Golan, T. Menes, L. Hevda, O. Goldray, and E. Even-Sapir. "Molecular breast imaging (MBI). Does it have a complementary role to breast MRI?" *Journal of Nuclear Medicine* 53.S1 (2012), p. 1290 (cit. on p. 21).

[89] G. M. Duarte et al. "Fusion of magnetic resonance and scintimammography images for breast cancer evaluation: a pilot study." *Annals of Surgical Oncology* 14.10 (Oct. 2007), pp. 2903–2910 (cit. on p. 21).

[90] B. M. W. Tsui, J. Xu, A. Rittenbach, S. Chen, A. M. El-Sharkaway, W. A. Edelstein, X. Guo, A. Liu, and J. W. Hugg. "High performance SPECT system for simultaneous SPECT-MR imaging of small animals". *2011 IEEE Nuclear Science Symposium Conference Record* (2011), pp. 3178–3182 (cit. on pp. 21, 112).

[91] B. J. Pichler, M. S. Judenhofer, C. Catana, J. H. Walton, M. Kneilling, R. E. Nutt, S. B. Siegel, C. D. Claussen, and S. R. Cherry. "Performance test of an LSO-APD detector in a 7-T MRI scanner for simultaneous PET/MRI." *Journal of Nuclear Medicine* 47.4 (2006), pp. 639–647 (cit. on p. 21).

[92] K. J. Hong, Y. Choi, J. Kang, W. Hu, J. H. Jung, B. J. Min, Y. H. Chung, and C. Jackson. "Performance evaluation of a PET detector consisting of an LYSO array coupled to a 4 × 4 array of large-size GAPD for MR compatible imaging". *Journal of Instrumentation* 6.12 (2011), E12001–E12001 (cit. on p. 21).

[93] P. Després, E. Izaguirre, S. L. S. Liu, L. Cirignano, H. K. H. Kim, M. Wendland, K. Shah, and B. Hasegawa. "Evaluation of a MR-compatible CZT detector". *2007 IEEE Nuclear Science Symposium Conference Record* 6 (2007), pp. 4324–4326 (cit. on p. 21).

[94] A. Goertzen, G. Stortz, J. Thiessen, D. Bishop, M. S. Khan, P. Kozlowski, F. Retiere, G. Schellenberg, V. Sossi, and C. Thompson. "First results from a high-resolution small animal PET insert for PET/MRI imaging". *European Journal of Nuclear Medicine and Molecular Imaging* 2.S1 (2015), A54 (cit. on p. 21).

[95] D. Meier, D. J. Wagenaar, S. Chen, J. Xu, J. Yu, and B. M. W. Tsui. "A SPECT camera for combined MRI and SPECT for small animals". *Nuclear Instruments and Methods in Physics Research, Section A: Accelerators, Spectrometers, Detectors and Associated Equipment* 652.1 (Oct. 2011), pp. 731–734 (cit. on p. 21).

[96] P. Busca et al. "Experimental Evaluation of a SiPM-Based Scintillation Detector for MR-Compatible SPECT Systems". *IEEE Transactions on Nuclear Science* 62.5 (2015), pp. 2122–2128 (cit. on p. 21).

[97] M. J. Hamamura, S. Ha, W. W. Roeck, L. T. Muftuler, D. J. Wagenaar, D. Meier, B. E. Patt, and O. Nalcioglu. "Development of an MR-compatible SPECT system (MRSPECT) for simultaneous data acquisition." *Physics in Medicine and Biology* 55.6 (2010), pp. 1563–1575 (cit. on pp. 21, 24, 82).

[98] J. Zajicek, J. Jakubek, M. Burian, M. Vobecky, A. Fauler, M. Flederle, and A. Zwerger. "Multimodal imaging with hybrid semiconductor detectors Timepix

for an experimental MRI-SPECT system". *Journal of Instrumentation* 8 (2013) (cit. on p. 21).

[99] M. J. Hamamura, W. W. Roeck, S. Ha, J. Hugg, D. J. Wagenaar, D. Meier, B. E. Patt, and O. Nalcioglu. "Simultaneous in vivo dynamic contrast-enhanced magnetic resonance and scintigraphic imaging." *Physics in Medicine and Biology* 56.4 (2011), N63–N69 (cit. on pp. 21, 112).

[100] H. Chen et al. "Large-volume, high resolution cadmium zinc telluride radiation detectors: Recent developments". *Proceedings of SPIE* 6706 (2007), pp. 1–14 (cit. on p. 23).

[101] W. Li, Y. Du, B. D. Yanoff, and J. S. Gordon. "Impact of temperature variation on the energy resolution of 3D position sensitive CZT gamma-ray spectrometers" (2007), pp. 1809–1815 (cit. on p. 23).

[102] G. Mæhlum, K. I. Dietzel, D. Meier, M. Szawlowski, B. Sundal, T. Vandehei, D. Wagenaar, and B. E. Patt. "Study of cadmium zinc telluride (CZT) radiation detector modules under moderate and long-term variations of temperature and humidity". *IEEE Nuclear Science Symposium Conference Record* 2 (2007), pp. 1645–1648 (cit. on p. 23).

[103] S. Cherry, J. Sorenson, and M. Phelps. *Physics in Nuclear Medicine*. 4th. Philadelphia: Elsevier Saunders, 2012 (cit. on p. 23).

[104] M. N. Wernick and J. N. Aarsvold. *Emission Tomography: The Fundamentals of PET and SPECT*. London: Elsevier Academic Press, 2007 (cit. on p. 23).

[105] P. Després, T. Funk, K. S. Shah, and B. H. Hasegawa. "Monte Carlo simulations of compact gamma cameras based on avalanche photodiodes." *Physics in Medicine and Biology* 52.11 (2007), pp. 3057–3074 (cit. on pp. 24, 79).

[106] J. W. Tan, L. Cai, and L. J. Meng. "Experimental study of the response of CZT and CdTe detectors of various thicknesses in strong magnetic field". *Nuclear Instruments and Methods in Physics Research, Section A: Accelerators, Spectrometers, Detectors and Associated Equipment* 652.1 (2011), pp. 153–157 (cit. on p. 24).

[107] P. M. Düppenbecker, J. Wehner, W. Renz, S. Lodomez, D. Truhn, P. K. Marsden, and V. Schulz. "Gradient transparent RF housing for simultaneous PET/MRI using carbon fiber composites". *IEEE Nuclear Science Symposium Conference Record* (2012), pp. 3478–3480 (cit. on p. 24).

[108] B. J. Peng, Y. Wu, S. R. Cherry, and J. H. Walton. "New shielding configurations for a simultaneous PET/MRI scanner at 7T." *Journal of Magnetic Resonanceesonance* 239 (2014), pp. 50–56 (cit. on p. 24).

[109] D. D. L. Chung. "Electromagnetic interference shielding effectiveness of carbon materials". *Carbon* 39 (2001), pp. 279–285 (cit. on p. 24).

[110] E. F. Jackson, M. J. Bronskill, D. J. Drost, J. Och, W. T. Sobol, and G. D. Clarke. "AAPM Report No. 100 -Acceptance testing and quality assurance procedures for magnetic resonance imaging facilities" (2010) (cit. on pp. 25, 63).

[111] B. C. Towe and A. M. Jacobs. "X-Ray Backscatter Imaging". *IEEE Transactions on Biomedical Engineering* BME-28.9 (1981), pp. 646–654 (cit. on p. 25).

[112] P. Rez, R. Metzger, and K. Mossman. "The Dose from Compton Backscatter Screening". *Radiation Protection Dosimetry* 145.1 (2010), pp. 75–81 (cit. on p. 25).

[113] O. Hupe and U. Ankerhold. "Determination of ambient and personal dose equivalent for personnel and cargo security screening". *Radiation Protection Dosimetry* 121.4 (2006), pp. 429–437 (cit. on p. 25).

[114] D. J. Kadrmas, E. C. Frey, and B. M. Tsui. "Analysis of the reconstructibility and noise properties of scattered photons in 99mTc SPECT." *Physics in Medicine and Biology* 42.12 (1997), pp. 2493–516 (cit. on p. 26).

[115] M. King and T. Farncombe. "An overview of attenuation and scatter correction of planar and SPECT data for dosimetry studies". *Cancer Biotherapy & Radiopharmaceuticals* 18.2 (2003), pp. 181–190 (cit. on p. 30).

[116] H. Zaidi. *Quantitative Analysis in Nuclear Medicine Imaging*. New York, NY: Springer Science + Business Media, 2006 (cit. on pp. 30, 31, 86).

[117] K. Ogawa, Y. Harata, T. Ichihara, A. Kubo, and S. Hashimoto. "A practical method for position-dependent Compton-scatter correction in single photon emission CT". *IEEE Transactions on Medical Imaging* 10.3 (1991), pp. 408–412 (cit. on p. 31).

[118] K. Ogawa. "Simulation study of triple-energy-window scatter correction in combined Tl-201, Tc-99m SPECT." *Annals of Nuclear Medicine* 8.4 (1994), pp. 277–281 (cit. on pp. 31, 94, 107).

[119] H. W. A. M. de Jong, F. J. Beekman, M. Ljungberg, and P. P. van Rijk. "The influence of backscatter material on 99mTc and 201Tl line source responses". *Physics in Medicine and Biology* 44.3 (1999), pp. 665–679 (cit. on p. 32).

[120] R. Crestani. *Redlen Digital Module Specification*. Redlen Technologies Inc., 2010 (cit. on p. 35).

[121] A. K. Gupta, V. Chowdhury, and N. Khandelwal. *Diagnostic Radiology: Recent Advances and Applied Physics in Imaging*. 2nd Ed. New Delhi: JP Medical Ltd., 2013 (cit. on p. 37).

[122] "Coaxial Low Pass Filter". *Mini-Circuits* (2013). URL: `http://www.minicircuits.com/pdfs/BLP-30+.pdf` (cit. on p. 37).

[123] A. Kroll. "Spi4teensy3" (2013). URL: `https://github.com/xxxajk/spi4teensy3` (cit. on p. 39).

[124] *NEMA NU 1-2012: Performance Measurements of Gamma Cameras*. National Electrical Manufacturers Association, 2012 (cit. on p. 56).

[125] C. P. Bernard, G. P. Liney, D. J. Manton, L. W. Turnbull, and C. M. Langton. "Comparison of fat quantification methods: a phantom study at 3.0T." *Journal of Magnetic Resonance Imaging* 27.1 (Jan. 2008), pp. 192–7 (cit. on p. 61).

[126] S. B. Reeder, C. D. Hines, H. Yu, C. A. Mckenzie, and J. H. Brittain. "On The Definition of Fat-Fraction for In Vivo Fat Quantification with Magnetic Resonance Imaging". *17th Meeting of the International Society of Magnetic Resonance in Medicine* 17 (2009), p. 211 (cit. on p. 61).

[127] S. Witoszynskyj, A. Rauscher, J. R. Reichenbach, and M. Barth. "Phase unwrapping of MR images using PhUN–a fast and robust region growing algorithm." *Medical Image Analysis* 13.2 (Apr. 2009), pp. 257–268 (cit. on p. 63).

[128] *NEMA Standards Publication MS 1-2008: Determination of Signal-to-Noise Ratio (SNR) in Diagnostic Magnetic Resonance Imaging*. National Electrical Manufacturers Association, 2008 (cit. on p. 65).

[129] *Redlen Module Evaluation System*. Redlen Technologies Inc., 2011 (cit. on p. 76).

[130] *Redlen M1762 Nuclear Imaging Module*. Redlen Technologies Inc., 2011 (cit. on p. 76).

[131] D. J. Wagenaar, O. Nalcioglu, L. Muftuler, and M. Szawlowski. "Development of MRI-compatible nuclear medicine imaging detectors". *IEEE Nuclear Science Symposium Conference Record* (2006), pp. 1825–1828 (cit. on p. 79).

[132] C. B. Hruska and M. K. O'Connor. "CZT detectors: How important is energy resolution for nuclear breast imaging?" *Physica Medica* 21.S1 (2006), pp. 72–75 (cit. on p. 79).

[133] H. Chen, S. A. Awadalla, J. Mackenzie, R. Redden, G. Bindley, A. E. Bolotnikov, G. S. Camarda, G. Carini, and R. B. James. "Characterization of traveling heater method (THM) grown Cd 0.9Zn0.1Te crystals". *IEEE Transactions on Nuclear Science* 54.4 (2007), pp. 811–816 (cit. on p. 80).

[134] E. Hendrick. *Breast MRI: Fundamentals and Technical Aspects*. New York, NY: Springer Science + Business Media, LLC, 2007 (cit. on p. 81).

[135] G. Fenical. "Rule-of-Thumb for Calculating Aperture Size". *Laird Technologies* (2003) (cit. on p. 82).

[136] S. Jan et al. "GATE: A simulation toolkit for PET and SPECT". *Physics in Medicine and Biology* 49.19 (2004), pp. 4543–61 (cit. on p. 87).

[137] C. B. Hruska and M. K. O'Connor. "Effect of collimator selection on tumor detection for dedicated nuclear breast imaging systems". *IEEE Transactions on Nuclear Science* 53.5 (2006), pp. 2680–2689 (cit. on p. 89).

[138] C. B. Hruska, S. W. Phillips, D. H. Whaley, D. J. Rhodes, and M. K. O'Connor. "Molecular breast imaging: use of a dual-head dedicated gamma camera to detect small breast tumors." *American Journal of Roentgenology* 191.6 (2008), pp. 1805–1815 (cit. on p. 102).

[139] S. R. Cherry. "Multimodality in vivo imaging system: twice the power or double the trouble?" *Annual Review of Biomedical Engineering* 8.1 (2006), pp. 35–62 (cit. on p. 102).

[140] Y. Dewaraja, J. Li, and K. Koral. "Quantitative 131-I SPECT with triple energy window compton scatter correction". *IEEE Transactions on Nuclear Science* 45.6 P2 (1998), pp. 3109–3114 (cit. on p. 107).

[141] A. Asgari, M. Ashoor, M. Sohrabpour, P. Shokrani, and A. Rezaei. "Evaluation of various energy windows at different radionuclides for scatter and attenuation correction in nuclear medicine". *Annals of Nuclear Medicine* 29.4 (2015), pp. 375–383 (cit. on p. 107).

[142] Y. S. Lee, J. S. Kim, K. M. Kim, H.-J. Kim, and S. M. Lim. "Optimal energy window for scatter correction in I-131: GATE simulation study". *2011 IEEE Nuclear Science Symposium Conference Record* (2011), pp. 2753–2755 (cit. on p. 107).

[143] J. T. Yang, K. Yamamoto, N. Sadato, T. Tsuchida, N. Takahashi, N. Hayashi, Y. Yonekura, and Y. Ishii. "Clinical value of triple-energy window scatter correction in simultaneous dual-isotope single-photon emission tomography with 123I-BMIPP and 201TI". *European Journal of Nuclear Medicine* 24.9 (1997), pp. 1099–1106 (cit. on p. 107).

Appendix A

Circuit board design

[1]See Fig. A.1. on page 128. A dual MUX was originally incorporated to control both the RSTB and PWR_OK pin of the modules individually, but the current version only uses the PWR_OK pin, therefore zero-ohm resistors were used to connect the input RSTB pins of the MUX.

The electronic schematic includes both the DRB and power distribution board, therefore the FFC components (Wurth Electronik 687 124 145 22) connecting the two were not included in the schematic. In addition, each CZT module has two sets of connectors denoted by J1 and J2 in the schematic (Samtec TFM-110-02-F-D/SFM-110-T2-F-D) and as seen in the layout of the power distribution board Fig.A.3. The components of the power distribution board are encased within the dashed lines.

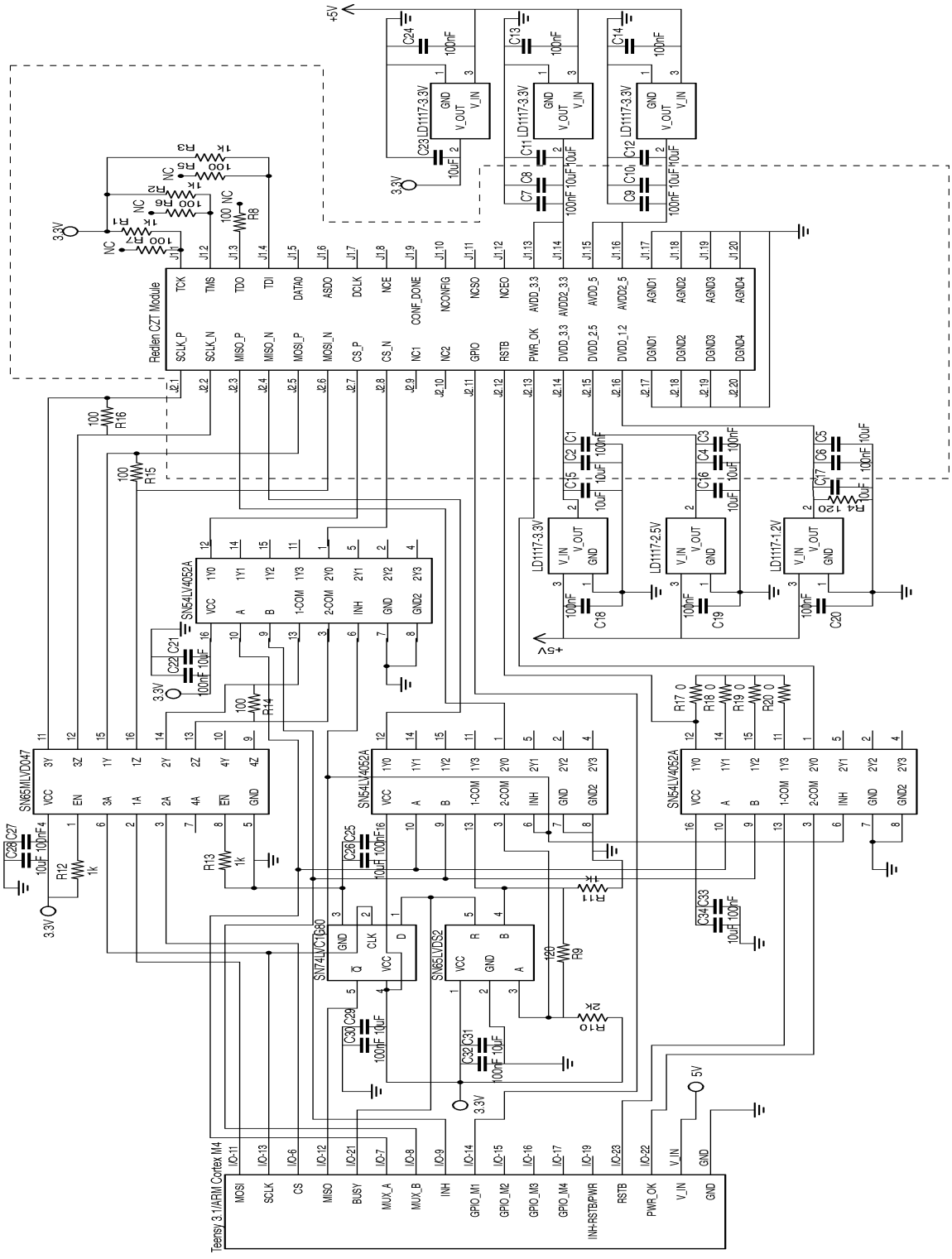

Figure A.1: Electronic schematic of digital readout board[1](Designed in EAGLE - http://www.cadsoftusa.com). Inset: Schematic for the power distribution board.

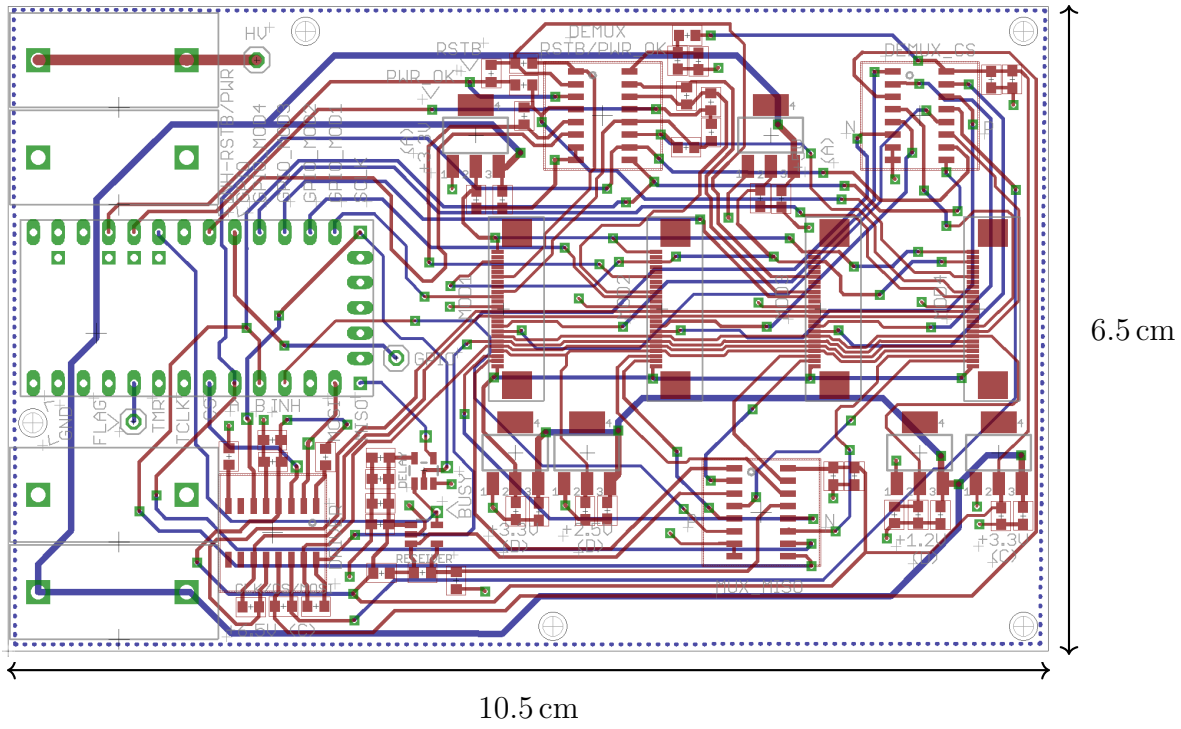

Figure A.2: Digital readout board - Layout (Designed in EAGLE/Printed by OSH Park)

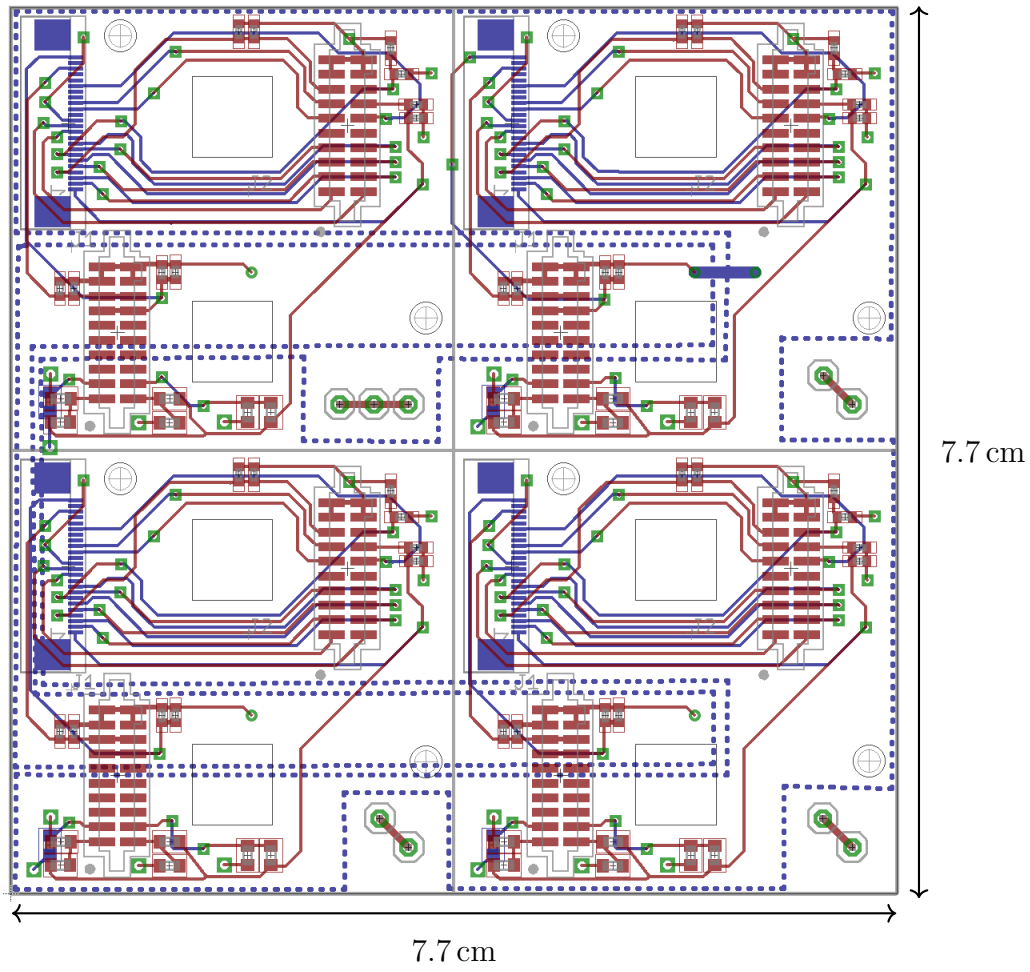

Figure A.3: Power distribution circuit board (Designed in EAGLE/Printed by OSH Park)

Appendix B

RF Shielding

Thickness(Cu), $t = 66\,\mu m$
Frequency, $f = 127,74\,MHz$
Conductivity(Cu), $\sigma = 5.85 \times 10^7\,\Omega^{-1} \cdot m^{-1}$
Permeability of free space, $\mu_0 = 4\pi \times 10^{-7}\,\Omega \cdot m$
Impedance of free space, $\eta_0 = 377\,\Omega$

Overall shielding effectiveness (SE) is the sum of attenuation due to reflection and absorption (Eq. B.1):

$$SE(dB) = 20log\frac{E_{inc}}{E_{trans}} = A(dB) + R(dB) \tag{B.1}$$

Intrinsic impedance of copper at 127.74 MHz: $\eta = \sqrt{\frac{2\pi f\mu}{\sigma}} = 4.15^{-3}\Omega$

Attenuation due to reflection: $R(dB) = 20\,log\frac{\eta_o}{4\eta}$=87 dB

Skin depth of copper at 127.74 MHz: $\delta = \frac{1}{\sqrt{\pi f\mu_0\sigma}} = 5.82\mu m$
Attenuation due to absorption: $A(dB) = 20log\,e^{t/\delta} \approx 8.7\frac{t}{\delta}$=99 dB

$$\therefore SE = 87\,dB + 99\,dB = 186\,dB \tag{B.2}$$

Appendix C

Source code

Source code C.1: Excerpts from MATLAB source code[1]

```
1
2  % CZT Module/Teensy
3  % Written by: Ashley Tao
4  % Last modified: Feb 6, 2016
5  % Module 1–4 are labelled as 0–3 in this code.
6
7  % Open communication with Teensy 3.1
8  teensy = serial('/dev/cu.usbmodem722711');
9  teensy.BaudRate = 115200;
10 teensy.Terminator = 'LF';
11 teensy.InputBufferSize = 3*1024; %num events in buffer = 1024
12 teensy.Timeout = 30;
13 fopen(teensy);
14 fwrite(teensy, modulemode,'uint8'); %Send mode to CZT module %Send into read/write MRA mode or EDR mode
15
16 %Close communication with Teensy 3.1
17 fclose(teensy);
18 delete(teensy);
19 clear teensy;
20
21     % Write register mode
22     if modulemode == 1
```

[1]MATLAB GUI code not included. Basic EDR, read and write MRA code provided.

```
        Mode_1_Ready = fread(teensy,1,'uint8')
        module_select = input('Enter modules to write to (1—15): ');

        if isempty(module_select) || module_select > 15 || module_select == 0
            module_select = 15;
            fprintf('Invalid module setting — Default module = 15')
        end

        fprintf('Register prefix options: \n0x08 — Module configuration and control registers\n0x0A =
             Individual pixel enable and calibration setting\n0x0E = Pixel priority register\n');
        Input_reg_prefix = input('Enter register prefix (0x##): ','s');
        while isempty(Input_reg_prefix)
            Input_reg_prefix = input('Enter register prefix (0x##): ','s');
        end
        Input_reg_prefix = hex2dec(Input_reg_prefix);

        if (Input_reg_prefix == 10)
            Input_register = input('Enter pixel number (0:255): ');
            while isempty(Input_register)
                Input_register = input('Enter pixel number (0:255): ');
            end
        else
            if (Input_reg_prefix == 8)
                fprintf('Registers:\n0x02 — Serial number\n0x06 — Module firmware version\n0x08 — Module
                     control\n0x09 — GPIO configuration\n0x0A — Temperature monitor\n0x0C — Voltage
                     monitor (3.3V)\n0x0E — Voltage monitor (5V)\n0x13 — FLASH CONTROL\n0x80 — Charge
                     collection reset\n0xC4 — Global threshold setting\n0xC6 — Charge collection channel
                     power setting\n0xC7 — Charge collection global channel configuration (Energy range)\n
                     ');
            elseif (Input_reg_prefix ~=12) || (Input_reg_prefix ==14)
                Input_reg_prefix = 8;
                fprintf('Invalid register prefix: Default set to: Module configuration and control
                     registers\n');
                fprintf('Registers:\n0x08 — Module control\n0x09 — GPIO configuration\n0x13 — FLASH
                     Control\n0x80 — Charge collection reset\n0xC4 — Global threshold setting\n0xC6 —
                     Charge collection channel power setting\n0xC7 — Charge collection global channel
                     configuration (Energy range)\n');
            end

            Input_register = input('Enter register address (0x##): ', 's');
            while isempty(Input_register)
                Input_register = input('Enter register address (0x##): ','s');
            end
            Input_register = hex2dec(Input_register);
        end

        if (Input_register == 19)
            fprintf('Restore CNFG: 0x02\nStore CNFG: 0x01 (Set channel power setting to high!)\n')
        elseif (Input_register == 9)
            fprintf('FIFO not empty: 0 (default)\nFIFO full: 1\nFIFO almost empty: 2\nFIFO almost full: 3\
                 n')
        elseif (Input_register == 128)
```

```
            fprintf('SW_RSTB: 2\n')
        elseif (Input_register == 196)
            fprintf('Threshold: x1.1765\n')
        elseif (Input_register == 198)
            fprintf('Low: 0\nNominal: 1 or 2\nHigh: 3\n')
        elseif (Input_register == 199)
            fprintf('Low energy range: 1\nHigh energy range: 0\n')
        else
        end

        Input_data = input('Enter register data (0x##): ','s');
        while isempty(Input_data)
            Input_data = input('Enter register data (0x##): ','s');
        end
        Input_data = hex2dec(Input_data);

        % Write data to Teensy 3.1
        fwrite(teensy, module_select, 'uint8');
        fwrite(teensy, Input_reg_prefix, 'uint8');
        fwrite(teensy, Input_register, 'uint8');
        fwrite(teensy, Input_data, 'uint8');

        for j=0:3
            if (bitand(bitshift(module_select,-j),1) == 1);
                while (teensy.bytesAvailable <1)
                end
                Register_address =(fscanf(teensy));

                while (teensy.bytesAvailable <1)
                end
                Register_data =(fscanf(teensy));%Check contents of register
                fprintf('Mod %d - Register Address: %s\n',j, Register_address);
                fprintf('Mod %d - Register Data: %s\n',j, Register_data);
                if (Input_register == 196) && (Input_reg_prefix == 8);
                    teensy.BytesAvailable;
                    GlobalThreshold = (fscanf(teensy));
                    fprintf('Global Threshold: %s keV \n', GlobalThreshold(1:3));
                end
            else
                fprintf('Module %d not selected\n\n',j)
            end
        end
    %End of write register mode

    %Write register mode
    elseif modulemode == 2
        Mode_2_Ready = fread(teensy,1,'uint8')
        module_select = input('Enter modules to read from (1-15): '); %% Enter number of modules 0-15

        if isempty(module_select) || module_select > 15 || module_select == 0
            module_select = 15;
            fprintf('Invalid module setting - Default module = 15')
```

```
116         end
117
118         fprintf('Register prefix options: \n0x08 — Module configuration and control registers\n0x0A =
                Individual pixel enable and calibration setting\n0x0C = Direct pixel event data access — READ
                 ONLY\n0x0E = Pixel priority register\n');
119         Input_reg_prefix = input('Enter register prefix (0x##): ','s');
120         while isempty(Input_reg_prefix)
121             Input_reg_prefix = input('Enter register prefix (0x##): ','s');
122         end
123         Input_reg_prefix = hex2dec(Input_reg_prefix);
124
125         if (Input_reg_prefix == 10)
126             Input_register = input('Enter pixel number (0:255): ');
127             while isempty(Input_register)
128                 Input_register = input('Enter pixel number (0:255): ');
129             end
130         else
131             if (Input_reg_prefix == 8)
132                 fprintf('Registers:\n0x02 — Serial number\n0x06 — Module firmware version\n0x08 — Module
                        control\n0x09 — GPIO configuration\n0x0A — Temperature monitor\n0x0C — Voltage
                        monitor (3.3V)\n0x0E — Voltage monitor (5V)\n0x13 — FLASH Control\n0x80 — Charge
                        collection reset\n0xC4 — Global threshold setting\n0xC6 — Charge collection channel
                        power setting\n0xC7 — Charge collection global channel configuration (Energy range)\n
                        ');
133             elseif (Input_reg_prefix ~=12) || (Input_reg_prefix ==14)
134                 Input_reg_prefix = 8;
135                 fprintf('Invalid register prefix: Default set to: Module configuration and control
                        registers\n');
136                 fprintf('Registers:\n0x02 — Serial number\n0x06 — Module firmware version\n0x08 — Module
                        control\n0x09 — GPIO configuration\n0x0A — Temperature monitor\n0x0C — Voltage
                        monitor (3.3V)\n0x0E — Voltage monitor (5V)\n0x13 — FLASH Control\n0x80 — Charge
                        collection reset\n0xC4 — Global threshold setting\n0xC6 — Charge collection channel
                        power setting\n0xC7 — Charge collection global channel configuration (Energy range)\n
                        ');
137             end
138
139             Input_register = input('Enter register address (0x##): ', 's');
140             while isempty(Input_register)
141                 Input_register = input('Enter register address (0x##): ','s');
142             end
143             Input_register = hex2dec(Input_register);
144         end
145
146         % Write data to Teensy 3.1
147         fwrite(teensy, module_select, 'uint8');
148         fwrite(teensy, Input_reg_prefix, 'uint8');
149         fwrite(teensy, Input_register, 'uint8')
150
151         for j=0:3
152             if (bitand(bitshift(module_select,-j),1) == 1);
153                 while (teensy.BytesAvailable < 1)
154                 end
```

```
155             Register_address =(fscanf(teensy));
156             teensy.bytesAvailable;
157             Register_data =(fscanf(teensy));%Check contents of register
158             fprintf('Mod %d — Register Address: %s',j, Register_address);
159             fprintf('Mod %d — Register Data: %s',j, Register_data);
160
161             % Temperature monitor
162             if (Input_register == 10) && (Input_reg_prefix == 8);
163                 teensy.BytesAvailable;
164                 temperature =(fscanf(teensy));
165                 fprintf('Temperature: %s %cC\n', temperature(1:5), char(176));
166
167             % Voltage monitor 1 — 3.3V
168             elseif (Input_register == 12) && (Input_reg_prefix == 8);
169                 teensy.BytesAvailable;
170                 Voltage1 =(fscanf(teensy));
171                 fprintf('Voltage Monitor #1: %s V\n', Voltage1(1:4));
172
173             % Voltage monitor 2 — 5V
174             elseif (Input_register == 14) && (Input_reg_prefix == 8);
175                teensy.BytesAvailable;
176                Voltage2 =(fscanf(teensy));
177                fprintf('Voltage Monitor #2: %s V\n', Voltage2(1:4));
178
179             % Over temp
180             elseif (Input_register == 16) && (Input_reg_prefix == 8);
181                 teensy.BytesAvailable;
182                 Overtemp = (fscanf(teensy));
183                 fprintf('Global Threshold: %s %cC \n', Overtemp(1:5),char(176));
184
185             % Pixel threshold
186             elseif (Input_register == 196) && (Input_reg_prefix == 8);
187                 teensy.BytesAvailable;
188                 GlobalThreshold = (fscanf(teensy));
189                 fprintf('Global Threshold: %s keV \n', GlobalThreshold(1:3));
190
191             % Module serial number
192             elseif (Input_register == 2) && (Input_reg_prefix == 8);
193                 teensy.BytesAvailable;
194                 ModSerialnumber = (fscanf(teensy));
195                 fprintf('Module serial number: %s \n', ModSerialnumber(1:9));
196
197             % Energy window
198             elseif (Input_register == 199) && (Input_reg_prefix == 8);
199                 if str2double(Register_data) == 1
200                     fprintf('Module energy range: 0 — 300 keV\n');
201                 elseif str2double(Register_data) == 0
202                     fprintf('Module energy range: 0 — 750 keV\n');
203                 end
204             end
205
206         else
```

```
207             fprintf('Module %d not selected\n\n',j)
208           end
209
210       end
211       %End of read register mode
212
213   elseif modulemode == 51 %Run C code — See source code B.2
214
215   elseif modulemode == 4 %Turn pixels on/off
216       module_select = input('Enter modules to write to (1—15): ');
217       if isempty(module_select)
218           module_select = 15;
219           fprintf('Invalid module setting — Default module = 15')
220       elseif module_select > 15
221           module_select = 15;
222           fprintf('Invalid module setting — Default module = 15')
223       end
224
225       fwrite(teensy, module_select, 'uint8');
226       pixel_map = zeros(1024,1);
227       pix_on = input('Turn pixel on? (1 — yes, 0 —no) ')
228       fwrite(teensy, pix_on,'uint8');
229       pix_off = input('Turn pixel off? (1 — yes, 0 —no) ')
230       fwrite(teensy, pix_off,'uint8');
231
232       mod0 = zeros(16);
233       mod1 = zeros(16);
234       mod2 = zeros(16);
235       mod3 = zeros(16);
236
237       deadpixelarray = zeros(16);
238       dead_pixel_array = zeros(32);
239       pixelmap = zeros(1024,1);
240       totaldeadpix = zeros(32);
241
242       for k=0:3
243           if (bitand(bitshift(module_select,—k),1) == 1);
244               % Pixels on
245               pixelson = 0:255;
246               length_pixelson = size(pixelson,2)—1;
247
248               if pix_on == 1
249                   fwrite(teensy,length_pixelson,'uint8'); %send length of dead pixel map
250                   fwrite(teensy, pixelson, 'uint8'); %send dead pixel map
251
252                   while teensy.BytesAvailable < 1
253                   end
254                   check_pix = fread(teensy, 1, 'uint8');
255                   check_pix = check_pix+1
256               else
257               end
258
```

```
259                 % Pixels off
260                 deadpixelarray = zeros(16,16);
261 %                 load('........'); %load previous pixel map
262                 mod0 = dead_pixel_map(1:16,1:16);
263                 mod1 = dead_pixel_map(1:16,17:32);
264                 mod2 = dead_pixel_map(17:32,17:32);
265                 mod3 = dead_pixel_map(17:32,1:16);
266 
267                 if k == 0 %Module 0
268                     deadpixelarray = deadpixelarray+mod0;
269                     deadpixelarray(6,16) = 1; %List all pixels to turn off in module 0
270                     totaldeadpix(1:16,1:16) = deadpixelarray;
271 
272                 elseif k == 1 %Module 1
273                     deadpixelarray = deadpixelarray+mod1;
274                     deadpixelarray(6,16) = 1;
275                     totaldeadpix(1:16,17:32) = deadpixelarray;
276 
277                 elseif k == 2 %module 2
278                     deadpixelarray = deadpixelarray+mod2;
279                     deadpixelarray(6,16) = 1;
280                     totaldeadpix(17:32,17:32) = deadpixelarray;
281 
282                 elseif k == 3 %module 3
283                     deadpixelarray = deadpixelarray+mod3;
284                     deadpixelarray(6,16) = 1;
285                     totaldeadpix(17:32,1:16) = deadpixelarray;
286                 end
287 
288                 deadpixels = find(deadpixelarray(:))-1;
289                 length_deadpixels = length(deadpixels)-1;
290 
291                 if pix_off == 1
292                     fwrite(teensy,length_deadpixels,'uint8');
293                     fwrite(teensy, deadpixels, 'uint8');
294                     while teensy.BytesAvailable < 1
295                     end
296                     check_pix = fread(teensy, 1, 'uint8');
297                     check_pix = check_pix +1
298                 else
299                 end
300             else
301                 fprintf('Module %d not selected\n\n',k)
302             end
303         end
304 
305         % Read status for each pixel
306         for mm = 0:3
307             if (bitand(bitshift(module_select,-mm),1) == 1);
308             while teensy.BytesAvailable < 256
309             end
310             pixel_map(((mm*256)+1):((mm+1)*256),1) = fread(teensy, 256, 'uint8');
```

```
            else
            end
        end

        mod_0 = reshape(pixel_map(1:256,1),16,16);
        mod_1 = reshape(pixel_map(257:512,1),16,16);
        mod_2 = reshape(pixel_map(513:768,1),16,16);
        mod_3 = reshape(pixel_map(769:1024,1),16,16);
        dead_pixel_map = [mod_0 mod_1; mod_3 mod_2];
        figure(3);
        imagesc(dead_pixel_map)
        total_off = sum(sum(dead_pixel_map));
        m0 = sum(sum(mod_0))
        m1 = sum(sum(mod_1))
        m2 = sum(sum(mod_2))
        m3 = sum(sum(mod_3))

% Not implemented in this current version.
    elseif modulemode == 5
        while(teensy.BytesAvailable < 1);
        end
        teensy_temp = fscanf(teensy);
        fprintf('Teensy Temperature: %s \n ',teensy_temp);

        while(teensy.BytesAvailable < 1);
        end
        power_status = fscanf(teensy);
        fprintf('power status %s ',power_status);

    elseif modulemode == 6
        pause(1);
        % Software reset modules
    elseif isempty(modulemode)
        flag = 0;
    end

    end
```

Source code C.2: Event readout - readUSB_v3.c

```
//Written by: Troy Farncombe
//Last Modified: Feb 6, 2016 by Ashley Tao

#include <stdio.h>
#include <stdlib.h>
#include <string.h>
#include <stdarg.h>
#include <sys/types.h>
#include <sys/stat.h>
#include <sys/time.h>
#include <fcntl.h>
#include <unistd.h>
```

```
13 #include <errno.h>
14 #include <math.h>
15 #include <pthread.h>
16
17 // One of these must be defined, usually via the Makefile
18 #define MACOSX
19
20 #include <termios.h>
21 #include <sys/select.h>
22 #define PORTTYPE int
23 #define BAUD B115200
24 #define MaxEvents 1024
25
26 // function prototypes
27 PORTTYPE open_port_and_set_baud_or_die(const char *name, long baud);
28 int transmit_bytes(PORTTYPE port, const char *data, int len);
29 int receive_bytes(PORTTYPE port,  char *data, int len);
30 void close_port(PORTTYPE port);
31 void die(const char *format, ...) __attribute__ ((format (printf, 1, 2)));
32 void *GetData(void *);
33 void *ProcessData();
34 void SaveData();
35 int file_exist ();
36
37 struct thread_data{
38     int  thread_id;
39     char *Device;
40     int elements;
41     unsigned int *data;
42     int status;
43 };
44
45 struct ListData{
46     unsigned int Time;
47     unsigned short Pixel;
48     unsigned short Energy;
49 } ;
50
51 int DataReady;
52 long ThreadNbr;
53 unsigned char *BatchOut;
54 int elements, Active, DataHold, Acquire;
55 int NbPixels, NbBins;
56 float AcqTime;
57 float *EnergyScale, *UniformityScale;
58 short int *PixelLUT;
59 struct timeval start, start2;
60 struct ListData AllData[MaxEvents];
61 int currentPosn = 0;
62 FILE *fid;
63
64 int main(int argc, char **argv) {
```

```
65      struct thread_data thread_data_array;
66      PORTTYPE port;
67      pthread_t GetDataThreads, SaveDataThreads, ProcessThreads;
68      pthread_attr_t attr;
69      struct timeval begin, end;
70      long mtime, seconds, useconds;
71      time_t AcqStart;
72      double elapsed=0;
73      int rc, hour, min;
74      int i, j, n, count=0;
75      int size, DataStatus=0;
76      void *status = 0;
77      char DevicePort[200], ByteOut;
78      int *data;
79      int recvd, value, batch, batchtotal, total, total_bytes, bytesneeded;
80      float sec;
81      int AcqTimems;
82      short int elementsSent;
83      unsigned char Timebuffer[4], TimeStr[10];
84      unsigned char BytesToRead[2];
85      unsigned char *buffer;
86      int DoAcq, events;
87      struct tm *ptr;
88      static const char ProgressStr[] = "/-\\|";
89      int iter = 0;
90    char buf1[80], *ByteIn,EnergyMapFilename[200], UniformityMapFilename[200];
91      FILE *fp;
92      int NoEMap = 0, NoUMap=0;
93      char fileout[80];
94
95      if ( (argc < 3) ) {
96          die("Usage: receive_test <comport> <AcqTime> <EnergyMapFilename> <UnformityMapFilename>\n");
97      } else if (argc == 3) {
98          sscanf(argv[1],"%s",DevicePort);
99          sscanf(argv[2],"%f",&AcqTime);
100         NoEMap = 1;
101        NoUMap = 1;
102     } else if (argc == 5) {
103         sscanf(argv[1],"%s",DevicePort);
104         sscanf(argv[2],"%f",&AcqTime);
105         sscanf(argv[3],"%s",EnergyMapFilename);
106         int ret;
107         int ret2;
108         ret = strcmp(EnergyMapFilename,"0");
109         if (ret == 0) {
110             NoEMap = 1;
111         }
112         sscanf(argv[4],"%s",UniformityMapFilename);
113         ret2 = strcmp(UniformityMapFilename,"0");
114         if (ret2 == 0) {
115             NoUMap = 1;
116         }
```

```
117     }
118
119     NbPixels = 1024;
120     NbBins = 2047;
121     // AllData is a 1D vector of NbPixels*NbBins representing the 2D image at each energy
122     //AllData = (double *) calloc(NbEvents*, sizeof(double));
123
124     // EnergyScale is slope and y intercept of linear energy scaling
125     // NewEnergy = EnergyScale[0] * DetectedEnergy + EnergyScale[1];
126     EnergyScale = (float *) calloc(2*NbPixels, sizeof(float));
127     fp = fopen(EnergyMapFilename,"rb");
128     if (NoEMap | (fp == NULL ) )  {
129         printf("No ENERGY mapping file found, using default map.\n");
130         for (i = 0;i< NbPixels;i++) {
131             EnergyScale[i] = 1.0;
132         }
133         } else {
134             fread(EnergyScale,sizeof(float), NbPixels*2, fp);
135             fclose(fp);
136         }
137
138         // UniformityScale is a uniformity map at each detected energy
139         UniformityScale = (float *) calloc(NbPixels*NbBins, sizeof(float));
140         fp = fopen(UniformityMapFilename,"rb");
141         if (NoUMap | ( fp == NULL ) ) {
142             printf("No UNIFORMITY map file found using default map.\n");
143             for (i = 0;i< NbPixels;i++) {
144                 for (j=0;j<NbBins;j++){
145                     UniformityScale[j*NbPixels+i] = 1.0;
146                 }
147             }
148         } else {
149         fread(UniformityScale,sizeof(float), NbPixels*NbBins, fp);
150         fclose(fp);
151     }
152
153     // PixelLUT is a mapping from 0—1023 of detected pixel location from module to a 32x32 pixel space
154     PixelLUT = (short int *) calloc(NbPixels,sizeof(short int));
155     fp = fopen("PixelLUT.dat","rb");
156     if( fp == NULL ) {
157         die("Error while opening the file.\n");
158     }
159     fread(PixelLUT,sizeof(short int), NbPixels, fp);
160     fclose(fp);
161
162     DataReady=0;
163     Active = 0;
164
165     // Get the time
166     time(&AcqStart);
167     ptr = localtime(&AcqStart);
168     strftime(buf1,80,"%X", ptr);
```

```
169     printf("Acquisition started at %s\n",buf1);
170
171     Active = 1;
172     printf("Acquiring for %3.3f seconds.\n", AcqTime);
173     port = open_port_and_set_baud_or_die(DevicePort, BAUD);
174     gettimeofday(&start, NULL);
175
176     // Tell the module to go into Data Read Mode: Send "3"
177     tcflush(port, TCIFLUSH);
178     printf("Setting Data acquisition mode -> ");
179     transmit_bytes(port, "3" , 1);
180     usleep(1000);
181
182     // Read the controller response: Should be "3"
183     ByteIn = calloc(1,sizeof(char));
184     n = receive_bytes(port, ByteIn, 1);
185     if (ByteIn[0] != 3) {
186         die("Wrong mode response sucker!\n");
187     }
188     usleep(1000);
189
190     // Tell the module to collect for a specified time: "0"
191     printf("Setting time mode -> ");
192     transmit_bytes(port,"0",1);
193     usleep(1000);
194
195     // Read the controller response: Should be "0"
196     n = receive_bytes(port, ByteIn, 1);
197     if (ByteIn[0] != 0) {
198        die("Wrong acquisition mode response sucker!\n");
199     }
200     printf("OK\n");
201     usleep(1000);
202
203     // Tell the module how long to collect data in milliseconds: Send a 4 byte integer
204     AcqTimems = (int) (AcqTime * 1000);
205     printf("Setting acquisition time to %d ms -> ", AcqTimems);
206     Timebuffer[0] = (char) ((AcqTimems >> 24) & 0xFF);
207     Timebuffer[1] = (char) ((AcqTimems >> 16) & 0xFF);
208     Timebuffer[2] = (char) ((AcqTimems >> 8) & 0xFF);
209     Timebuffer[3] = (char) (AcqTimems & 0xFF);
210     transmit_bytes(port, Timebuffer, 4);
211     usleep(1000);
212
213     // Read the module response: Should be "9"
214     n = receive_bytes(port, ByteIn, 1);
215     if (ByteIn[0] != 9) {
216         die("Wrong time response sucker!\n");
217     }
218     printf("OK\n");
219     usleep(1000);
220     DoAcq = 1;
```

```
221
222     printf("Opening file\n");
223     char time_string[1000];
224     time_t t = time(NULL);
225     struct tm * p = localtime(&t);
226     strftime(time_string,1000,"%B%d", p);
227     int mm;
228     mm = 0;
229     int file_check;
230     file_check = 0;
231     char buffer_name[50];
232     while (file_check == 0){
233         snprintf(buffer_name,sizeof(char)*32,"ListOut_%s_%d.dat",time_string,mm);
234         if (file_exist (buffer_name)) {
235             mm++;
236             file_check = 0;
237         } else {
238             file_check = 1;
239         }
240     }
241     sprintf(fileout,"ListOut_%s_%d.dat",time_string,mm);
242     fid = fopen(fileout,"w");
243
244     // Now start the acquisition
245     printf("**********************\nStarting Acquisition\n");
246
247     // Repeat this loop to keep reading data.  The module should already be in Data Readout Mode
248     // DoAcq is equal to 1 as long as the module is still sending data. while(DoAcq) {
249     if (DataReady == 0) {                       // Check if I am ready to receive data
250         gettimeofday(&start2, NULL);
251         total_bytes = 0;
252
253         while(total_bytes<1){
254             usleep(10);
255             n = receive_bytes(port, ByteIn, 1);     // Read byte to see if Teensy is ready
256             if (n<0) n = 0;
257             total_bytes = total_bytes + n;
258         }
259
260         transmit_bytes(port, "A", 1);           // Transmit "A" to request data from Teensy
261         total = 0;
262         batch = 0;
263         recvd = 0;
264
265         n = 0;
266         total_bytes = 0;
267     while(total_bytes<2){
268         usleep(10);
269         n = receive_bytes(port, &BytesToRead[total_bytes], 2-total_bytes);      // Read the number of
              events to read
270             if (n<0) n = 0;
271         total_bytes = total_bytes + n;
```

```
272     }
273
274     elements = (unsigned short int) ((BytesToRead[1]<<8)+(BytesToRead[0]));
275     fflush(stdout);
276     BatchOut = (unsigned char* ) calloc(3*(elements+1)*sizeof(char),1);
277     size = elements*3;
278
279      // Determine how many bytes I've already read in this batch, and how many more I still have to read
280      if (3*elements>size) {
281          bytesneeded = size;
282      } else {
283          bytesneeded = 3*elements;
284      }
285     buffer = (unsigned char*) calloc (size,sizeof(char));
286
287     // Read them until I have them all
288     while (total < 3*elements) {
289         n = receive_bytes(port, buffer, bytesneeded);
290         if (n<0) n=0;
291         recvd = n;
292         batch++;
293         total=total+n;
294
295         if ((3*elements-total)<size) {
296              bytesneeded = 3*elements-total;
297              } else {
298                  bytesneeded = size;
299              }
300              for (i=0;i<recvd;i++) {
301                  BatchOut[total-recvd+i+3] = buffer[i];
302                  }
303         }
304
305         // Read the last byte to see whether more data is still coming.
306         n = receive_bytes(port, ByteIn, 1);
307         while (n<1) {
308             usleep(10);
309             n = receive_bytes(port, ByteIn, 1);
310         }
311
312         // If this byte == 1, then keep reading, otherwise, stop.
313         if (ByteIn[0] == 5) {
314             DoAcq = 1;
315         } else {
316             DoAcq = 0;
317         }
318
319         BatchOut[0] = (BytesToRead[0]);
320         BatchOut[1] = (BytesToRead[1]);
321         BatchOut[2] = 0;
322         fflush(stdout);
323
```

```
324         DataReady = 1;
325         // Start a data processing thread
326         rc = pthread_create(&ProcessThreads, NULL, ProcessData, (void*) BatchOut);
327         if (rc){
328             printf("ERROR; return code from pthread_create() is %d\n", rc);
329             exit(-1);
330         }
331 
332         usleep(100);
333         iter++;
334         fflush(stdout);
335         free (buffer);
336         free (BatchOut);
337         } else {
338             usleep(1);
339         }
340     }
341     // Close the port and kill remaining threads.
342     time(&AcqStart);
343     ptr = localtime(&AcqStart);
344     strftime(buf1,80,"%X", ptr);
345     usleep(1000000);
346     printf("\nClosing\n");
347     printf("Acquisition finished at %s\n",buf1);
348     close_port(port);
349     fclose(fid);
350     Active = 0;
351     pthread_exit(NULL);
352 }
353 
354 int file_exist (char *filename) {
355     struct stat   buffer;
356     return (stat (filename, &buffer) == 0);
357 }
358 
359 void *ProcessData (void *data) {
360     int ii;
361     int i;
362     unsigned short int pixel, energy, tmp_pixel, datacheck;
363     unsigned int value, events;
364     unsigned char *tempbuffer;
365     struct timeval begin, end;
366     long seconds,useconds, mtime;
367     long seconds2,useconds2, mtime2;
368     double elapsed, speed, TotalElapsed, sum=0.0;
369 
370     gettimeofday(&end, NULL);
371     seconds  = end.tv_sec  - start.tv_sec;
372     useconds = end.tv_usec - start.tv_usec;
373     mtime = ((seconds) * 1000 + useconds/1000.0) + 0.5;
374 
375     seconds2  = end.tv_sec  - start2.tv_sec;
```

```
    useconds2 = end.tv_usec - start2.tv_usec;
    elapsed = (double) ((seconds2) * 1000 + useconds2/1000.0) + 0.5;

    tempbuffer = (unsigned char *) calloc(3*sizeof(char),1);
    memcpy(tempbuffer, data, 3);
    events = (int) ((tempbuffer[2]<<16)+(tempbuffer[1]<<8) + (tempbuffer[0]));
    free(tempbuffer);
    tempbuffer = (unsigned char *) calloc(3*(events+1)*sizeof(char),1);
    memcpy(tempbuffer, data, 3*(events+1)*sizeof(char));

    usleep(1);
    DataReady = 0;
    DataHold = 1;

    for (i=1; i < (events+1); i++) {
        value = (unsigned int) (tempbuffer[3*i]<<16)+(tempbuffer[3*i+1]<<8)+(tempbuffer[3*i+2]);
        tmp_pixel = (unsigned short int) ((((value >> 19) & 0x03)*256) + (value & 0xff));
        pixel = PixelLUT[tmp_pixel];
        energy = (unsigned short int) ((value >> 8) & 0x07FF);
        energy = (unsigned short int)  ((EnergyScale[pixel] * (float) (energy)) + EnergyScale[NbPixels+pixel]);
        datacheck = (unsigned short int) ((value >> 19) & 0x0F);
        if (energy>=NbBins) energy=NbBins-1;

        AllData[i-1].Time = (unsigned long int) mtime;
        AllData[i-1].Pixel = (unsigned short int) pixel;
        AllData[i-1].Energy = (unsigned short int) energy;
        currentPosn++;
    }
   //Append data into list-mode file
   for (i=0;i<(events);i++) {
        fwrite(&AllData[i],sizeof(struct ListData),1,fid);
    }

    printf("\b\b\b\b\b\b\b\b\b\b\b\b\b\b\b\b\b\b\b\b\b\b\b\b\b\b\b\b\b\b\b\b\b\b\b\b\b\b\b\b\b\b\b\b\b\b\b\b\b\b\b\b\b\b\b\b\b\bComplete: %2.2f%%  CPS: %6.2lf  Total counts = %d", 100*(float)(mtime/1000.)/AcqTime, (double) events/elapsed*1000.0, currentPosn);
    fflush(stdout);
    DataHold = 0;
    free(tempbuffer);
    pthread_exit(NULL);
}

PORTTYPE open_port_and_set_baud_or_die(const char *name, long baud)
{
        PORTTYPE fd;
        struct termios tinfo;
        fd = open(name, O_RDWR | O_NONBLOCK);

        if (fd < 0) {
        die("unable to open port %s\n", name);
        }
```

```
425         if (tcgetattr(fd, &tinfo) < 0) {
426         die("unable to get serial parms\n");
427         }
428         cfmakeraw(&tinfo);
429         if (cfsetspeed(&tinfo, baud) < 0) {
430             die("error in cfsetspeed\n");
431         }
432         tinfo.c_cflag |= CLOCAL;
433 
434         if (tcsetattr(fd, TCSANOW, &tinfo) < 0) {
435         die("unable to set baud rate\n");
436         }
437         fcntl(fd, F_SETFL, fcntl(fd, F_GETFL));
438         fcntl(fd, F_RDAHEAD, 0);
439         return fd;
440 
441 }
442 
443 int receive_bytes(PORTTYPE port, char *data, int len)
444 {
445     return read(port, data, len);
446 }
447 
448 
449 int transmit_bytes(PORTTYPE port, const char *data, int len)
450 {
451     return write(port, data, len);
452 }
453 
454 int transmit_int32(PORTTYPE port, const int data, int len)
455 {
456     unsigned char byte_data[4];
457     char byte;
458     int i;
459 
460     byte_data[0] = (unsigned char)((data>>24) & (0xff));
461     byte_data[1] = (unsigned char)((data>>16) & (0xff));
462     byte_data[2] = (unsigned char)((data>>8) & (0xff));
463     byte_data[3] = (unsigned char)((data) & (0xff));
464     return write(port, byte_data, len);
465 }
466 
467 void close_port(PORTTYPE port)
468 {
469     close(port);
470 }
471 
472 void die(const char *format, ...)
473 {
474     va_list args;
475         va_start(args, format);
476         vfprintf(stderr, format, args);
```

```
        exit(1);
}
```

Source code C.3: Microcontroller source code

```
//Written by: Ashley Tao
//Last modified Feb 6, 2016
//This microcontroller code communicates with Redlen's CZT modules via five modes: Read register (via MRA)
     , Write register (via MRA), event data readout( via EDR), pixel enable/disable (via MRA), and
     software reset (via MRA).

#include <spi4teensy3.h>
#include <Arduino.h>

//Define variables/pin locations

//Module GPIO/Multiplexer
#define MUX_A 7
#define MUX_B 8
#define INH 9
#define INH_RSTB 19
#define GPIO_MOD1 14
#define GPIO_MOD2 15
#define GPIO_MOD3 16
#define GPIO_MOD4 17
uint8_t gpio_check = 0;

//Master out data
byte Module_mode;
byte input_mod; //switched from uint8_t
uint8_t mod_select;
byte reg_address;
byte reg_data;

byte reg_prefix;
uint8_t mod_trig;
uint8_t gpio_trig;
char tempbuffer[4];

byte *pixel; //= NULL;
byte *pixel_map; // = NULL;
byte valid_regdata;
byte total_pix;

int tempPin = A10;
int tempValue = 0;
float Teensy_temp, Vout;

//Slave out data
uint32_t reg_check;
uint32_t data_return;
uint32_t data_return2;
```

```
uint32_t data_return3;
uint32_t data_return4;
uint32_t *event_data = NULL;
uint32_t BufferSize = 1024;

//indices
uint32_t indx;
uint8_t ii;
uint8_t jj;

//Module chip select
#define CS_MOD 6

//Timer variables
IntervalTimer event_readout_timer; //Create IntervalTimer object
#define DATA_ACQ_TIMER 4 //Timer active low
int timer_counter = 0;
int AcqTime;
int timer_flag;
uint32_t count;
uint32_t remaining_count;

byte power_status;

//Other pin designations
#define RSTB 23
#define PWR_OK 22
#define BUSY_BIT 21

void setup() {
  //GPIO pins idle low
  *portConfigRegister(14) &= ~PORT_PCR_PS;
  *portConfigRegister(15) &= ~PORT_PCR_PS;
  *portConfigRegister(16) &= ~PORT_PCR_PS;
  *portConfigRegister(17) &= ~PORT_PCR_PS;

  //Declare pin INPUT/OUTPUT
  pinMode(tempPin, INPUT);
  pinMode(CS_MOD, OUTPUT);
  pinMode(GPIO_MOD1, INPUT);
  pinMode(GPIO_MOD2, INPUT);
  pinMode(GPIO_MOD3, INPUT);
  pinMode(GPIO_MOD4, INPUT);
  pinMode(PWR_OK, INPUT);
  pinMode(RSTB, OUTPUT);
  pinMode(BUSY_BIT, INPUT);
  pinMode(DATA_ACQ_TIMER, OUTPUT);
  pinMode(MUX_A, OUTPUT);
  pinMode(MUX_B, OUTPUT);
  pinMode(INH, OUTPUT);
  pinMode(INH_RSTB, OUTPUT);

```

```
98    digitalWriteFast(INH, LOW);
99    digitalWriteFast(INH_RSTB, LOW);
100   analogReadResolution(12);
101
102   Serial.begin(115200); // USB is always 12 Mbit/sec
103   spi4teensy3::init(1, SPI4TEENSY3_MODE_1); // full speed, cpol 0, cpha 1
104
105   //Reset all modules
106   digitalWriteFast(RSTB, LOW);
107   delayMicroseconds(1000000);
108   digitalWriteFast(RSTB, HIGH);
109   delayMicroseconds(1000);
110
111   //Wait for power up
112   for (ii = 0; ii < 2; ii++) {
113     for (jj = 0; jj < 2; jj++) {
114       digitalWriteFast(MUX_A, !!ii);
115       digitalWriteFast(MUX_B, !!jj);
116       delayMicroseconds(50);
117
118       power_status = 0;
119       while (!power_status) {
120         power_status = digitalRead(PWR_OK);
121       }
122     }
123   } //end of loop to power on modules
124
125   //Reset all modules
126   for (ii = 0; ii < 2; ii++) {
127     for (jj = 0; jj < 2; jj++) {
128       digitalWriteFast(MUX_A, !!ii);
129       digitalWriteFast(MUX_B, !!jj);
130       delayMicroseconds(50);
131
132       //Write to register
133       spi4teensy3::write_register(CS_MOD, 0x00, 0x01, 0x08); //Module RST
134       delayMicroseconds(10);
135       spi4teensy3::write_register(CS_MOD, 0x08, 0x02, 0x08); //Clear FIFO
136     }
137   } //end of loop to reset all modules
138 } //end of setup
139
140 void loop() {
141
142   Serial.flush();
143
144   //Wait for module mode
145   while (Serial.available() < 1) {
146   }
147   Module_mode = Serial.read();
148
149   if (Module_mode == 1 ) { //Write register mode
```

```
150     Serial.write(1);
151     Serial.flush();
152     //Wait for module to write to:
153     while (Serial.available() < 1) {
154     }
155     mod_select = Serial.read();
156
157     //Wait for reg prefix information
158     while (Serial.available() < 1) {
159     }
160     reg_prefix = Serial.read();
161
162     //Wait for register address information
163     while (Serial.available() < 1) {
164     }
165     reg_address = Serial.read();
166
167     //Wait for register data information
168     while (Serial.available() < 1) {
169     }
170     reg_data = Serial.read();
171
172     for (input_mod = 0; input_mod < 4; input_mod++) {
173       if (((mod_select >> input_mod) & 0x01) == 1) {
174         //Set multiplexer
175         digitalWriteFast(MUX_A, !!(input_mod & 0x01));
176         digitalWriteFast(MUX_B, !!((input_mod & 0x02) >> 1));
177         delayMicroseconds(50);
178
179         spi4teensy3::write_register(CS_MOD, reg_address, reg_data, reg_prefix);
180         delayMicroseconds(1000); //Wait for register write to finish writing to modules before reading
               back (orig 1000, was set to 50000)
181
182         if ((reg_address == 0x13) && (reg_data == 0x02)) {
183           data_return = spi4teensy3::read_register(CS_MOD, reg_address, reg_prefix, BUSY_BIT);
184           while(((data_return >> 1) & 0xFF) !=0x08) {
185             data_return = spi4teensy3::read_register(CS_MOD, reg_address, reg_prefix, BUSY_BIT);
186           }
187         }
188
189         else {
190           valid_regdata = 1;
191           while (valid_regdata) { //remove for saving configuration
192             data_return = spi4teensy3::read_register(CS_MOD, reg_address, reg_prefix, BUSY_BIT);
193             valid_regdata = ((data_return >> 21) & 0x07); // Set valid_regdata to 1 if busy/error/reg data
                    (0)— event data (1)
194             delayMicroseconds(50);
195           }
196         }
197         Serial.println(reg_address, HEX); //Address info
198         Serial.println((data_return >> 1) & 0xFF, HEX); //Data info
199         Serial.flush(); // set Serial flush after serial.println
```

```
200
201         if ((reg_prefix == 8) && (reg_address == 196)) {
202           int Globalthreshold = ((data_return >> 1) & 0xFF) * 1.1765;
203           Serial.println(Globalthreshold, DEC);
204           Serial.flush(); // set Serial flush after serial.println
205         } //globalthreshold
206       } //end of if mod
207     } //end of for mod
208   } //End of write register mode
209
210   else if (Module_mode == 2) { //Read register mode
211     Serial.write(2);
212     Serial.flush();
213
214     //Wait for module to write to:
215     while (Serial.available() < 1) {
216     }
217     mod_select = Serial.read();
218
219     //Wait for reg prefix information
220     while (Serial.available() < 1) {
221     }
222     reg_prefix = Serial.read();
223
224     //Wait for register address information
225     while (Serial.available() < 1) {
226     }
227     reg_address = Serial.read();
228
229     for (input_mod = 0; input_mod < 4; input_mod++) {
230       if (((mod_select >> input_mod) & 0x01) == 1) {
231         //Set multiplexer
232         digitalWriteFast(MUX_A, !!(input_mod & 0x01));
233         digitalWriteFast(MUX_B, !!((input_mod & 0x02) >> 1));
234         delayMicroseconds(50);
235
236         //Read register content
237         data_return = spi4teensy3::read_register(CS_MOD, reg_address, reg_prefix, BUSY_BIT);
238         valid_regdata = ((data_return >> 23) & 0x01); //busy/error/reg data (0)— event data (1)
239         while (valid_regdata == 1) {
240           data_return = spi4teensy3::read_register(CS_MOD, reg_address, reg_prefix, BUSY_BIT);
241           valid_regdata = ((data_return >> 23) & 0x01); //busy/error/reg data (0)— event data (1)
242           delayMicroseconds(10);
243         }
244         Serial.println(reg_address, HEX);
245         Serial.println((data_return >> 1) & 0xFF, HEX); //Data info
246         Serial.flush();
247         secondary_registers(reg_address, reg_prefix);
248
249       } //if mod
250     } //for mod
251   } //end of read register mode
```

```
252
253   else if (Module_mode == 51) { // Event readout mode
254     mod_select = 15;
255     Serial.write(3);
256     Serial.flush();
257     event_data = (uint32_t *)malloc(BufferSize * sizeof(uint32_t));
258
259     for (input_mod = 0; input_mod < 4; input_mod++) {
260       if (((mod_select >> input_mod) & 0x01) == 1) {
261         digitalWriteFast(MUX_A, !!(input_mod & 0x01));
262         digitalWriteFast(MUX_B, !!((input_mod & 0x02) >> 1));
263         delayMicroseconds(50);
264
265         //Initialize event readout mode
266         spi4teensy3::write_register(CS_MOD, 0xC6, 0x03, 0x08); //Channel power setting
267         delayMicroseconds(10);
268         spi4teensy3::write_register(CS_MOD, 0x07, 0xFF, 0x08); //Clear ERRORS
269         delayMicroseconds(10);
270         spi4teensy3::write_register(CS_MOD, 0x08, 0x00, 0x08); //Module control
271         delayMicroseconds(10);
272         spi4teensy3::write_register(CS_MOD, 0x80, 0x00, 0x08); //Charge collection reset - clears analog
                event accumulation components
273         delayMicroseconds(10);
274         spi4teensy3::write_register(CS_MOD, 0x08, 0x02, 0x08); //Module control, clear FIFO
275         delayMicroseconds(10);
276         spi4teensy3::write_register(CS_MOD, 0x80, 0x0A, 0x08); // 0A/03Charge collection reset 1010
                SW_RSTB b1 set high to operate normally
277         delayMicroseconds(10);
278         spi4teensy3::write_register(CS_MOD, 0x08, 0x01, 0x08); //Set OP MODE bit - event readout mode
279         delayMicroseconds(10);
280       }
281     } // end of for mod-  set op mode
282
283     //Wait for acquisition type - total time/total events
284     while (Serial.available() < 1) {
285     }
286     byte eventcount = Serial.read(); //Total time/event counts
287
288     if (eventcount == 48) { //Acquire over time period
289       Serial.flush();
290       Serial.write(0);
291       Serial.flush();
292       //Wait for acquisition time
293       AcqTime = 0;
294       while (Serial.available() < 4) {
295       }
296       Serial.readBytes(tempbuffer, 4);
297
298       AcqTime = (uint32_t) ((tempbuffer[0] << 24) | (tempbuffer[1] << 16) | (tempbuffer[2] << 8) |
              tempbuffer[3]); //c
299       Serial.write(9);
300       Serial.flush();
```

```
301
302       count = 0;
303       timer_counter = 0;
304       remaining_count = 0;
305       timer_flag = 0;
306       input_mod = 0;
307
308       digitalWriteFast(DATA_ACQ_TIMER, HIGH);
309       digitalWriteFast(DATA_ACQ_TIMER, LOW);
310       //Begin event readout timer
311       event_readout_timer.begin(mytimer, 1000); //Timer set to milliseconds
312
313       uint32_t gpio_track = 0;
314       uint32_t gpio_track2 = 0;
315       byte gpio_trig2;
316       gpio_trig = 0;
317       gpio_track = 0;
318       while (!timer_flag) {
319         gpio_trig = 0;
320         input_mod++;
321         if (input_mod >= 4) {
322           input_mod = 0;
323         }
324         gpio_trig = digitalReadFast(14 + input_mod);
325         gpio_track = 0;
326         gpio_track2 = 0;
327
328         digitalWriteFast(MUX_A, !!(input_mod & 0x01));
329         digitalWriteFast(MUX_B, !!((input_mod & 0x02) >> 1));
330         delayMicroseconds(50);
331
332         while (!gpio_trig && !timer_flag) {
333           input_mod++;
334           gpio_track++;
335           if (input_mod >= 4) {//if input_mod exceeds 3, reset input mod and clear all errors
336             input_mod = 0;
337           }
338           gpio_trig = digitalReadFast(14 + input_mod);
339           digitalWriteFast(MUX_A, !!(input_mod & 0x01));
340           digitalWriteFast(MUX_B, !!((input_mod & 0x02) >> 1));
341           delayMicroseconds(50);
342
343           if (gpio_track == 0xFFFF) {
344             gpio_track = 0;
345             if (!gpio_trig) {
346               digitalWriteFast(MUX_A, !!(input_mod & 0x01));
347               digitalWriteFast(MUX_B, !!((input_mod & 0x02) >> 1));
348               delayMicroseconds(50);
349               data_return = spi4teensy3::read_register(CS_MOD, 0x07, 0x08, BUSY_BIT);
350
351               if (((data_return >> 1) & 0xFF) != 0x20) {
352                 spi4teensy3::write_register(CS_MOD, 0x07, 0xFF, 0x08);
```

```
353             delayMicroseconds(10000);  //check to drop to 1000
354             gpio_trig = digitalReadFast(14 + input_mod);
355             gpio_trig2 = gpio_trig;
356             timer_flag = digitalReadFast(DATA_ACQ_TIMER);
357
358             while (!gpio_trig2 && !timer_flag) {
359               spi4teensy3::write_register(CS_MOD, 0x07, 0xFF, 0x08);
360               delayMicroseconds(1000);
361               gpio_trig2 = digitalReadFast(14 + input_mod);
362               gpio_track2++;
363               if (gpio_track2 == 1000) {
364                 gpio_track2 = 0;
365                 if (!gpio_trig2) {
366                   gpio_trig2 = 1;
367                   gpio_trig = 0;
368                 } //if gpio_trig2
369                 else {
370                   gpio_trig = gpio_trig2;
371                 }
372               } //if gpio track2
373               timer_flag = digitalReadFast(DATA_ACQ_TIMER);
374
375             } //while gpio2 and timer
376           } //if data return
377         } // if gpio_track
378       timer_flag = digitalReadFast(DATA_ACQ_TIMER);
379
380       } //while gpio and timer low
381     } //end else statement if gpio high
382
383     while (gpio_trig && !timer_flag) {
384       data_return = spi4teensy3::read_event(CS_MOD, BUSY_BIT);
385       if (((data_return >> 21) & 0x07) == 1) {  //if b001 — busy bit low, error bit low, event bit
              high
386         event_data[count] = (((input_mod & 0x03) << 19) | (((data_return >> 1) & 0x7FF) << 8) | ((
              data_return >> 13 & 0xFF)));
387         count++;
388         if (count == BufferSize) {
389           Serial.write(66);
390           Serial.flush();
391           while (Serial.available() < 1) {
392           }
393           byte Check = Serial.read(); //Receive A when ready
394           if (Check == 65) {
395             USBsend(event_data, count);
396             Serial.write(5);
397             count = 0;
398           }
399         } //if == buffersize
400         remaining_count = count;
401
402       } //if data busy/error
```

```
403
404           else {
405             data_return = spi4teensy3::read_register(CS_MOD, 0x07, 0x08, BUSY_BIT);
406             if (((data_return >> 1) & 0xFF) == 0x20) {
407             }
408             else {
409               spi4teensy3::write_register(CS_MOD, 0x07, 0xFF, 0x08);
410               delayMicroseconds(50);
411             }
412           }
413           timer_flag = digitalReadFast(DATA_ACQ_TIMER);
414           gpio_trig = digitalReadFast(14 + input_mod);
415
416         }// while gpio high and timer low
417         gpio_trig = digitalReadFast(14 + input_mod);
418         timer_flag = digitalReadFast(DATA_ACQ_TIMER);
419
420       } //End of time event readout
421
422       event_readout_timer.end(); //stop timer
423       Serial.write(67); //timer up
424       Serial.flush();
425       while (Serial.available() < 1) {
426       }
427       byte Check = Serial.read();
428       if (Check == 65) {
429         //Read out remaining events left in buffer
430         if (remaining_count > 0) {
431           USBsend(event_data, count);
432           Serial.write(2); //End of data check bit
433           Serial.flush();
434         }
435         else {
436           Serial.write(0);
437           Serial.write(0);
438           Serial.write(4);
439           Serial.flush();
440         }
441       } //check 65
442     } //End of 'if time acquisition'
443
444 //    // Total counts not implemented in this version
445 //    // Acquire for total counts
446 //    else {
447 //    }
448
449     //RESET/CLEAR EVENT READOUT MODE
450     for (input_mod = 0; input_mod < 4; input_mod++) {
451       if (((mod_select >> input_mod) & 0x01) == 1) {
452         digitalWriteFast(MUX_A, !!(input_mod & 0x01));
453         digitalWriteFast(MUX_B, !!((input_mod & 0x02) >> 1));
454         delayMicroseconds(50);
```

```
455
456         spi4teensy3::write_register(CS_MOD, 0x08, 0x00, 0x08); //Module control: Clear OP MODE bit
457         delayMicroseconds(10);
458         spi4teensy3::write_register(CS_MOD, 0x80, 0x00, 0x08); //Charge collection reset: clears analog
                event accumulation components
459         delayMicroseconds(10);
460         spi4teensy3::write_register(CS_MOD, 0x08, 0x02, 0x08); //Module control: clear FIFO
461         delayMicroseconds(10);
462         spi4teensy3::write_register(CS_MOD, 0x00, 0x01, 0x08); //Module reset — clears FIFO and returns
                modules to default state
463         delayMicroseconds(10);
464       }
465     }
466     free (event_data);
467   } //End of event readout mode
468
469   else if (Module_mode == 4) {
470     pixel_map = (uint8_t *)malloc(256 * sizeof(uint8_t));
471     uint16_t indx_s;
472
473     //Wait for modules to write to:
474     while (Serial.available() < 1) {
475     }
476     mod_select = Serial.read();
477
478     while (Serial.available() < 1) {
479     }
480     byte pix_on = Serial.read();
481
482     while (Serial.available() < 1) {
483     }
484     byte pix_off = Serial.read();
485
486     for (input_mod = 0; input_mod < 4; input_mod++) {
487       if (((mod_select >> input_mod) & 0x01) == 1) {
488         digitalWriteFast(MUX_A, !!(input_mod & 0x01));
489         digitalWriteFast(MUX_B, !!((input_mod & 0x02) >> 1));
490         delayMicroseconds(50);
491
492         //Config pixels on
493         if (pix_on) {
494           Pixel_Config(0x07);
495         }
496         //Config pixels off
497         if (pix_off) {
498           Pixel_Config(0x17);
499         }
500       }
501     }
502
503     for (input_mod = 0; input_mod < 4; input_mod++) {
504       if (((mod_select >> input_mod) & 0x01) == 1) {
```

```
505         digitalWriteFast(MUX_A, !!(input_mod & 0x01));
506         digitalWriteFast(MUX_B, !!((input_mod & 0x02) >> 1));
507         delayMicroseconds(50);
508
509         for (indx_s = 0; indx_s < 256; indx_s++) {
510           data_return = spi4teensy3::read_register(CS_MOD, indx_s, 0x0A, BUSY_BIT);
511           pixel_map[indx_s] = ((data_return >> 5) & 0x01);
512         }
513         Serial.write(pixel_map, 256);
514         Serial.flush();
515       }
516     }
517     free(pixel_map);
518   }
519
520 //This mode not currently implemented.
521   else if (Module_mode == 5) {
522     //Check teensy temperature
523     int tempValue = analogRead(tempPin);
524     Vout = tempValue / 4096.*3.3;
525     Teensy_temp = Vout / 0.01 - 40;
526     Serial.println(Teensy_temp);
527     delay(100);
528
529     mod_select = 15;
530     for (input_mod = 0; input_mod < 4; input_mod++) {
531       if (((mod_select >> input_mod) & 0x01) == 1) {
532         digitalWriteFast(MUX_A, !!(input_mod & 0x01));
533         digitalWriteFast(MUX_B, !!((input_mod & 0x02) >> 1));
534         delayMicroseconds(50);
535         power_status = digitalRead(PWR_OK);
536         Serial.print(power_status);
537       }
538     }
539     Serial.println();
540   }
541
542   else if (Module_mode == 6) {
543     //Reset all modules
544     digitalWriteFast(RSTB, LOW);
545     delayMicroseconds(100000);
546     digitalWriteFast(RSTB, HIGH);
547     delayMicroseconds(1000);
548
549     //Wait for power up
550     for (ii = 0; ii < 2; ii++) {
551       for (jj = 0; jj < 2; jj++) {
552         digitalWriteFast(MUX_A, !!ii);
553         digitalWriteFast(MUX_B, !!jj);
554         delayMicroseconds(50);
555         power_status = 0;
556         while (!power_status) {
```

```
557           power_status = digitalRead(PWR_OK);
558         }
559       }
560     } //end of loop to power on modules
561
562     //Reset all modules
563     for (ii = 0; ii < 2; ii++) {
564       for (jj = 0; jj < 2; jj++) {
565         digitalWriteFast(MUX_A, !!ii);
566         digitalWriteFast(MUX_B, !!jj);
567         delayMicroseconds(50);
568
569         //Write to register
570         spi4teensy3::write_register(CS_MOD, 0x00, 0x01, 0x08); //Module RST
571         delayMicroseconds(10);
572         spi4teensy3::write_register(CS_MOD, 0x08, 0x02, 0x08); //Clear FIFO
573         delayMicroseconds(10);
574       }
575     } //end of loop to reset all modules
576   }
577
578 }//end of main loop
579
580 void secondary_registers(byte reg_address, byte reg_prefix) {
581   //Temperature monitor
582   if ((reg_prefix == 8) && (reg_address == 10)) {
583     delayMicroseconds(20);
584     data_return = spi4teensy3::read_register(CS_MOD, 0x0A, 0x08, BUSY_BIT);
585     delayMicroseconds(20);
586     data_return2 = spi4teensy3::read_register(CS_MOD, 0x0B, 0x08, BUSY_BIT);
587     uint16_t data_temp = (((data_return2 >> 1) & 0xFF) * 256) + ((data_return >> 1) & 0xFF);
588     float temperature = (float) data_temp * 0.04395 - 50;
589     Serial.println(temperature);
590   }
591
592   //Voltage Monitor #1 (3.3V)
593   else if ((reg_prefix == 8) && (reg_address == 12)) {
594     delayMicroseconds(10);
595     data_return2 = spi4teensy3::read_register(CS_MOD, 0x0D, 0x08, BUSY_BIT);
596     uint16_t data_volt = (((data_return2 >> 1) & 0xFF) * 256) + ((data_return >> 1) & 0xFF);
597     float Voltage1 = ((float) data_volt * 0.0013184);
598     Serial.println(Voltage1, DEC);
599   }
600
601   //Voltage Monitor #2 (5V)
602   else if ((reg_prefix == 8) && (reg_address == 14)) {
603     delayMicroseconds(10);
604     data_return2 = spi4teensy3::read_register(CS_MOD, 0x0F, 0x08, BUSY_BIT);
605     uint16_t data_volt2 = (((data_return2 >> 1) & 0xFF) * 256) + ((data_return >> 1) & 0xFF);
606     float Voltage2 = ((float) data_volt2 * 0.001758);
607     Serial.println(Voltage2, DEC);
608   }
```

```
609
610   //Serial Number
611   else if ((reg_prefix == 8) && (reg_address == 2)) {
612     data_return2 = spi4teensy3::read_register(CS_MOD, 0x03, 0x08, BUSY_BIT);
613     delayMicroseconds(1);
614     data_return3 = spi4teensy3::read_register(CS_MOD, 0x04, 0x08, BUSY_BIT);
615     delayMicroseconds(1);
616     data_return4 = spi4teensy3::read_register(CS_MOD, 0x05, 0x08, BUSY_BIT);
617     uint32_t Serialnumber = (((data_return >> 1) & 0xFF) + (((data_return2 >> 1) & 0xFF) * 256) + (((
          data_return3 >> 1) & 0xFF) * 65536) + (((data_return4 >> 1) & 0xFF) * 16777216)) ;
618     Serial.println(Serialnumber, DEC);
619   }
620
621   //Over Temp
622   else if ((reg_prefix == 8) && (reg_address == 16)) {
623     uint16_t over_temp = (((data_return >> 1) & 0xFF) * 16);
624     float over_temperature = (float) over_temp * 0.04395 - 50;
625     Serial.println(over_temperature);
626   }
627
628   //Global Pixel Threshold
629   else if ((reg_prefix == 8) && (reg_address == 196)) {
630     int Globalthreshold = ((data_return >> 1) & 0xFF) * 1.1765;
631     Serial.println(Globalthreshold, DEC);
632   }
633 }
634
635 void mytimer(void) {
636   timer_counter = timer_counter + 1; //Timer counter for every 100ms
637   if (timer_counter >= AcqTime) {
638     timer_counter = 0;
639     digitalWriteFast(DATA_ACQ_TIMER, HIGH); //if timer is up, end event readout mode
640     //RESET/CLEAR EVENT READOUT MODE
641     for (input_mod = 0; input_mod < 4; input_mod++) {
642       if (((mod_select >> input_mod) & 0x01) == 1) {
643         digitalWriteFast(MUX_A, !!(input_mod & 0x01));
644         digitalWriteFast(MUX_B, !!((input_mod & 0x02) >> 1));
645         delayMicroseconds(50);
646         spi4teensy3::write_register(CS_MOD, 0x08, 0x00, 0x08); //Module control: Clear OP MODE bit
647         delayMicroseconds(10);
648         spi4teensy3::write_register(CS_MOD, 0x80, 0x00, 0x08); //Charge collection reset: clears analog
              event accumulation components
649         delayMicroseconds(10);
650         spi4teensy3::write_register(CS_MOD, 0x08, 0x02, 0x08); //Module control: clear FIFO
651         delayMicroseconds(10);
652         spi4teensy3::write_register(CS_MOD, 0x00, 0x01, 0x08); //Module reset - clears FIFO and returns
              modules to default state
653       }
654     }
655   }
656 }
657
```

```
658 //Pixel configuration — Pixel enpixleable and threshold
659 void Pixel_Config(byte pix_on_off) {
660   int numpixel2;
661   int i;
662   byte pix_check;
663   int check_pix;
664   while (Serial.available() < 1) {
665   }
666   int numpixel = Serial.read();
667   numpixel2 = ((int) numpixel) + 1;
668   pixel = (byte*)malloc((numpixel2) * sizeof(byte));
669 
670   for (i = 0; i < numpixel2; i++) {
671     while (Serial.available() < 1) {
672     }
673     pixel[i] = Serial.read();
674   }
675 
676   check_pix = 0;
677   for (int ij = 0; ij < numpixel2; ij++) {
678     check_pix++;
679     spi4teensy3::write_register(CS_MOD, pixel[ij], pix_on_off, 0x0A);
680     delayMicroseconds(100);
681     data_return = spi4teensy3::read_register(CS_MOD, pixel[ij], 0x0A, BUSY_BIT);
682     pix_check = ((data_return >> 5) & 0x01);
683 
684     while (pix_check == !((pix_on_off >> 4) & 0xFF)) {
685       spi4teensy3::write_register(CS_MOD, pixel[ij], pix_on_off, 0x0A);
686       delayMicroseconds(100);
687       data_return = spi4teensy3::read_register(CS_MOD, pixel[ij], 0x0A, BUSY_BIT);
688       pix_check = ((data_return >> 5) & 0x01);
689     }
690   }
691 
692   check_pix = check_pix — 1;
693   Serial.write(check_pix);
694   Serial.flush();
695   free(pixel);
696 }
697 
698 void USBsend(uint32_t *data, uint32_t elements) {
699   uint32_t i;
700   char temp[3 * elements];
701 
702   for (i = 0; i < elements; i++) {
703     temp[3 * i] = (byte) ((data[i] >> 16) & 0xFF);
704     temp[(3 * i) + 1] = (byte) ((data[i] >> 8) & 0xFF);
705     temp[(3 * i) + 2] = (byte) (data[i] & 0xFF);
706   }
707 
708   Serial.write(lowByte(elements)); //Send buffer size (low byte)
709   Serial.write(highByte(elements)); //Send buffer size (high byte)
```

```
  Serial.write(temp, 3 * elements); //Send event data
  Serial.flush();
}
```

Source code C.4: Spi4teensy3 library (Header file)

```
/*
 * File:   spi4teensy3.h
 * Author: xxxajk
 *
 * Created on November 21, 2013, 10:54 AM
 * Last Modified February 12, 2015 by Ashley Tao
 */

#ifndef SPI4TEENSY3_H
#define SPI4TEENSY3_H
#if defined(__MK20DX128__) || defined(__MK20DX256__)
#include <mk20dx128.h> // same header for Teensy 3.0 & 3.1
#include <core_pins.h>
#include <sys/types.h>

#ifndef SPI_SR_RXCTR
#define SPI_SR_RXCTR 0XF0
#endif
#ifndef SPI_PUSHR_CONT
#define SPI_PUSHR_CONT 0X80000000
#endif
#ifndef SPI_PUSHR_CTAS
#define SPI_PUSHR_CTAS(n) (((n) & 7) << 28)
#endif

#define SPI4TEENSY3_MODE_0 0, 0
#define SPI4TEENSY3_MODE_1 0, 1
#define SPI4TEENSY3_MODE_2 1, 0
#define SPI4TEENSY3_MODE_3 1, 1
#define MODE_TO_SPI4TEENSY3_MODE(x) (x & 1), (x&2)

namespace spi4teensy3 {
    void init();
    void init(uint8_t speed);
    void init(uint8_t cpol, uint8_t cpha);
    void init(uint8_t speed, uint8_t cpol, uint8_t cpha);
    void write_register(uint8_t cs_pin, uint8_t reg_address, uint8_t reg_data, uint8_t reg_prefix);
    uint32_t read_event(uint8_t cs_pin, uint8_t bsy_bit);
    uint32_t read_register(uint8_t cs_pin, uint8_t reg_address, uint8_t reg_prefix, uint8_t bsy_bit);
    uint32_t Even_parity_calc(uint32_t frame1);
};
#endif /* __MK20DX128__ || __MK20DX256__ */
#endif  /* SPI4TEENSY3_H */
```

Source code C.5: Spi4teensy3 library (C++ code)

```
/*
 * File:   spi4teensy3.cpp
 * Author: xxxajk
 *
 * Created on November 21, 2013, 10:54 AM
 * Last modified January 29, 2016 by Ashley Tao
 * Functions to send and receive single and array of bytes were removed. Custom 24-bit frames were
     implemented to read and write from Redlen CZT module registers and to read out detected events in
     event data readout mode.
 */

#if defined(__MK20DX128__) || defined(__MK20DX256__)
#include spi4teensy3.h
/**
 * spi4teesny3 is a library for the freescale microcontroller
 * on a teensy 3.x from http://pjrc.com
 * <PRE>
 * Documentation for initialization of SPI.
 *
 * Speed:
 * Speed is the internal buss speed is _always_ divided at least by 2.
 * This table shows the speeds supported for a given value.
 *
 * speed | buss speed  | uC speed | uC speed
 * value |   divisor   | 96/48MHz |  24MHz
 * ------+-------------+----------+---------
 *   0   |      2      |  24MHz   | 12MHz
 * ------+-------------+----------+---------
 *   1   |      4      |  12MHz   | 6MHz
 * ------+-------------+----------+---------
 *   2   |      8      |  6MHz    | 3MHz
 * ------+-------------+----------+---------
 *   3   |      12     |  4MHz    | 2MHz
 * ------+-------------+----------+---------
 *   4   |      16     |  3MHz    | 1.5MHz
 * ------+-------------+----------+---------
 *   5   |      32     |  1.5MHz  | 750KHz
 * ------+-------------+----------+---------
 *   6   |      64     |  750KHz  | 375KHz
 * ------+-------------+----------+---------
 *   7   |      128    |  375KHz  | 187.5KHz
 * ------+-------------+----------+---------
 *
 * cpol is the SPI clock Polarity
 * cpha is the SPI clock capture Phase
 *
 * CPOL | CPHA | Description
 * -----+------+-------------------------------------------------------------------
 *      |      | Idle clock state is low
 *  0   |  0   | data captured on clock low->high
 *      |      | data propagated on high->low
```

```
 * ------+------+-------------------------------------------------------------
 *       |      | Idle clock state is low
 *  0    |  1   | data captured on clock high->low
 *       |      | data propagated on low->high
 * ------+------+-------------------------------------------------------------
 *       |      | Idle clock state is high
 *  1    |  0   | data captured on clock high->low
 *       |      | data propagated on low->high
 * ------+------+-------------------------------------------------------------
 *       |      | Idle clock state is high
 *  1    |  1   | data captured on clock low->high
 *       |      | data propagated on high->low
 * ------+------+-------------------------------------------------------------
 *
 * cpol and cpha are specified separately instead of using mode numbers in order
 * to simplify the design, however, A set of handy macros are available for
 * initialization as follows:
 *
 * SPI4TEENSY3_MODE_0
 * SPI4TEENSY3_MODE_1
 * SPI4TEENSY3_MODE_2
 * SPI4TEENSY3_MODE_3
 * MODE_TO_SPI4TEENSY3_MODE(x) -- where 'x' is 0, 1, 2 or 3
 *
 * The following examples are all equal, but the first one is the best
 * to use for maximum speed and mode 0 as it produces the smallest amount of code.
 * This default was chosen since nearly all devices support mode 0, and all the
 * devices I use work at the maximum speed possible. Your devices might too.
 *
 * spi4teensy3::init()
 * spi4teensy3::init(0)
 * spi4teensy3::init(0, 0)
 * spi4teensy3::init(0, 0, 0)
 * spi4teensy3::init(SPI4TEENSY3_MODE_0)
 * spi4teensy3::init(MODE_TO_SPI4TEENSY3_MODE(0))
 * spi4teensy3::init(0, SPI4TEENSY3_MODE_0)
 * spi4teensy3::init(0, MODE_TO_SPI4TEENSY3_MODE(0))
 *
 * </PRE>
 */
namespace spi4teensy3 {
    uint32_t ctar0;
    uint32_t ctar1;

    void updatectars() {
        // This function is only used internally.
        uint32_t mcr = SPI0_MCR;
        if(mcr & SPI_MCR_MDIS) {
            SPI0_CTAR0 = ctar0;
            SPI0_CTAR1 = ctar1;
        } else {
            SPI0_MCR = mcr | SPI_MCR_MDIS | SPI_MCR_HALT;
```

```
102             SPI0_CTAR0 = ctar0;
103             SPI0_CTAR1 = ctar1;
104             SPI0_MCR = mcr;
105         }
106     }
107 
108     /*
109      * Generic initialization. Maximum speed, cpol and cpha 0.
110      */
111     void init() {
112         SIM_SCGC6 |= SIM_SCGC6_SPI0;
113         CORE_PIN11_CONFIG = PORT_PCR_DSE | PORT_PCR_MUX(2);
114         CORE_PIN12_CONFIG = PORT_PCR_MUX(2);
115         CORE_PIN13_CONFIG = PORT_PCR_DSE | PORT_PCR_MUX(2);
116 
117         ctar0 = SPI_CTAR_DBR | SPI_CTAR_DT(0);
118         ctar1 = ctar0;
119         ctar0 |= SPI_CTAR_FMSZ(7) | SPI_CTAR_PCSSCK(0) | SPI_CTAR_PASC(0) | SPI_CTAR_PDT(0) | SPI_CTAR_DT
                (0);
120         ctar1 |= SPI_CTAR_FMSZ(15) | SPI_CTAR_PCSSCK(0) | SPI_CTAR_PASC(0) | SPI_CTAR_PDT(0) | SPI_CTAR_DT
                (0);
121             SPI0_MCR = SPI_MCR_MSTR | SPI_MCR_PCSIS(0x1F) | SPI_MCR_CLR_RXF | SPI_MCR_CLR_TXF;
122         updatectars();
123     }
124 
125         /**
126          * Initialization with max speed, cpol and cpha configurable.
127          * @param cpol SPI Polarity
128          * @param cpha SPI Phase
129          */
130         void init(uint8_t cpol, uint8_t cpha) {
131             init();
132             ctar0 |= (cpol == 0 ? 0 : SPI_CTAR_CPOL) | (cpha == 0 ? 0 : SPI_CTAR_CPHA);
133             ctar1 |= (cpol == 0 ? 0 : SPI_CTAR_CPOL) | (cpha == 0 ? 0 : SPI_CTAR_CPHA);
134             updatectars();
135         }
136 
137         /**
138          * Initialization with cpol and cpha 0, speed is configurable.
139          *
140          * @param SPI speed [0—7]
141          */
142         void init(uint8_t speed) {
143             init();
144             // Default 1/2 speed
145             uint32_t ctar = SPI_CTAR_DBR;
146             switch(speed) {
147                 case 1: // 1/4
148                     ctar = 0;
149                     break;
150                 case 2: // 1/8
151                     ctar = SPI_CTAR_BR(1);
```

```
152                 break;
153             case 3: // 1/12
154                 ctar = SPI_CTAR_BR(2);
155                 break;
156             case 4: // 1/16
157                 ctar = SPI_CTAR_BR(3);
158                 break;
159             case 5: // 1/32
160                 ctar = SPI_CTAR_PBR(1) | SPI_CTAR_BR(4);
161                 break;
162             case 6: // 1/64
163                 ctar = SPI_CTAR_PBR(1) | SPI_CTAR_BR(5);
164                 break;
165             case 7: //1/128
166                 ctar = SPI_CTAR_PBR(1) | SPI_CTAR_BR(6);
167                 // fall thru
168            default:
169                 // default 1/2 speed, this is the maximum.
170                 break;
171             }
172             ctar0 = ctar | SPI_CTAR_FMSZ(7) | SPI_CTAR_PCSSCK(0) | SPI_CTAR_PASC(0) | SPI_CTAR_PDT(0);
173             ctar1 = ctar | SPI_CTAR_FMSZ(15) | SPI_CTAR_PCSSCK(0) | SPI_CTAR_PASC(0) | SPI_CTAR_PDT(0)
                      ;
174             updatectars();
175         }
176
177         /**
178          * Initialization with speed, cpol, and cpha configurable.
179          *
180          * @param SPI speed [0—7]
181          * @param cpol SPI Polarity
182          * @param cpha SPI Phase
183          */
184         void init(uint8_t speed, uint8_t cpol, uint8_t cpha) {
185             init(speed);
186             ctar0 |= (cpol == 0 ? 0 : SPI_CTAR_CPOL) | (cpha == 0 ? 0 : SPI_CTAR_CPHA);
187             ctar1 |= (cpol == 0 ? 0 : SPI_CTAR_CPOL) | (cpha == 0 ? 0 : SPI_CTAR_CPHA);
188             updatectars();
189         }
190
191         /**
192          * Write data to register
193          *
194          * @param cs_pin Chip select pin
195          * @param reg_address Address register
196          * @param reg_data Data to be written to reg_address
197          * @param reg_prefix Register prefix
198          */
199         void write_register(uint8_t cs_pin, uint8_t reg_address, uint8_t reg_data, uint8_t reg_prefix) {
200             uint32_t tx_buffer;
201             tx_buffer = ((0x00 | reg_prefix) << 16) | (reg_address << 9) | (reg_data << 1);
202                     tx_buffer = Even_parity_calc(tx_buffer);
```

```
203
204             // clear any data in RX/TX FIFOs, and be certain we are in master mode.
205             SPI0_MCR = SPI_MCR_MSTR | SPI_MCR_CLR_RXF | SPI_MCR_CLR_TXF | SPI_MCR_PCSIS(0x1F);
206             SPI0_SR = SPI_SR_TCF;
207             digitalWriteFast(cs_pin,0);
208             SPI0_PUSHR = SPI_PUSHR_CONT | SPI_PUSHR_CTAS(0) | ((tx_buffer >>16) & 0xFF) ;
209             SPI0_PUSHR = SPI_PUSHR_EOQ | SPI_PUSHR_CTAS(1) | (uint16_t) tx_buffer;
210
211             while((SPI0_SR & SPI_SR_EOQF) == 0);
212                 SPI0_SR = SPI_SR_EOQF;
213                 digitalWriteFast(cs_pin,1);
214         }
215
216         /**
217          * Read data from register
218          *
219          * @param cs_pin Chip select pin
220          * @param reg_address Address register
221          * @param reg_prefix Register prefix
222          * @param bsy_bit Bit 1 of MISO frame
223          * Return data from register
224          */
225         uint32_t read_register(uint8_t cs_pin, uint8_t reg_address, uint8_t reg_prefix, uint8_t bsy_bit) {
226             uint32_t tx_buffer;
227             tx_buffer = ((0x40 | reg_prefix) << 16) | (reg_address << 9) ;
228             tx_buffer = Even_parity_calc(tx_buffer);
229             uint32_t data_return = 0;
230
231             // clear any data in RX/TX FIFOs, and be certain we are in master mode.
232             SPI0_MCR = SPI_MCR_MSTR | SPI_MCR_CLR_RXF | SPI_MCR_CLR_TXF | SPI_MCR_PCSIS(0x1F);
233             SPI0_SR = SPI_SR_TCF;
234             digitalWriteFast(cs_pin,0);
235             SPI0_PUSHR = SPI_PUSHR_CONT | SPI_PUSHR_CTAS(0) | ((tx_buffer >>16) & 0xFF) ;
236             SPI0_PUSHR = SPI_PUSHR_EOQ | SPI_PUSHR_CTAS(1) | (uint16_t) tx_buffer;
237
238             while((SPI0_SR & SPI_SR_EOQF) == 0);
239             SPI0_SR = SPI_SR_EOQF;
240             digitalWriteFast(cs_pin,1);
241             uint32_t tx_buffer2;
242             tx_buffer2 = 0x800001;
243
244             SPI0_MCR = SPI_MCR_MSTR | SPI_MCR_CLR_RXF | SPI_MCR_CLR_TXF | SPI_MCR_PCSIS(0x1F);
245             SPI0_SR = SPI_SR_TCF;
246
247             //CHECK BUSY BIT
248             digitalWriteFast(cs_pin,0);
249             asm(nop);
250             asm(nop);
251             uint8_t busystatus = digitalReadFast(bsy_bit);
252
253             while (busystatus) {
254                 digitalWriteFast(cs_pin,1);
```

```
255                 asm(nop);
256                 asm(nop);
257                 digitalWriteFast(cs_pin,0);
258                 asm(nop);
259                 asm(nop);
260                 busystatus = digitalReadFast(bsy_bit);
261             }
262             SPI0_PUSHR = SPI_PUSHR_CONT | SPI_PUSHR_CTAS(0) | ((tx_buffer2>>16) & 0xFF);
263                     SPI0_PUSHR = SPI_PUSHR_EOQ | SPI_PUSHR_CTAS(1) | (uint16_t) tx_buffer2;
264
265             while((SPI0_SR & SPI_SR_EOQF) == 0);
266             uint8_t w1 = (SPI0_POPR & 0xFF);
267             uint16_t w2 = SPI0_POPR;
268             SPI0_SR = SPI_SR_EOQF;
269
270             digitalWriteFast(cs_pin,1);
271             data_return = (w1 << 16) | w2;
272             return ~data_return;
273         }
274
275         /**
276          * Return event data in EDR mode
277          */
278         uint32_t read_event(uint8_t cs_pin, uint8_t bsy_bit) {
279                     uint32_t tx_buffer;
280                     tx_buffer = 0x800001;
281                     uint32_t data_return = 0;
282                 uint8_t count = 0;
283                     uint8_t flag = 0;
284             // clear any data in RX/TX FIFOs, and be certain we are in master mode.
285             SPI0_MCR = SPI_MCR_MSTR | SPI_MCR_CLR_RXF | SPI_MCR_CLR_TXF | SPI_MCR_PCSIS(0x1F);
286             SPI0_SR = SPI_SR_TCF;
287
288             //CHECK BUSY BIT
289             digitalWriteFast(cs_pin,0);
290             asm(nop);
291             asm(nop);
292                     asm(nop);
293                     uint8_t busystatus = digitalReadFast(bsy_bit);
294             count = 0;
295                     while (busystatus) {
296                 digitalWriteFast(cs_pin,1);
297                 asm(nop);
298                 asm(nop);
299                         asm(nop);
300                         digitalWriteFast(cs_pin,0);
301                         asm(nop);
302                         asm(nop);
303                         asm(nop);
304                         busystatus = digitalReadFast(bsy_bit);
305                 count++;
306                 if (count >=5) {
```

```
307                             flag = 1;
308                             data_return = 0xFFFFFFFF;
309                             break;
310                 }
311                     }
312 
313             SPI0_PUSHR = SPI_PUSHR_CONT | SPI_PUSHR_CTAS(0) | ((tx_buffer >>16) & 0xFF);
314                     SPI0_PUSHR = SPI_PUSHR_EOQ | SPI_PUSHR_CTAS(1) | (uint16_t) tx_buffer;
315 
316             while((SPI0_SR & SPI_SR_EOQF) == 0);
317                     uint8_t w1 = (SPI0_POPR & 0xFF);
318                     uint16_t w2 = SPI0_POPR;
319                     SPI0_SR = SPI_SR_EOQF;
320                     data_return = (w1 << 16) | w2;
321                     digitalWriteFast(cs_pin,1);
322                     return ~data_return;
323         }
324 
325         /**
326          * Calculate even parity (if odd, parity bit = 1; if even, parity bit =0)
327          */
328         uint32_t Even_parity_calc(uint32_t frame1){
329                     uint32_t frame = frame1;
330                     uint32_t noofones = 0;
331                     while(frame !=0){
332                         noofones++;
333                         frame &= (frame-1); //the loop will execute once for each bit of ino set
334                     }
335 
336                     //if noofones is odd, least significant bit will be 1 */
337                     uint32_t parity = noofones & 1;
338                     frame1 = frame1 + parity;
339                     return frame1;
340         }
341 }
342 #endif
```